ABSTRACT

Title of Document: **SEMICONDUCTOR AND GLASS MICRO-RESONATORS**

Li-Chiang Kuo

Doctor of Philosophy, 2015

Directed By: **Professor Christopher Davis**

Electrical and Computer Engineering

In this thesis we have demonstrated the cascading of two photonic AND logic gates by using two symmetric semiconductor GaAs microring resonators. In addition, we have developed a new, low-cost method for fabricating glass microring resonators.

In the first part of this work, we discuss the properties of microring resonators and describe the fabrication of semiconductor microring resonators by the research team of which I was a member. In the experiments on cascaded logic gates we launched one probe and pump beam into different input waveguides, respectively. The first ring works as a AND logic gate for probe and pump beams. The output beam from the first ring goes to the second ring. The second ring also work as a AND logic gate using the second pump to switch the beam coming from the first ring. We successfully demonstrated

cascading two photonic logic gates by using two symmetric semiconductor GaAs microrings.

In the second part of this work, we extended our prior work on the fabrication of semiconductor microrings in a clean room to a purely mechanical method of glass microring fabrication. Many laboratories, including ours, lack the expensive facilities needed for the lithographic fabrication of microrings. And, a low-cost, high yield method of fabrication may have significant application in the development of disposable microring sensors. We have built up a complete mass=production capability based on glass capillary pulling and micro-polishing to fabricate glass microrings, because there were no available off-the-shelf systems available from industry at affordable prices.

This method of producing highly polished glass micro-resonators has many advantages, such as fast fabrication ($\leqq$6 weeks), high yield ($\geqq$50%) (percentage of devices w/o cracks on edge), low cost (no need to use costly facilities in a clean room), mass production (800~1200 devices per batch). The surface quality of glass resonators should be excellent because capillaries were made at high temperature $\geqq$1000℃ and devices were polished by suspension slurry of 70 nm colloidal silica. Further measurements that are beyond our current capability are needed for final verification. If some fabrication steps could be optimized in the future, we estimate that the fabrication time could be within 2 weeks, the yield rate would be higher than 90 %, and the number of devices per batch could be more than 1,200.

This innovative method opens a new path for microresonator fabrication at low cost and in fast mass production. In sensor applications where low cost and mass production could be important, our work is an important first step to making microring

sensors inexpensive, if further work in characterizing them can be done. Glass microresonators can play a key role, for example, in gas sensors, chemical sensors, liquid sensors, biological sensors, and vibration sensors. Two appendices in this thesis list the most significant sub-systems of the whole system we designed and built for producing glass microring resonators. Designs and engineering drawings are also listed in Appendices.

SEMICONDUCTOR AND GLASS MICRO-RESONATORS

By

Li-Chiang Kuo

Dissertation submitted to the Faculty of the Graduate School of the
University of Maryland, College Park, in partial fulfillment
of the requirements for the degree of
Doctor of Philosophy
2015

Advisory Committee:
Professor Christopher Davis, Chair
Professor Julius Goldhar
Professor Thomas Murphy
Professor Jeremy Munday
Professor Miao Yu

Acknowledgements

For the completion of this dissertation, I would like to thank Professor P.T. Ho, Tarek Ibrahim, Rohit Grover, Kuldeep Amarnath, Wei-Yen Chen, and all other members of our research group at the Laboratory for Physical Sciences who have helped me in many ways in my experiments. I am grateful to Professor Julius Goldhar whose helpful advice has improved my dissertation. I would also like to thank my adviser, Professor Christopher Davis for giving me useful advice on my experiments and thesis discussion. Besides, he also has given much encouragement. This has been valuable for my thesis progress. In addition, I would like to acknowledge the support of project funding from Prof Chi at National Chao Tung University in Taiwan. All of this help from my colleagues has contributed to the completion of this thesis. I truly appreciate their help.

Table of Contents

Chapter 1: Introduction

1.1 Development and need by industry

Over the past decades, the integrated circuit industry has developed rapidly and has changed many aspects of our daily life. CPU clock rate has evolved from the early 33MHz, to the current 4 GHz. There are potentially many advantages in using optical devices to fulfill photonic integrated circuits [1]. Nowadays, optical transmission dominates high-speed communications. More and more optical components are replacing electronics in optical processing applications. The current trend is to add more photonic devices on a single chip. The factors truly affecting the dimensions of photonic devices are the choices of dielectric materials and geometrical structures suitable for low-loss propagation. Different groups have developed many different devices. But, none of them has achieved systematic large-scale photonic integration. Over the past ten years, micro-ring resonators have been attracting more and more attention. The key advantage of micro-ring resonators is that the micro-ring resonator is a versatile elemental building block which is appropriate for massive integration. Since 1990s different aspects of functionality of micro-ring resonator have been demonstrated, such as optical sensing [50], all-optical switching [51], microring modulator [52], optical digital-to-analog converter [53], fast wavelength locking [54], modulator for metro networks [55], photonic differentiator [56], pulley-type resonator [57], trace gas absorption spectroscopy [58], channel dropping filter [2], second order filter [3,4], eight-channel add-drop filter [5], all-optical switching [6], AND/NAND Logic [7], photonic logic NOR gate [8],

spatial pulse routing [9], low-power optical memory [10,11], microring lasers [12,13,14], optical sensing of bio-molecules using microring [15,16], and so on.

Optical devices like micro-ring resonators have many advantages such as low cross talk, low propagation loss, small dimension, coherent properties, and so forth. Microring resonators have great potential to become the universal building block for future photonic integrated circuits [1].

1.2 Basic concepts of micro-ring resonators

The discussion in the following sections of this chapter is based on the literature [17 - 23].

1.2.1 Resonant wavelengths

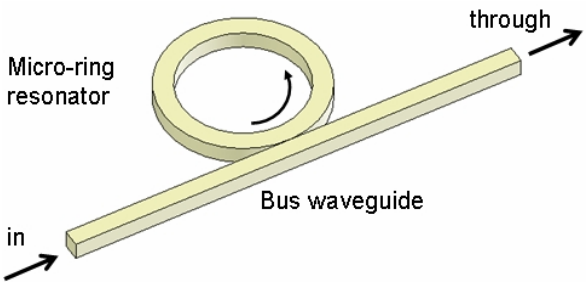

Fig 1: Schematic of a microring resonator. The input light wave couples in and out of the microring through the bus waveguide

A microring is an optical waveguide whose shape is a ring structure as can be seen in Fig 1. The circumference of the microring is from a few microns to a few hundred microns. A light wave coupled into a ring will circulate inside the ring. Subsequently the light wave will be coupled out of this structure. For resonant wavelength, the field repeats itself after one round trip. Its amplitude and phase satisfy the following condition

$$m\ \lambda_m\ =\ 2\pi R\ n_{eff} \tag{1}$$

Here, *m* is the order of resonance, λ_m is the wavelength of the *m*-th longitudinal mode, R is the radius of the ring resonator, n_{eff} is the effective index of the optical mode in the ring waveguide. At resonance the intensity inside the ring resonator will be many times larger than the value in the bus waveguide.

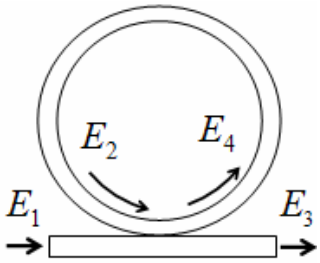

Fig 2: Schematic of a single waveguide coupling to a single microring

$$E_2(t) = a\ E_4(t - n_{eff}L/c) = a\ e^{j\phi}E_4(t) \tag{2}$$

L is circumference, t is time, ϕ is the round-trip phase in the ring resonator, a is amplitude of light wave. The single-pass phase ϕ is given by

$$\phi = 2\pi \frac{Ln_{eff}}{\lambda} \tag{3}$$

In the ring resonator, the circulating field E_4 is given by

$$E_4(t) = -j\kappa E_1(t) + \tau E_2(t) = -j\kappa E_1(t) + \tau\ a\ e^{j\phi}E_4(t) \tag{4}$$

τ and κ are transmission and coupling coefficient between bus waveguide and ring resonator, respectively. Due to power conservation, it is required that

$$\kappa^2 + \tau^2 = 1 \tag{5}$$

The transmitted field E_3 is given by

$$E_3(t) = \tau E_1(t) - j\kappa E_2(t) = \tau E_1(t) - j\kappa \; a \; e^{j\phi} E_4(t) \tag{6}$$

In a steady state, the transfer function of the ring resonator is given by solving Eq (4) and Eq (6)

$$T \equiv \frac{E_3}{E_1} = \frac{\tau - a \; e^{j\phi}}{1 - \tau a \; e^{j\phi}} \tag{7}$$

The effective phase shift for the ring resonator is defined as the phase argument of the transfer function of the ring resonator [17]. For negligible attenuation (a=1) the effective phase shift ϕ is given by [17]

$$\phi_{\underset{(a=1)}{eff}} = \pi - \phi - 2\tan^{-1}\left(\frac{\tau \sin\phi}{1 - \tau\cos\phi}\right) \tag{8}$$

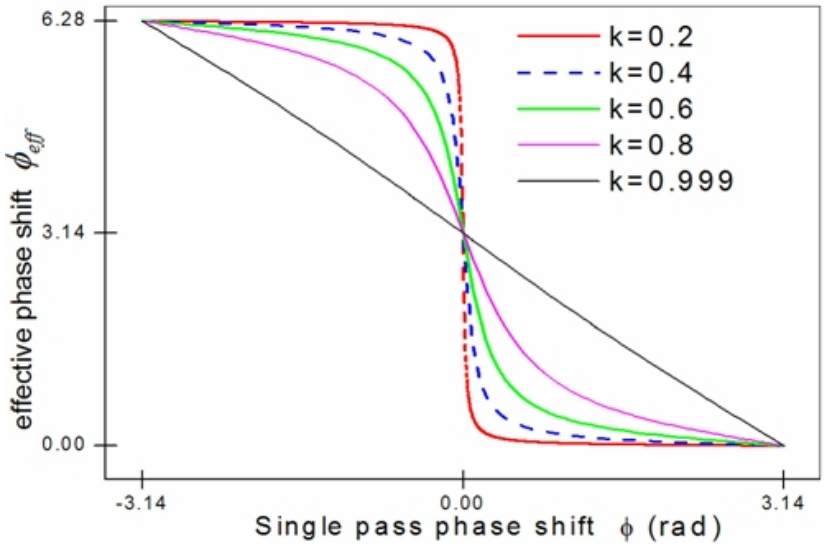

Fig 3: Diagram of phase shift for a lossless ring resonator (Here, we assume *a*=1). Here, k in the figure is coupling coefficient between microring and bus waveguide

In the above figure, Fig 3, the slope of the phase shift is extremely steep near resonance (ϕ=0) for a lossless ring resonator (a=1). So, the phase of the device output is very sensitive to the variation of the single-pass phase shift in the ring resonator. This phase enhancement has already been observed in experiment by inserting a ring resonator in one arm of a Mach-Zehnder interferometer [18].

1.2.2 Field enhancement

The physical meaning of the field enhancement factor (FE) is the magnitude ratio of the circulating field in the ring to the input field at resonance. Let us consider a steady state. The circulating field inside the ring resonator is given by

$$E_4 = -j\kappa E_1 + \tau\ a\ e^{j\phi} E_4 \tag{9}$$

Then, the magnitude ratio of the circulating field in the ring to the input field at resonance is given by

$$FE \equiv \left| \frac{E_{circulating}}{E_{input}} \right|_{\phi=0} = \left| \frac{E_4}{E_1} \right|_{\phi=0} = \frac{\kappa}{1-a\tau} \tag{10}$$

κ is coupling coefficient between ring and bus waveguide. As can be seen in Eq.(10), the built-up intensity in the ring resonator is larger when field enhancement (FE) is bigger. In the meantime, the intensity of the input beam required to produce significant nonlinear effects in the ring resonator is lower for larger FE.

1.2.3 Free spectral range (FSR)

The free spectral range is defined as the wavelength separation between two consecutive resonances. For two consecutive resonances, the longitudinal mode number changes by unity

$$m\ \lambda_m\ =\ L\ n_{eff}\ =(m-1)\ \lambda_{m-1}\ =(m-1)\ (\lambda_m+\Delta\lambda) \tag{11}$$

Assume that $m >> 1$ ($\Delta\lambda >> \lambda$). The above equation gives the expression for FSR.

$$\Delta\lambda \approx \frac{\lambda^2}{L\ n_{group}} \tag{12}$$

For a smaller round trip, FSR will be larger. n_{group} is group index.

1.2.4 Microring bandwidth

The definition of ring resonator bandwidth is the full width at half maximum (FWHM) of the intensity in the ring resonator. It is the 3-dB bandwidth.

$$\left|\frac{E_4}{E_1}\right|^2 = \left|\frac{-j\kappa}{1-a\tau e^{j\Delta\phi}}\right|^2 = \frac{1}{2}\times\left|\frac{\kappa}{1-a\tau}\right|^2 \tag{13}$$

By solving the above equation this gives

$$\cos(\Delta\phi) = \frac{4a\tau - 1 - a^2\tau^2}{2a\tau} \tag{14}$$

In terms of Taylor expansion for narrow bandwidth, this becomes

$$\cos(\Delta\phi) \approx\ 1-\frac{(\Delta\phi)^2}{2} \tag{15}$$

From Eq (14) and Eq (15),

$$1-\frac{(\Delta\phi)^2}{2}\approx\frac{4a\tau-1-a^2\tau^2}{2a\tau} \tag{16}$$

and

$$\Delta\phi=\frac{1-a\tau}{\sqrt{a\tau}} \tag{17}$$

Then,

$$|\Delta\phi|=\left|\Delta\left(2\pi\frac{Ln_{eff}}{\lambda}\right)\right|=\left|2\pi\frac{Ln_{eff}(-1)\Delta\lambda}{\lambda^2}\right|=2\pi\frac{Ln_{eff}|\Delta\lambda|}{\lambda^2} \tag{18}$$

From Eq (17) and Eq (18)

$$\Delta\lambda_{FWHM}=2|\Delta\lambda|\ \approx\ \frac{\lambda^2}{\pi Ln_{eff}}\times\frac{1-a\tau}{\sqrt{a\tau}} \tag{19}$$

1.2.5 Finesse

$$Finesse=\frac{FSR}{\Delta\lambda_{FWHM}}=\frac{\pi\sqrt{a\tau}}{1-a\tau} \tag{20}$$

$\Delta\lambda_{FWHM}$ is the resonance bandwidth (full width at half maximum). a is round-trip loss factor in the ring resonator. τ is field transmission coefficient.

1.2.6 Cavity Q factor

The Q factor of a ring resonator shows its ability to store energy. It is defined as the ratio of the energy stored in the ring to the energy dissipated per oscillation. The energy dissipation means absorption in the ring resonator or coupling out to the bus waveguide.

$$Q = \frac{energy\ stored\ in\ the\ ring}{power\ loss} \times \omega \tag{21}$$

ω is the frequency of light coupled to the ring resonator. The quality factor of a ring resonator can be calculated from [23]

$$Q = \frac{\lambda_m}{\Delta\lambda_{FWHM}} = \frac{\pi n_{eff} L}{\lambda_m} \times \frac{\sqrt{a\tau}}{1 - a\tau} = \frac{n_{eff} L}{\lambda_m} \times Finesse \tag{22}$$

τ is field transmission coefficient. λ_m is the wavelength of the m-th longitudinal mode.

1.2.7 Cavity photon lifetime

Cavity photon lifetime is defined as the average time a photon stays in the ring resonator before it is absorbed or transmitted. It is inversely proportional to the resonator bandwidth. It is given by [23]

$$\tau_{ph} = \frac{1}{\Delta f_{FWHM}} = \frac{\pi n_{eff} L}{c} \times \frac{\sqrt{a\tau}}{1 - a\tau} = \frac{n_{eff} L}{c} \times Finesse \tag{23}$$

c is the speed of light in free space.

1.3 The scope of this dissertation

This thesis has two parts. In the first part, chapters 2-4, the cascading of two AND photonic logic gates using two symmetric semiconductor microrings will be discussed. In the second part, based on our prior work on semiconductor microring fabrication we developed a new method for fabricating highly polished glass microresonator. This method has improved the yield rate (percentage of devices w/o cracks on edge), shortened the total time of fabrication, and improved the surface quality of devices. We designed, made, and built the whole system specific for glass microresonators. This part will be discussed in Chapter 5, Appendix 1, and Appendix 2. Chapter 6 will summarize the achievements and innovations of this thesis.

Chapter 2: Semiconductor microring resonators

In this chapter we will discuss several mechanisms in semiconductor microring resonators for enhancing their nonlinear response in switching. These will be helpful for discussing the experiment on cascade photonic logic gates that will be discussed in chapter three. These theories had been developed mainly by Dr. Vien Van in our group [21, 41] and Dr. J. E. Heebner [17].

2.1 Optical nonlinearity

The discussion in this section is based on the books [35-41]. First, the instantaneous response of optical nonlinearity of a material can be written as follows

$$P(t) = P^{(1)}(t) + P^{(2)}(t) + P^{(3)}(t) + \cdots = \varepsilon_0[\chi^{(1)}E(t) + \chi^{(2)}E^2(t) + \chi^{(3)}E^3(t) + \ldots] \quad (24)$$

P is polarization of material, E is electric field strength, ε_0 is the free space permittivity, $\chi^{(n)}$ is the n-th order nonlinear optical susceptibilities. The constant of proportionality $\chi^{(1)}$ is known as the linear susceptibility.

$$n_0 = \mathrm{Re}\left\{\sqrt{1+\chi^{(1)}}\right\}, \qquad \alpha_0 = \frac{4\pi}{\lambda}\mathrm{Im}\left\{\sqrt{1+\chi^{(1)}}\right\} \quad (25)$$

n_0 is linear index of refraction, α_0 is linear absorption. The second order nonlinear susceptibility is responsible for several different processes. These different processes are second harmonic generation (SHG), sum frequency generation (SFG), difference frequency generation (DFG), optical rectification (OR), optical parametric generation (OPG), optical parametric oscillation (OPO), optical parametric amplification (OPA) and

the electro-optic effect. The second order nonlinear optical interaction occurs only in crystals that lack inversion symmetry. .

$$P^{(3)}(t) = \varepsilon_0 \chi^{(3)} E^3(t) \tag{26}$$

The third-order contribution to the nonlinear part of the polarization is described in Eq (26). The third-order susceptibility $\chi^{(3)}$ is responsible for phenomena such as third - harmonic generation, four-wave mixing (FWM), self-focusing, saturable absorption, nonlinear refractive index change, and two-photon absorption. In general, the imaginary part of the $\chi^{(3)}$ is responsible for saturation absorption. Its real part usually refers to nonlinear refractive index change or Kerr nonlinearities.

Now consider a monochromatic applied field

$$E(t) = E\cos(\omega t) \tag{27}$$

Substituting this into Eq (26), this gives

$$P^{(3)}(t) = \frac{1}{4}\varepsilon_0 \chi^{(3)} E^3(t) \times \cos(3\omega t) + \frac{3}{4}\varepsilon_0 \chi^{(3)} E^3(t) \times \cos(\omega t) \tag{28}$$

The third harmonic generation due to the applied field at frequency ω determines the first term. The nonlinear contribution to the nonlinear part of polarization at the frequency of the incident field determines the second term. This second term results in a nonlinear contribution to the index of refraction experienced by an incident light wave centered at frequency ω. Then we represent the index of refraction as

$$n = n_0 + n_2 I \qquad where \quad n_2 = \frac{3}{n_0^2 \varepsilon_0 c}\mathrm{Re}\left\{\chi^{(3)}\right\} \tag{29}$$

n_0 is the linear index of refraction independent of the beam intensity. The second term corresponds to an additional nonlinear refractive index contribution proportional to the beam intensity. In addition, the imaginary part of $\chi^{(3)}$ gives a nonlinear absorption coefficient.

$$\alpha = \alpha_0 + \alpha_2 I \qquad where \quad \alpha_2 = \frac{12\pi}{n_0^2 \varepsilon_0 c \lambda} \mathrm{Im}\left\{\chi^{(3)}\right\} \tag{30}$$

α_0 is the linear absorption coefficient and α_2 is the two-photon absorption coefficient.

2.2 Two-photon absorption (TPA) in semiconductors

Multi-photon phenomena were originally predicted by Maria Goeppert-Mayer in 1931 in her doctoral dissertation [32]. Thirty years later, the invention of the laser allowed the first experimental verification of two-photon absorption (TPA) when two-photon-excited fluorescence was detected in a europium-doped crystal [33] and subsequently observed in a cesium vapor [34]. Goeppert-Mayer received the Nobel prize in Physics for proposing the shell model of the atomic nucleus.

According to solid state physics, one electron in the valence band absorbs one photon of energy equal to or larger than the band gap and it will jump into the conduction band. For two-photon absorption mechanism one electron absorbs two photons whose total energy is equal to or larger than band gap and the electron makes a transition from valence band to conduction band as can be seen in Fig 4. During the processes of two-photon absorption, one free electron and one free hole are generated. This results in free

carriers, which change the electronic and optical properties of the materials. Thus, this causes nonlinear refraction and nonlinear absorption.

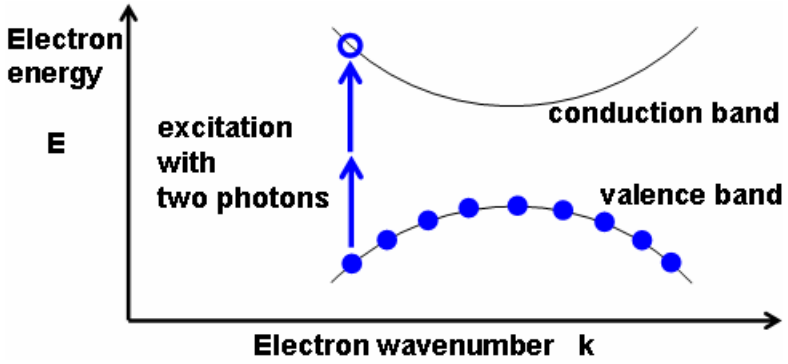

Fig 4: Schematic of two photon absorption process occurring in semiconductor. An electron absorbs two photons and jumps to conduction band from valence band.

When an incident beam travels through an optical waveguide, its intensity variation is given by [40]

$$\frac{dI}{dz} = -\alpha_0 I - \alpha_2 I^2 - (\sigma N_{fc}) I \tag{31}$$

I is the beam intensity across the optical waveguide, σis free carrier absorption cross section (m^2), and α_0 is the linear absorption coefficient, which includes intrinsic loss and scattering loss, α_2 is the nonlinear TPA loss. During TPA processes, the free carrier density changes with time [21, 47-48]

$$\frac{dN_{fc}}{dt} = \frac{\alpha_2}{2\hbar\omega} I^2 - \frac{N_{fc}}{\tau_{fc}} \tag{32}$$

In Eq (32), τ_{fc} is the free carrier recombination time or relaxation time, N_{fc} is the free carrier density, I is the beam intensity across the optical waveguide. This nonlinear

TPA coefficient in GaAs, α_2, is about 18 cm/GW which was measured by Dr. T. A. Ibrahim in our group [7]. It is found that the carrier lifetime was comparable to the microring lifetime [41].

2.3 Enhanced nonlinear response in semiconductor microring

When a microring resonator works as a logic gate, two beams, pump and signal, will be used to do optical switching. The theoretical work about the interaction between the pump-and-probe beams in a ring resonator was developed by Dr. Vien Van in our group. The following discussion is based on his papers [21, 41].

2.3.1 Reduction of the self-switching power

In the context of Fabry–Pérot resonators and fiber rings, many topics have been studied such as steady-state and dynamic transmission properties of resonators with intensity-dependent nonlinearity [42-46]. In the following, we will focus on the reduction achievable in the switching power of a microring due to the resonance condition.

Here we consider the all-pass filter case which we discussed in chapter one.

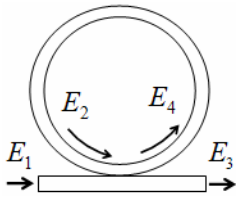

Fig 5: Schematic of a single waveguide coupling to a single microring

As discussed in section 1-2-1, in a steady state the transfer function T of the ring resonator is given by

$$T \equiv \frac{E_3}{E_1} = \frac{\tau - a\ e^{j\phi}}{1 - \tau a\ e^{j\phi}}, \quad \Rightarrow \quad T^2 \equiv \left|\frac{E_3}{E_1}\right|^2 = \frac{2\tau^2(1-\cos\phi)}{1+\tau^4-2\tau^2\cos\phi} \tag{33}$$

ϕ is the round-trip phase shift, τ is transmission coefficient, a is the amplitude of light wave in the ring. The enhancement of the optical intensity in the ring resonator causes a reduction in the effective switching threshold of the device. First we take the derivative of the transfer function of the ring resonator to obtain

$$\frac{dT^2}{dP_{in}} = \frac{dT^2}{d\phi} \times \frac{d\phi}{dP_r} \times \frac{dP_r}{dP_{in}} \tag{34}$$

P_r is the power circulating in the ring resonator, P_{in} is the power of the incident beam. The term on the right-hand side of Eq (34) is the change in the device output due to resonance. It can be calculated from Eq (33) and it gives

$$\frac{dT^2}{d\phi} = \frac{2\tau^2\kappa^4 \sin\phi}{\left(1+\tau^4-2\tau^2\cos\phi\right)^2} \tag{35}$$

κ is coupling coefficient between bus waveguide and ring resonator. In order to maximize the switching efficiency, we choose to operate the ring resonator where the slope of the transmission curve is maximum. It can be seen that this point occurs at just off the resonance peak, as shown in Fig 6 on the next page. For Eq (35) to have maximum, it gives [41]

$$\cos\phi_{\max} \approx 1 - \kappa^4/6 \qquad for\ \kappa << 1 \tag{36}$$

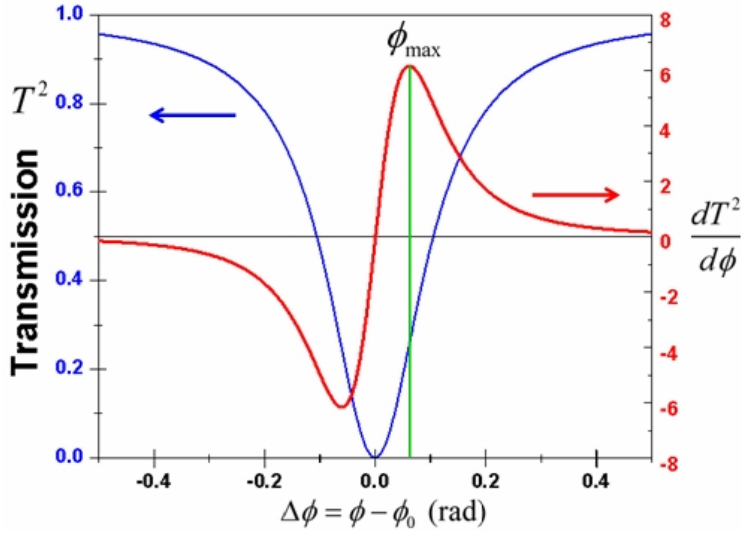

Fig 6: Throughput transmittance (blue line) versus phase detuning near resonance. This plot is for a microring notch filter whose coupling condition is so-called critical coupling and we assume that $\kappa^2 = 10\%$. The slope ($dT^2/d\varphi$) of the transmittance ($dT/d\varphi$) (red line) indicates that the maximum of switching enhancement can be achieved while φ_{max} is located just off resonance of microring resonator.

Inserting this into Eq (35), it gives

$$\left.\frac{dT^2}{d\phi}\right|_{\phi_{max}} \approx \frac{3\sqrt{3}}{8\kappa^2} \tag{37}$$

$\frac{dP_r}{dP_{in}}$, the last term on the right-hand-side of Eq (34), is the power enhancement factor in the ring resonator. Because the ratio of the circulating intensity in the ring to the input intensity is given by

$$\left|\frac{E_{circulating}}{E_{input}}\right|^2 = \left|\frac{E_2}{E_1}\right|^2 = \frac{\kappa^2}{1+\tau^4-2\tau^2\cos\phi} \tag{38}$$

Thus, at $\phi_{\max}$ we got [41]

$$\left.\frac{dP_r}{dP_{in}}\right|_{\phi_{\max}} \approx \frac{3}{4\kappa^2} \tag{39}$$

2.3.2 Intensity-dependent nonlinearity, Kerr effect

For Kerr effect (intensity-dependent nonlinearity), the material refractive index is given as

$$n = n_0 + n_2 I_r \tag{40}$$

n_2 is the nonlinear index of refraction, and I_r is the resonant field intensity in the ring resonator., and n_0 is the linear index of refraction. Thus, the round-trip phase shift is given by

$$\phi = \phi_0 + \frac{n_2 L}{A_{eff}\lambda} 2\pi P_r \tag{41}$$

P_r is the power circulating in the ring resonator, L is the circumference of the ring resonator, ϕ_0 is the linear phase term, A_{eff} is the effective mode area of the ring waveguide, and λ is the wavelength of the input beam. Taking the derivative of Eq (41) with respect to P_r gives

$$\frac{d\phi}{dP_r} = \frac{n_2 L 2\pi}{A_{eff}\lambda} \tag{42}$$

Inserting Eq. (42)(39)(37) into Eq. (34), we got the switching slope of the ring resonator [41]

$$\left.\frac{dT^2}{dP_{in}}\right|_{\phi_{\max}} \approx \frac{9\sqrt{3}}{16} \times \frac{n_2 L \pi}{A_{eff} \lambda} \times \frac{1}{\kappa^4} \propto (FE)^4 \tag{43}$$

As can be seen in Eq. (43), the switching threshold is proportional to the fourth power of the field enhancement factor FE. Equivalently, it is proportional to the square of the finesse $\mathcal{F}$ of the microring resonator because $(FE)^2 = \mathcal{F}/\pi$. What we have discussed on the previous pages has shown that the nonlinear microring resonator has two separate mechanisms of switching enhancement. One is caused by operation of the device near resonance where the slope of the transmission curve is maximum. The other is caused by the field enhancement in the microring resonator. As a whole, these two effects work at the same time to make microring nonlinear response enhanced by the power of FE.

2.3.3 Enhanced nonlinear response due to two-photon absorption in the ring resonator

In section 2-2 and Eqs. (31)(32), we discussed the optical nonlinearity caused by the free carriers generated during the two-photon absorption (TPA) processes. If we inject a pump beam, whose photon energy is above the half-bandgap of ring material, into the microring resonator, let us see what will happen. The free carrier generated during TPA processes is given [8, 21, 41, 47-48]

$$\frac{dN_{fc}}{dt} = \frac{\alpha_2}{2\hbar\omega} I_r^2 - \frac{N_{fc}}{\tau_{fc}} \tag{44}$$

τ_{fc} is the free carrier recombination time or relaxation time, N_{fc} is the free carrier density, I_r is the beam intensity across the optical waveguide. The nonlinear TPA coefficient, α_2, is about 18 cm/GW which was measured by Dr. T. A. Ibrahim in our group [7]. It is found that the carrier lifetime was comparable to the microring lifetime [41].

According to the experimental data in the papers of Dr. Ibrahim [7, 21] and inserting data into Eq.(44), the first term on the right-hand side of Eq. (44) is larger than the second term by 2 or 3 orders of magnitude. So, the second term on the right-hand side of Eq. (44) can be ignored compared with the first term. Eq. (44) is approximated as

$$\Delta N_{fc} \simeq \frac{\alpha_2}{2\hbar\omega} I_r^2 \, \Delta t \tag{45}$$

where Δt is the pulse width of pump pulse circulating in the microring resonator. Thus the index of refraction of the microring resonator is changed by the above free carriers generated during the TPA processes. It is given as [21, 47]

$$\Delta n \approx -\sigma_r \Delta N_{fc} \tag{46}$$

where σ_r is the refractive volume of the material. In terms of Eq. (45), the above equation turns out to be

$$\Delta n \approx -\sigma_r \Delta N_{fc} \approx -\sigma_r \frac{\alpha_2 \Delta t}{2\hbar\omega} I_r^2 \quad \propto I_r^2 \tag{47}$$

To compare the above equation with Eq. (40), $n = n_0 + n_2 I_r$, we can see that the nonlinear index change of refraction due to TPA is proportional to the square of the

incident pump beam intensity circulating in the microring resonator. However, the nonlinearity from the Kerr effect only has a linear dependence on the pump beam intensity. That is, nonlinearity introduced by TPA is dominant over the nonlinearity of Kerr effect. Now let us consider the phase change in the microring resonator only caused by the nonlinearity of the free carriers generated during TPA processes. It is given by using Eq (47) as,

$$\Delta\phi \approx \frac{2\pi}{\lambda} L\left(-\sigma_r \frac{\alpha_2 \Delta t}{2\hbar\omega} I_r^2\right) \approx -L\frac{\pi\sigma_r\alpha_2\Delta t}{\lambda\hbar\omega} I_r^2 \approx -L\frac{\pi\sigma_r\alpha_2\Delta t}{\lambda\hbar\omega A_{eff}^2} P_r^2 \quad (48)$$

where P_r is the beam intensity circulating in the microring resonator, L is the circumference, and A_{eff} is the effective mode area of the waveguide. Taking the derivative of the above equation with respect to P_r gives

$$\frac{d\phi}{dP_r} \approx \frac{d}{dP_r}\left(-L\frac{\pi\sigma_r\alpha_2\Delta t}{\lambda\hbar\omega A_{eff}^2} P_r^2\right) \approx -L\frac{2\pi\sigma_r\alpha_2\Delta t}{\lambda\hbar\omega A_{eff}^2} P_r \quad (49)$$

Inserting Eqs. (49) (37) (38) and (39) into Eq (34), we obtain the switching slope of the microring [7, 41, 47]

$$\left|\frac{dT}{dP_r}\right|_{\phi_{\max}} \approx K\frac{1}{\kappa^6} \quad where \;\; K = \frac{27\sqrt{3}}{64} \times \frac{\pi L\sigma_r\alpha_2\Delta t}{\lambda A_{eff}^2\hbar\omega} \times P_i \quad (50)$$

By re-writing Eq (50) as a function of the resonator field enhancement FE [7, 41, 47] we get.

$$\left|\frac{dT}{dP_r}\right|_{\phi_{\max}} \approx \left(FE\right)^6 \quad (51)$$

From the above equation, we see that we can obtain an enhancement determined by the sixth power of the microring field enhancement FE when TPA processes in the microring resonator are used for pump-and-probe experiments. For the discussion on the previous pages, we neglected the nonlinearity of Kerr effect, because we mentioned that nonlinearity introduced by TPA is dominant over the nonlinearity of the Kerr effect. We also assume that the round-trip loss in the microring resonator is constant and we neglected the nonlinear loss contribution. If significant nonlinear loss appears, the round-trip loss will vary with time. At the same time the critical coupling condition of the microring resonator will also be destroyed and the enhancement effect of switching due to different mechanisms will be reduced.

Chapter 3: Fabrication of semiconductor microring resonators

I will discuss the fabrication processes which have been used to make semiconductor microrings in clean rooms. The microrings I used for experiments on "cascade photonic AND logic gates" are vertically coupled GaAs microrings which were made by Dr. Tarek Ibrahim. I was a contributor to some portions of his microring fabrications in the clean room. For many years I had worked on GaAs microring fabrications together with Dr. Ibrahim in clean rooms. The whole processes for GaAs microring fabrications will be discussed in the following.

3.1 Wafer layer structure of GaAs microring resonators

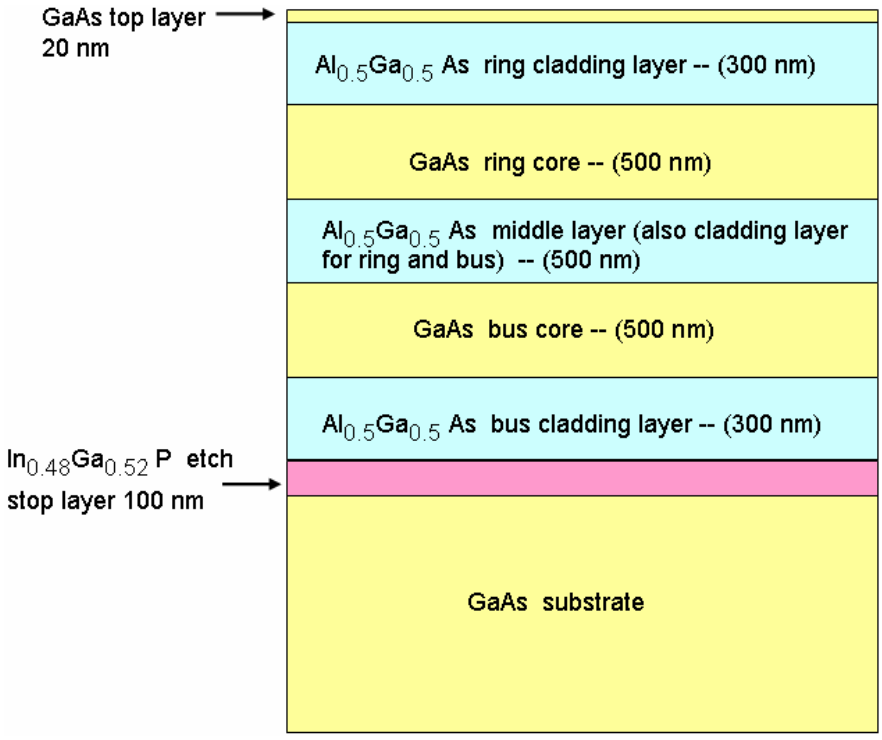

Fig 7: Wafer layer structure of GaAs microrings

Fig 7 is the wafer layer structure of GaAs microrings.

3.2 Fabrication steps of vertically-coupled GaAs microring

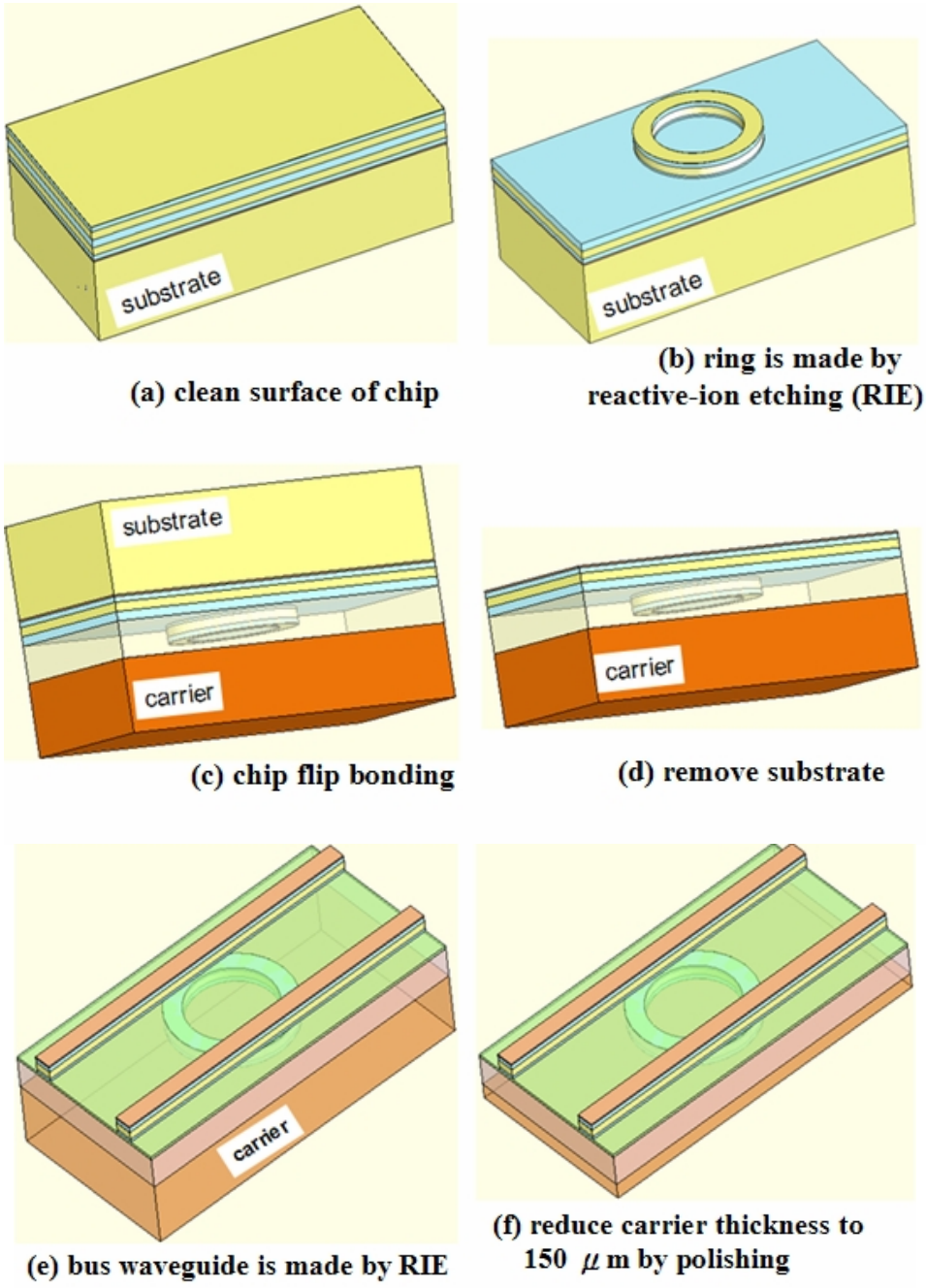

(a) clean surface of chip

(b) ring is made by reactive-ion etching (RIE)

(c) chip flip bonding

(d) remove substrate

(e) bus waveguide is made by RIE

(f) reduce carrier thickness to 150 μm by polishing

Fig 8: Schematic for the fabrication steps of vertically coupled GaAs microresonator.

3.2.1 Clean sample, photolithography, dry etch, make ring

Firstly, the GaAs wafer is cleaned by using acetone, methanol, and isopropanol on a wet processing deck (Fig 8a). Photoresist, OIR 906-10, is spread uniformly on the chip using a spinner of 3500 rpm for one minute. The thickness obtained in this way is 1.1 μm. The chip is then heated on a hot plat at temperature 90°C for one minute in the pre-baked process. Then the chip is put in the projection aligner machine for photolithography. After this is done, the chip is put on a hot plate at higher temperature 120°C for one minute for the post-baked process. After this the chip is put in developer solution, OPD 4262, for one minute. Use deionized water to rinse it and air-blow chip with nitrogen.

Use reactive-ion etching (RIE) machine to do a dry etch on the chip. There are some alignment keys and Vernier marks on each optical mask. Alignment keys are helpful for alignment between ring resonator level and bus waveguide level. Vernier marks are used to measure the misalignment between different levels.

3.2.2 Chip flip bonding, sample transferred to carrier

After ring resonator has been etched by RIE (Fig 8b), next step is chip flip-bonding (Fig 8c). Use another GaAs chip of same size to be carrier. Sample chip will be transferred to this carrier. Before transferring, adhesion promoter (AP 3000) spreads uniformly on this carrier using a spinner. Put one drop of benzocyclobutene (BCB) on the carrier and bring sample on carrier slowly with ring resonator side downward. Pay attention to the alignment between carrier and sample. Align them roughly by checking their crystal axes. Very gently press sample when sample is slowly put on carrier. After

this step, bring the whole assembly (carrier and sample) into a furnace for curing BCB polymer. Then sample will stick to carrier firmly.

3.2.3 Remove substrate－reduce thickness by polishing, wet etch, selective etch

The next step will be removing the substrate of sample (Fig 8d). Use lapping machine to remove the substrate of sample gradually. The thickness of substrate is reduced from about 650 μm to 150 μm. The remaining 150 μm substrate is removed by wet etch. This wet etch will stop at the etch stop layer, InGaP (100nm). Then, in order to remove this etch stop layer (InGaP) a selective etch is applied to it. When all of these steps are complete, removing substrate is finished (Fig 8d).

3.2.4 Clear alignment keys and Vernier marks for better alignment at next step

Before going to make the bus waveguide, we need to clear alignment keys and Vernier marks in order that they can be seen clearly under microscope and alignment of bus waveguide with ring resonators on the another side of sample will be easier for projection aligner machine. The total thickness of all epilayers is 2.1 μm. Before removing substrate, the etch depth of epilayer has already been reduced to 0.95 μm. The thickness of mid-layer is 0.2 μm. This thickness of 0.2 μm is enough for offering mechanical strength as well as coupling between ring and bus waveguides.

For clearing alignment keys and Vernier marks, photoresist is spun on sample and windows are patterned on photoresist of sample. We use RIE or ICP to etch down through those windows and etch stops at the mid-layer. After this step, alignment keys

and Vernier marks on the bottom side can be seen clearly from the top using the projection aligner machine. This is helpful for aligning ring resonators on bottom side and bus waveguides on top side.

3.2.5 Make bus waveguides

Then we use the similar processing methods on the bus waveguides of top side as we did previously for ring resonators on bottom side (Fig 8e).

3.2.6 Reduce final thickness of sample, inscribe sample, cleave sample

The final step is to reduce sample thickness down to 150 μm using wet etch and to cleave sample into stripes of about 500 μm wide (Fig 8f). When the total thickness of sample is reduced down to 150 μm, it is easier to cleave it. Then we mount sample on the stage of the inscriber which has vacuum suction holes on its stage. Vacuum is applied through the vacuum suction holes to hold sample to the stage. Use tip of inscriber diamond blade to inscribe sample along crystal axes of substrate. We inscribe chip every 500 μm width. That is, the separation between adjacent scribe lines on sample is 500 μm. After this is done, we put sample on the tip of a razor blade and align scribe lines with razor blade under microscope. Slightly press down sample from both sides. Sample will break along scribe line and separate into many bars whose width is 500 μm. These bars will be mounted with metal-based epoxy on end facet of a narrow copper plate for optical experiments.

3.2.7 Anti-Reflection Coating

The optical spectrum of microring resonator shows many Fabry–Pérot resonances.

The reason is that the two cleaved end facets of bus waveguide on chip cause this effect. Fabry–Pérot resonance is determined by the length of the bus waveguide. For reducing the Fabry–Pérot resonances, anti-reflection coating is used to reduce the reflection from both facets. The refractive index of this coated material is required to have value $n = \sqrt{n_{GaAs} \times n_{air}} = \sqrt{3 \times 1} = 1.73$. We used the electron-beam evaporator to deposit a thin layer of 240 nm aluminum oxide, Al_2O_3, on both facets of each GaAs bar. Then, an ellipsometer was used to measure the optical constants of this deposited thin layer of aluminum oxide Al_2O_3. The value of the refractive index of Al_2O_3 is 1.62. After anti-reflection coating was applied to GaAs bars, the power reflectivity of facets dropped from 25% to 2% according to the experimental results from Dr. Ibrahim.

Chapter 4: Cascaded photonic logic gates by using two symmetric GaAs microring resonators

Previously Dr. Ibrahim had worked on a few experiments on single photonic logic gates using single semiconductor microring resonators [7-9]. After his graduation, I continued this project. That is the experiment of cascaded photonic logic gates using multiple microrings which can offer us the ability to perform more and more complex operations involving photonic logic gates. This experiment is the building block of multi-stage photonic logic gates. It is the key and important step for the future application of photonic logic gates in industry and commercial products. We will discuss it now.

4.1 Operation principle of one photonic logic gate using one ring

The theory of the enhancement effect of optical switching using microring resonators has already been discussed in chapter two. The basic schematic of a photonic logic gate using a microring is shown in Fig 9. A control pulse is launched into the upper waveguide at wavelength λ_1 and a probe beam is launched into the lower waveguide at wavelengthλ_2. If control pulse (λ_1) is right on resonance with the microring (Fig 10b), the refractive index of the microring changes due to carriers generated during two photon absorption processes and resonances also shift (Fig 10c). This shift of resonances also works for probe beam (λ_2) and shifts the probe beam off resonance in the microring.

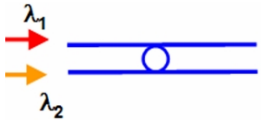

Fig 9: Schematic for the operation of microring to work as photonic logic gate.

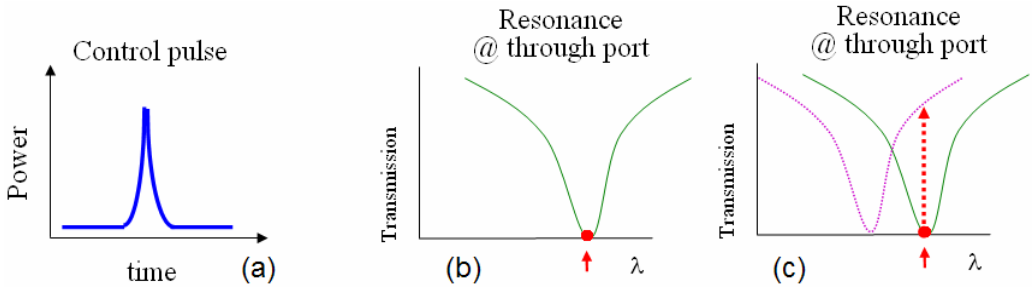

Fig 10: Operation for the case that pump beam is on resonance and signal is also on resonance initially.

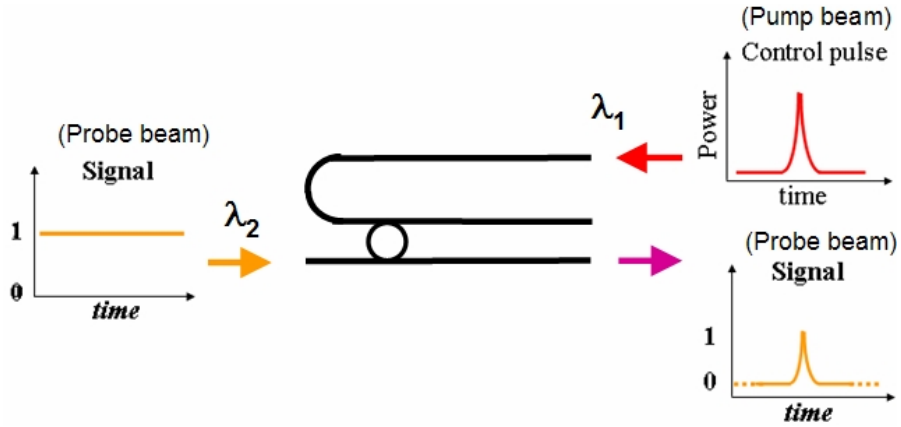

Fig 11: Schematic for pump-and-probe operation using single microring resonator.

In Fig 11, pump beam (control pulse) is launched into upper bus waveguide at λ_1 and probe beam (signal) is launched into lower bus waveguide at λ_2 . According to the operation principle explained previously, the probe beam (signal) at through port of lower bus waveguide will be switched on. This operation of microring as a logic gate works as an AND gate in this case. The upper waveguide is bent and designed for matching the separation of an array of lensed-fiber couplers in Fig 12. The separation between adjacent lensed-fiber tips is 250 μm. The discussion above is for operation of single photonic logic gate using one microring resonator. If one more microring is added (that is, one more logic gate is added), its schematic is shown in Fig 13. The second microring works as a

second logic gate. The second pump beam (control pulse) is launched into the lower bus waveguide on the left side and is on resonance with the second microring resonator. If the probe beam (signal) passes through the first microring and reaches point X in the schematic, it would be controlled by the second pump beam (control pulse).

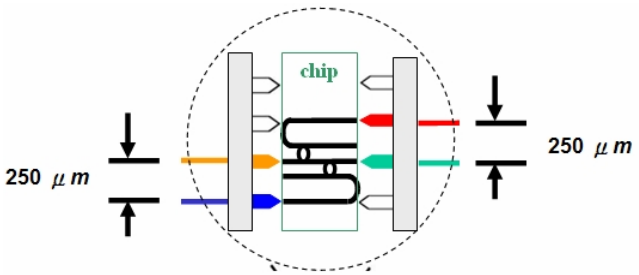

Fig 12: Schematic for the microring chip with two fiber arrays respectively approaching it on both sides of chip for coupling process.

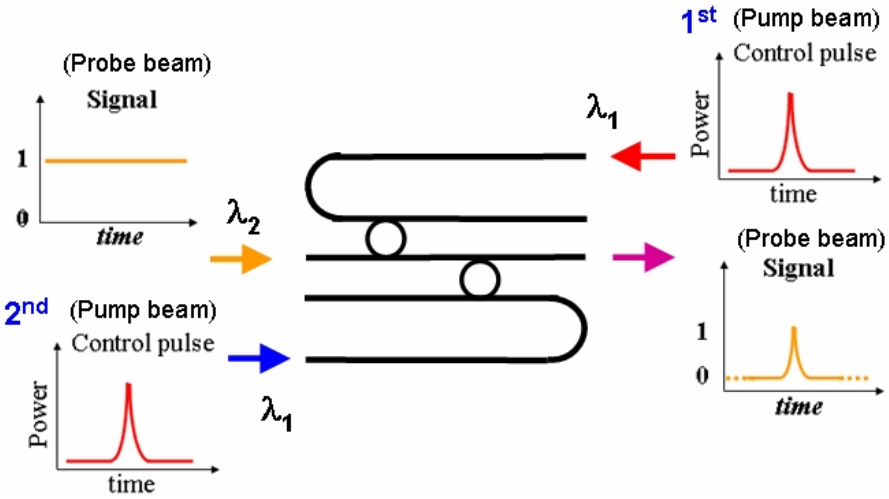

Fig 13: Schematic for pump-and-probe operations in cascading two AND logic gates using two symmetric microring resonators.

The details and operation of experiments on this cascaded photonic logic AND gates using 2 microrings will be discussed in the following sections.

4.2 Experiment on cascaded two photonic logic AND gates by using two symmetric GaAs microrings

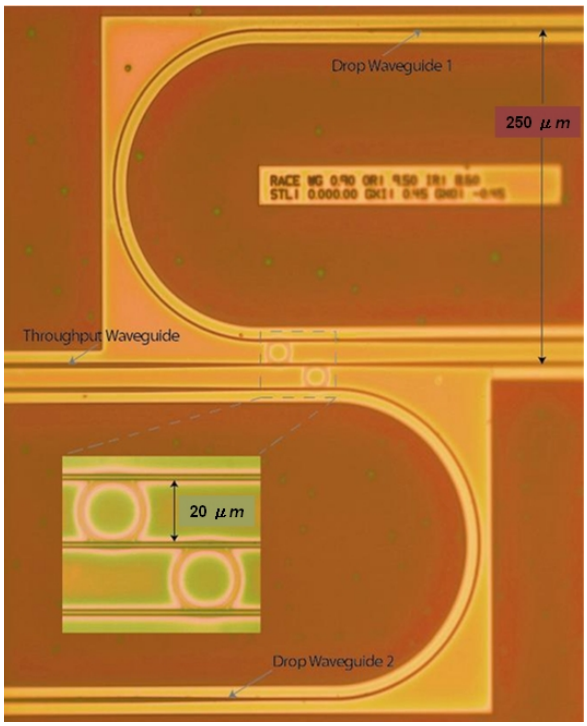

Fig 14: SEM photo of two photonic logic AND gates on chip. These two GaAs microrings are symmetric and their diameter is 20 μm.

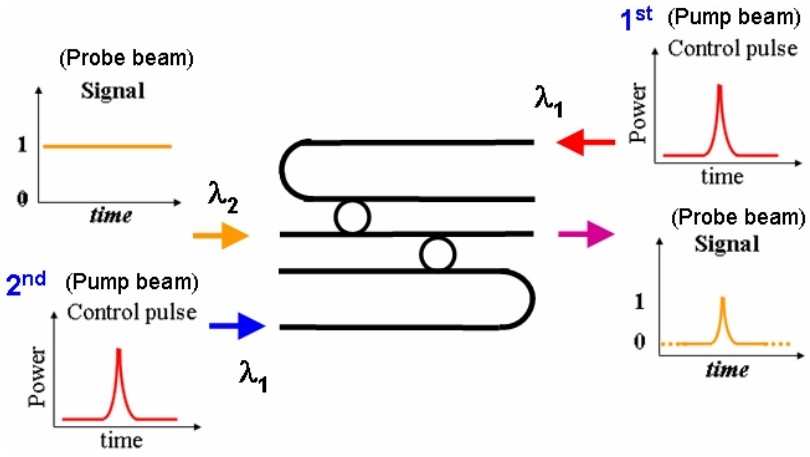

Fig 15: This schematic is placed here again for convenience to compare with Fig 14.

I conducted this experiment using two symmetric GaAs microring resonators offered by Dr. Ibrahim. Fig 14 shows the layout of two microring resonators on chip. Fig 14 and Fig 15 are placed together on the same page for convenience to compare. In Fig 14, the diameter of microrings used for my experiments is 20 μm. These two GaAs-AlGaAs microrings are closely matched and integrated on the same chip. The mismatch of resonant wavelengths between two microrings is less than 0.1 nm for resonance at 1558.6 μm.

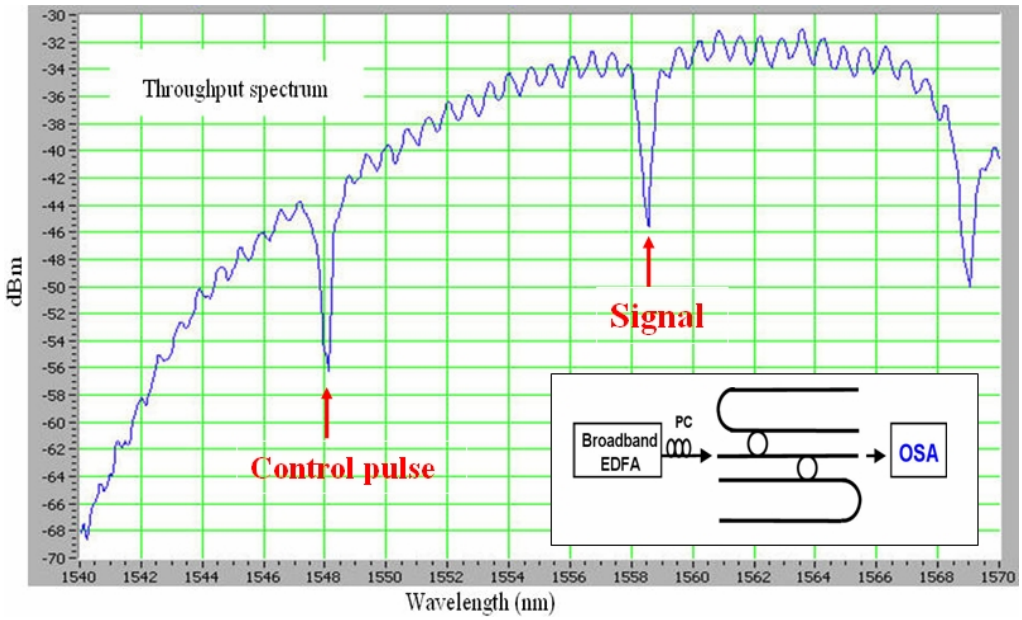

Fig 16: Transmission spectrum measured at the middle through port. Control beam and signal are centered at different wavelengths. Control beam is centered at 1548.06 nm and signal is centered at 1558.6 nm. Free spectral range is 10.54 nm.

These two microrings have a free spectral range of 10.54 nm, 3-dB bandwidth of 0.42 nm and 0.6 nm (Fig 16), finesses of 25 and 18, field enhancements (FE) of 5 and 4.2, round trip losses of 7% and 11%, coupling coefficients of 35% and 40%, respectively. Half bandgap of GaAs is close to the photon energy of light of wavelength 1550 nm. As

discussed earlier in chapter 2, pump beams of 1558.6 μm are absorbed through two-photon absorption (TPA) inside the microring resonators and free carriers generated through TPA process change the refractive index of microring resonators. According to Eq (9) of chapter two, free carriers are generated

$$\frac{dN_{fc}}{dt} = \frac{\alpha_2 I_r^2}{2\hbar\omega} - \frac{N_{fc}}{\tau_{fc}}$$

The effective carrier lifetime τ_{fc} is about 35 ps, reported in [7]. According to transmittance experiments on straight GaAs waveguides, TPA coefficient α_2 is about 18 cm/GW [7]. The surface recombination of free carriers at the sidewall and carrier diffusion determine the effective carrier lifetime. The free carriers generated through TPA change the refractive index of the microrings according to $\Delta n = -\sigma_r N_C$, where Δn is the refractive index change and σ_r is the refractive volume of the material whose value is around $1\times10^{-20}\ cm^3$ [7]. According to the above equation and $\Delta n = -\sigma_r N_C$, the estimated intensity required to make a spectral shift of 0.2 nm (~ 0.5 FWHM) in the ring is 12 GW/cm^2.

4.3 Experimental Setup

Fig 17 is the experimental setup for cascading logic AND gates using 2 GaAs microrings.

One continuous-wave (CW) pump beam is tuned to the resonant wavelength (1558.6 μm) of the microring. This CW pump beam is modulated externally by a pattern generator. The repetition rate is 30 MHz. Then the pump beam is equally split into two beams, pump A and pump B, by a 50/50 fiber coupler. Two pump beams are amplified

by EDFAs and filtered with band-pass filters. The first pump beam, A, is launched into one port of the first microring, which will work as the first logic AND gate. The second pump beam, B, is launched into one port of the second microring, which will work as the second logic AND gate.

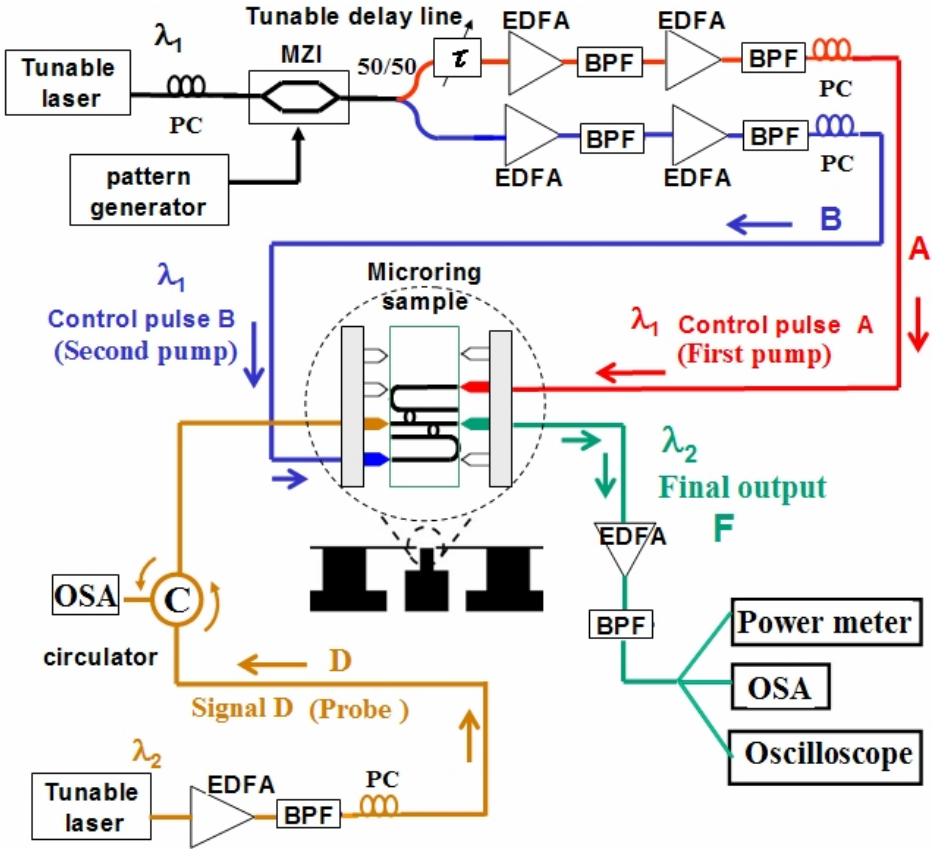

Fig 17: Schematic of the experimental setup for cascading two photonic logic AND gates by using two symmetric GaAs microrings. PC: polarization controller, MZI: Mach–Zehnder interferometer, EDFA: Erbium Doped Fiber Amplifier, BPF: Band Pass Filter, OSA: Optical Spectrum Analyzer. Probe beam, D, is CW and has power of 10 mW at the device input. The output power of tunable laser is 5 mW for pump beam. The switching energy (pulse energy) for pump A and B at the device input is 18 pJ/pulse.

In this experiment pump A and B have repetition rate of 30 MHz, pulse width of 75 ps, wavelength of 1558.6 μm, and switching energy of 18 pJ/pulse at the device input. The output power of tunable laser (light source) is 5 mW for pump beam. Probe beam, D, is launched into the middle bus waveguide (Fig 17). At the device input the probe beam, D, is CW and has power of 10 mW.

We collect output probe, F, at the output port of the middle bus waveguide on the right side of the microring sample with a lensed-fiber coupler. An EDFA is used to amplify output probe and band-pass filter is tuned to the wavelength of output probe. In the end a power meter, OSA, or oscilloscope can be used to measure output probe

4.4 Operation principle of cascaded AND logic gates using 2 GaAs microrings

In section 4-1, operation of a **single** logic gate using one ring has already been discussed. Now we will show the operation principle of cascaded logic AND gates using 2 GaAs microrings. Its experimental setup is shown in the previous section.

We put Fig 15 here as Fig 18 **a**. Fig 18 **b** is logic gate representation of Fig 18**a**. This shows cascaded logic AND gates. It has 3 inputs (A, B and D) and one output (F). The output probe of the first AND logic gate is D′. The final output probe of the second logic AND gate is F. The input probe, D, is switched on or off manually because one of two ultra-high frequency facilities was broken and only one was available. Fig 19 has five sub-figures. The sub-figures on the first raw show the results after the first ring and the second ring respectively while CW probe, D, is switched on manually. The sub-figures on the second raw show the results while CW probe, D, is switched off manually.

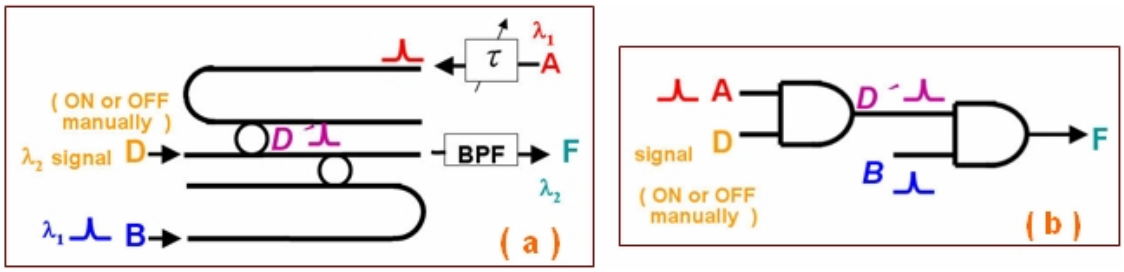

Fig 18: Schematic of experimental setup and its logic gate schematic are placed together for convenience to reference to each other. Probe beam, D, is CW and has power of 10 mW at the device input. The switching energy (pulse energy) for pump beams A and B at the device input is 18 pJ/pulse.

In section 4-1, we have already discussed the operation principle of a single ring working as a single logic gate. Now we continue to discuss the operation principle of cascaded logic AND gates using two GaAs microring resonators.

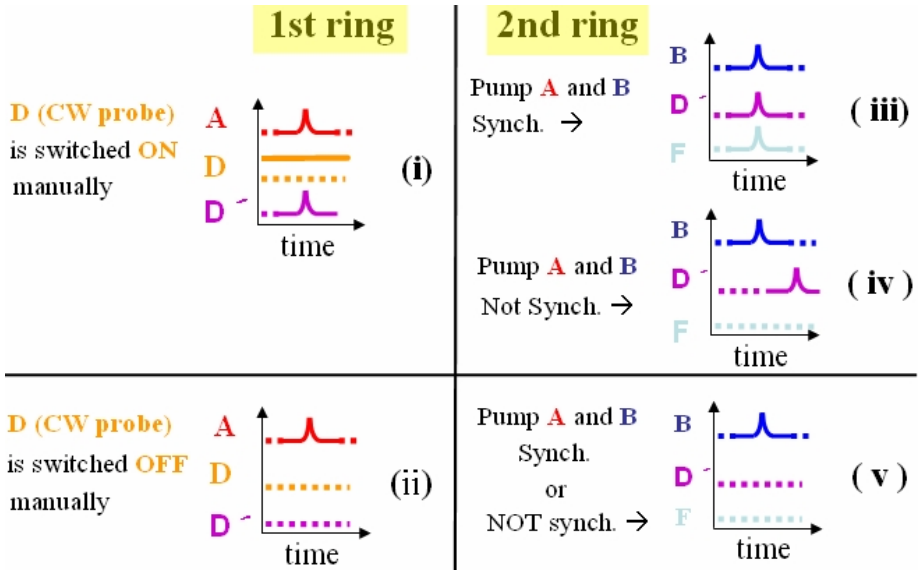

Fig 19: Schematic for explaining the operations of the first and second AND logic gate using two single microring separately.

In Fig 19 (i, iii, and iv), the CW probe is switched on manually. The first pump pulse 'A' and CW probe are non-zero. The result of the first photonic logic gate is '1' (D'). This is logic AND gate operation. For the second ring operation, its result will be '1' if pump pulse A is synchronized with pump pulse B.

A	D	B	F
1	1	1	1
1	1	0	0
1	0	1	0
1	0	0	0
0	1	1	0
0	1	0	0
0	0	1	0
0	0	0	0

Fig 20: Truth table for cascading two photonic AND logic gates by using two symmetric GaAs microrings.

This is shown in Fig 19 (iii). That is, probe beam D' will be switched out of resonance of the second ring optically by the second pump pulse B and will reach the final output port F, which can be seen in Fig 18α. For this case the second ring works as a logic AND gate. If pump pulse A is NOT synchronized with pump pulse B, probe beam D' will not be switched out of resonance of the second ring and will NOT be able to reach the output port F, which is shown in Fig 19 (iv).

In Fig 19 (ii and v), the CW probe is switched off manually. There is no doubt that at the final output port F there will be no signal appearing. The above logic gate operations are also shown on the truth table in Fig 20. Readers can see these operations easily and clearly in Fig 21. In the left column, pump pulse A and B are not synchronized with each other.

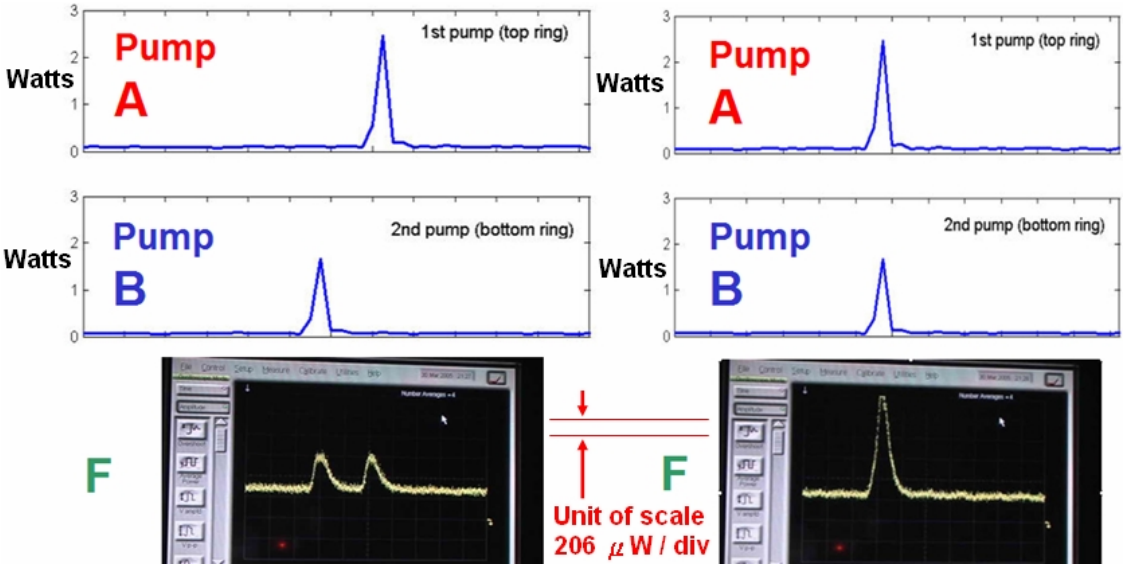

Fig 21: The unit of vertical scale for pump A and B at device input is watts. The unit of vertical scale on the screen for signal, F, measured at final output port is 206 μW. Schematic of signal at the final output port F for different cases of synchronized and un-synchronized input pumps, A and B. Left part is for un-synchronized input pumps, A and B. Right part is for synchronized input pumps, A and B. The switching energy (pulse energy) for pump beams A and B at the device input is 18 pJ/pulse. The estimated intensity required to make a spectral shift of 0.2 nm (~ 0.5 FWHM) in the ring is 12 GW/cm^2 according to the calculation in section 4.2.

On screen of oscilloscope in the left column we see that two very small pulses appear at the final output port and they are not synchronized. While the delay line (in Fig 18) is slowly tuned to synchronize both of two pump pulses (the right column), the pulse at the final output port F becomes much larger (about four times the value of pulse in the left column). This also corresponds to Fig 19 (iii).

4.5 Results and discussion

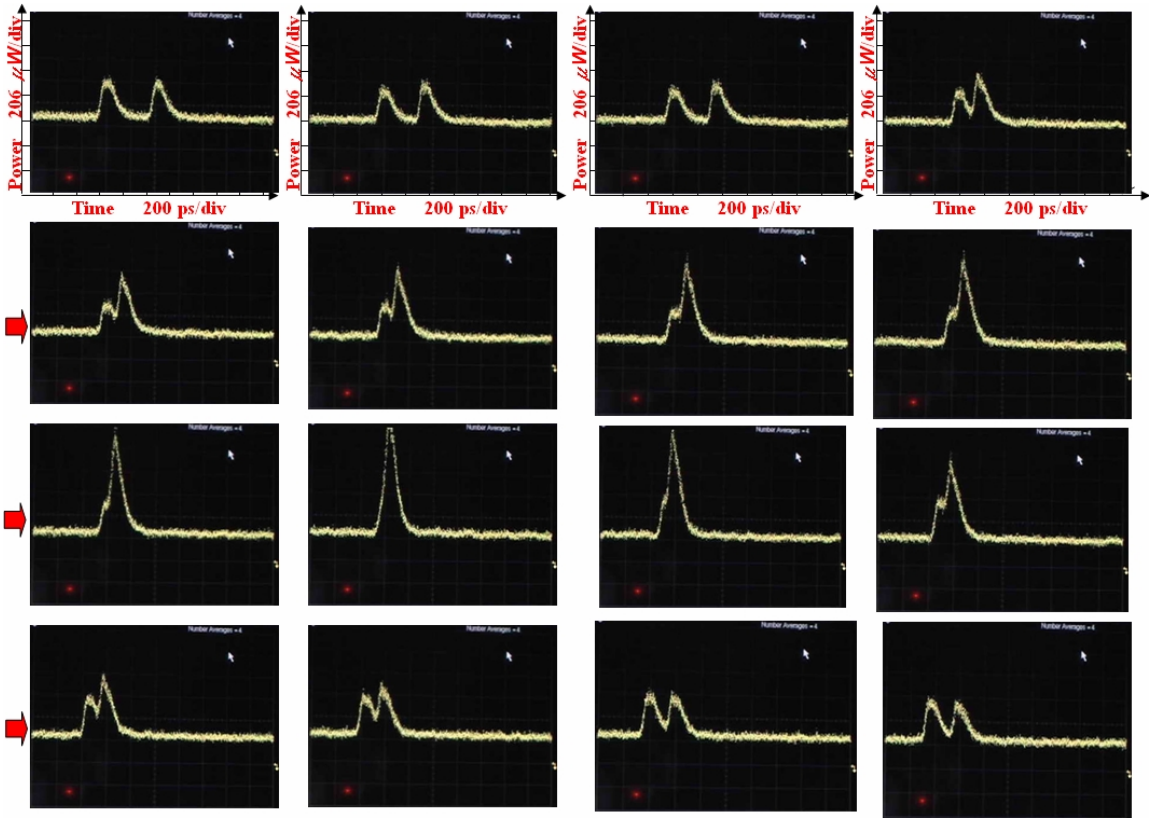

Fig 22: The unit of vertical scale shown in the first row is 206 μW. The unit is same for all the photos. A succession of photos captured from the video images recording the process of switching during experiment of cascading two AND logic gates. The order is from left to right and top to bottom sequentially.

This work was presented at CLEO in 2006 [48]. In Fig 22, there are 16 photos which are captured consecutively and continuously from a movie of the experiment. This movie recorded the variation of two pulses at the final output 'F' shown in Fig 18 **α.** The order of photos is from left to right for each raw photo. Two photos of Fig 21 are from this movie also. Right at the beginning two pump pulses A and B are not synchronized. While delay line (in Fig 18) is tuned to make both of A and B synchronized, the output pulse 'F'

becomes much larger (about four times the value of pulses in the first photo of first rawest of photos). It means that this output pulse for pump pulse A and B to be synchronized corresponds to '1' state of cascaded logic gates of 2 ANDs. If pump pulse A and B are not synchronized, output pulse will be very small, which corresponds to '0' state of cascaded logic gates of 2 ANDs.

As for the threshold switching power in Fig 21, pump A controls the first ring and pump B controls the second ring. As can be seen in the first photo of 4-th raw, the peak value of pulse at output port is about 5 units (206 μW/div X 5 = 1030 μW) when pump A and pump B are synchronized. If pump A and pump B are not synchronized, the peak value of pulse at output port is about 2 units (206 μW/div X 2 = 412 μW). So the threshold of switching power in Fig 21 and Fig 22 is 40 % (412 μW/ 1030 μW= 40%).

As shown from the above experimental results, two symmetric GaAs microrings can work as cascaded photonic AND logic gates. This experiment result shows that to cascade more and more logic gates by using semiconductor microrings is feasible. It is an important step for the future application of photonic logic gates in engineering, industry, and commercial products.

Chapter 5: Glass microresonators

5.1 Motivation: to build on previous work on semiconductor microrings

Since I started to work on semiconductor microrings, I have carried out each step of the fabrication, optical switching experiments using microrings, and related research. The experiments on optical switching using micro-rings were already discussed in chapter 2 through chapter 4. After having worked on semiconductor micro-rings for years, we found that semiconductor and polymer microresonators made by photolithographic facilities in a clean room had many drawbacks. The yield rate was 10% at most in our lab at LPS and it generally required costly facilities in clean room. The sidewall surface quality of the semiconductor microrings made by photolithographic facilities was not excellent and produced significant scattering loss. Besides, the initial fabrication of semiconductor microrings in our lab generally took many years to complete before the first batch of successful devices was obtained.

Since microresonators were invented decades ago, most people have used semiconductor photolithographic facilities to fabricate micro-resonators. Some researchers tried other approaches to fabricate micro-resonators [60-73]. We tried to come up with an innovative method to increase the yield rate, improve the surface quality of sidewall, and shorten the total time of fabrication. In this chapter I will describe my new method and at the end of this chapter the experimental results will be discussed.

Owing to funding shortage and no available polishing systems from industry specific for polishing glass micro-resonators in mass production, we designed, developed,

and built up the whole system on our own. In Appendices we will discuss the designs of our new system and facilities created specifically for this new method.

5.2 Introduction of highly polished glass microresonator

5.2.1 Advantages of this new method

Because of the reasons listed on the previous page and funding shortages, we proposed an innovative fabrication method for glass microresonators using a special polishing process. According to our final experiment results using this method, it has many advantages. We list them below:

(i) Fast fabrication (6 weeks. It can be within 2 weeks if optimized in the future),

(ii) High yield rate of above 50 % (it can be above 90 % if optimized in the future), (yield rate: the percentage of devices w/o cracks on edge)

(iii) Large quantity production (800~1200 devices per batch), it can be more if optimized in the future.

(iv) Surface quality should be excellent (our glass capillaries were made at temperature $\geqq$1000℃ and devices were polished by suspension slurry of 70 nm colloidal silica. Further measurements that are beyond our current capability are needed for final verification.).

(v) Low cost. No need to use facilities in semiconductor clean room.

5.2.2 Requirement: to build a whole system specific for glass microresonator

The required facilities are an ultra-long puller, glue-on facility, work cylinder, work rings, workpiece fixtures, stainless steel polishing plates, flexible swing jig holders for wok rings of different sizes, conditioning plate for polishing machine, abrasive disk holder, DC motor controller, and take-out facility. The designs and engineering drawings of the whole system are shown in Appendix 1 and Appendix 2. Some discussion is also contained in Appendices. Here we will describe the steps of this new method first.

5.2.3 Flow chart of this new method

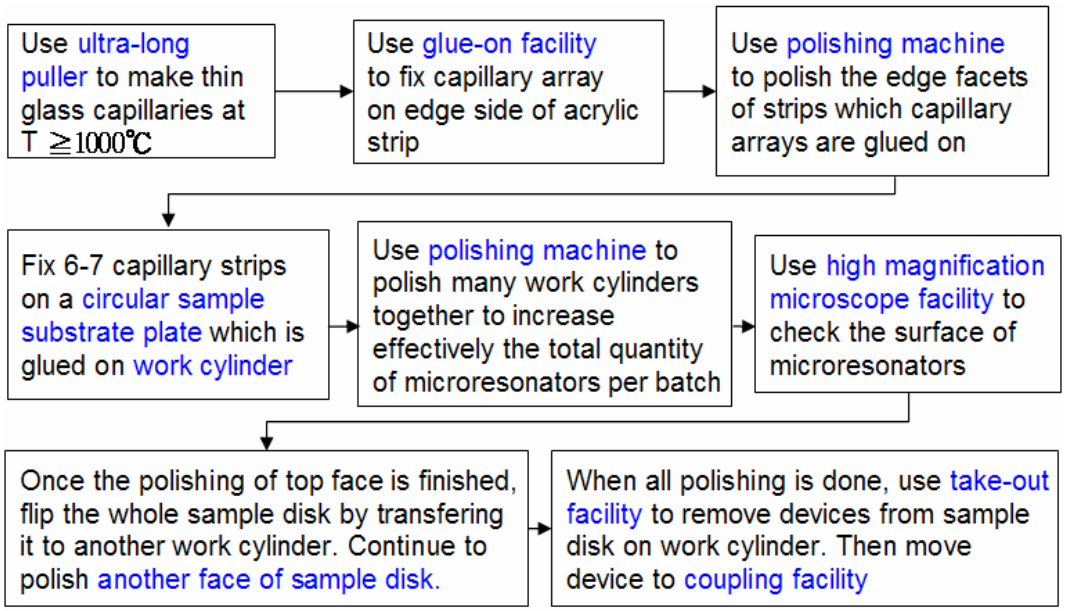

Table 1: Flow chart of the fabrication steps of this new method, highly polished glass microresonators.

Table 1 is the flow chart. The details of each step are discussed in the following.

5.3 Fabrication steps of glass microresonators

(1) Make glass capillaries using the ultra-long puller

First we inserted one 10 cm long glass tube of diameter 3 mm in the vertical ultra-long puller machine (Fig 23c) we designed and made, which is 75 cm tall, and gently fixed its two ends on the machine (Fig 23a). We brought a torch close to the glass tube and let the flame of torch cover the central portion of the glass tube for a few tens of seconds (Fig 23b). Because the temperature was above 1000 ℃, the glass tube became soft. We used tweezers to gently squeeze the melted tube and made its cross-section close to a racetrack shape, which will be good for coupling due to longer coupling length. Then we released the lower fixture of the puller machine to let the bottom sliding block free fall to the lowest point. We let the thin glass capillary cool down for a few tens second and then took the whole glass capillary out. We used a diamond knife to cut the whole capillary into many shorter sections which are easier to store in a plastic dish.

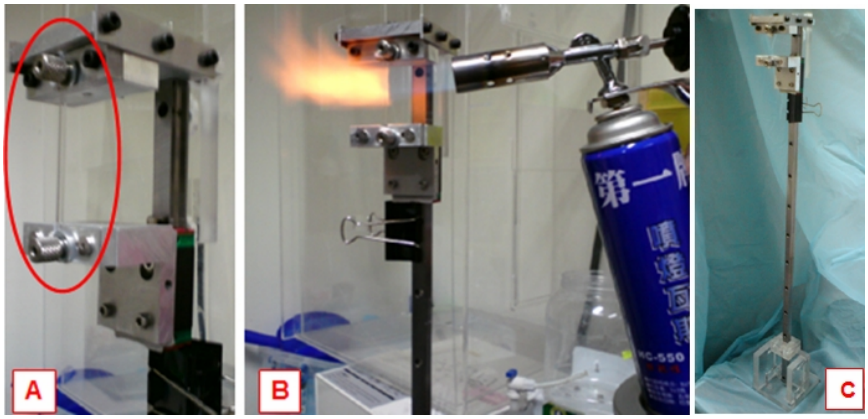

Fig 23: Photos for ultra-long puller of capillary. Initially a glass tube is fixed and heated up to get melted at high temperature ≥ 1000 ℃.

(2) Bundle glass capillaries into an array fixed on carrier plate

For this step, we bundled one array of glass capillaries and fixed them on glass or acrylic plates (Fig 24a and Fig 24b). This capillary-array carrier made it easier for the following steps.

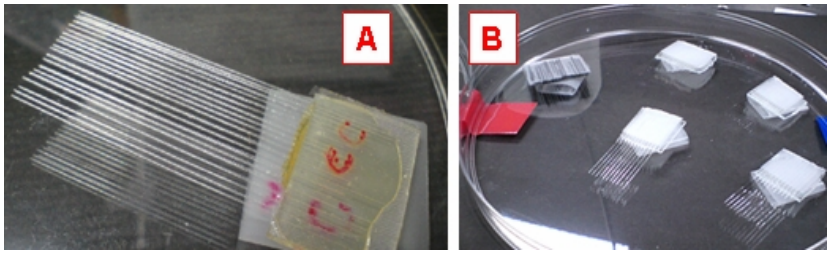

Fig 24: One array of glass capillaries fixed on plate using epoxy. One Petri dish can contain a few arrays of capillaries.

(3) Fix each array of capillaries on the edge face of acrylic strip

We put a few capillary-array carriers on the glue-on facility we made (Fig 25a) for glue to firmly fix capillaries on the edge facets of acrylic strips. When glue solidified (Fig 25b), we used a diamond knife to cut it and removed them from the glue-on facility. We stored them in a plastic dish for future usage (Fig 25c).

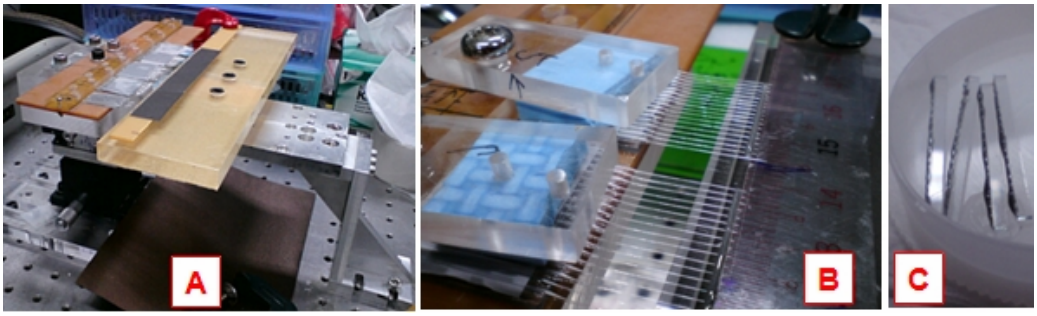

Fig 25: (a) photo of our glue-on facility (b) Enlarged view of two arrays of glass capillaries prepared to be fixed on the edge facets of acrylic strips using epoxy.

(4) Polish both of the edge faces of each strip

We used a polishing machine to polish both of the edge faces of the glass capillaries (Fig 25c) fixed on acrylic strips. This step will let each strip lie on the carrier disk horizontally (Fig 26a, Fig 26b, Fig 26c).

(5) Fix 6~7 strips on the top of carrier disk glued on the work cylinder

The acrylic strips of glass capillaries (Fig 26a) will be fixed on the top face of a carrier disk, which sits on the top of a work cylinder (Fig 26b and Fig 26c). Fig 26b is the isometric view.

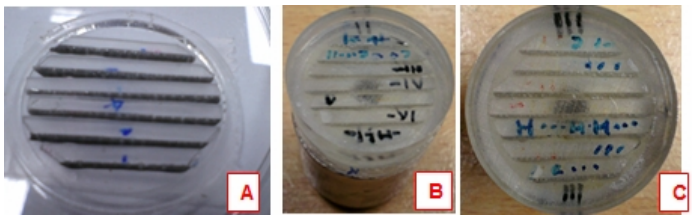

Fig 26: (a) six acrylic strips with capillary array fixed on it. (b) (c) photos for different view angles of capillary arrays fixed onto work cylinder.

The carrier disk under the strips is used to transfer devices to another work cylinder after the polishing work of the top face is finished. This will be discussed in the following. Each work cylinder can support 6 to 7 strips of glass capillaries fixed on it. The total number of glass capillaries each work cylinder can support depends on the density of capillaries we arranged.

Fig 27: Photo for six work cylinders. Each with many capillaries fixed on it.

In general each work cylinder can support up to 200 capillaries. Fig 27 shows six work cylinders for processing.

(6) Polish 4~6 work cylinders simultaneously using a set of facilities we designed

We designed two work piece fixtures and two work rings for disks and pads of different sizes.

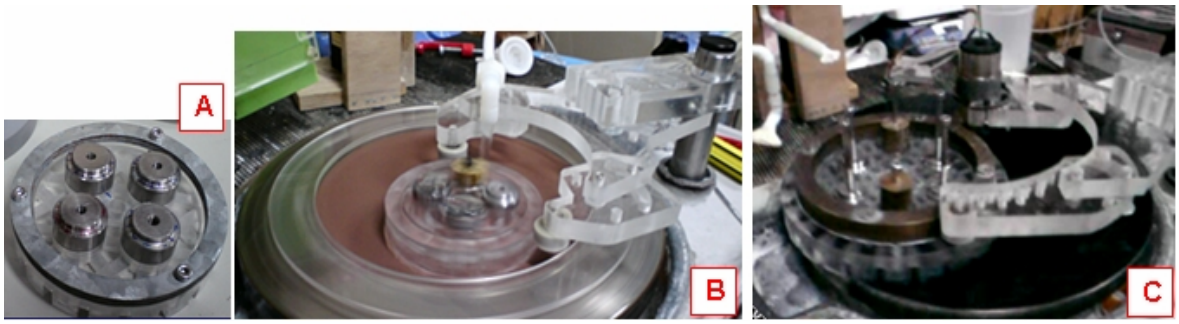

Fig 28: (a) Small workpiece fixture (b) polishing of small workpiece fixture is operation. (c) final polishing with large workpiece fixture is running.

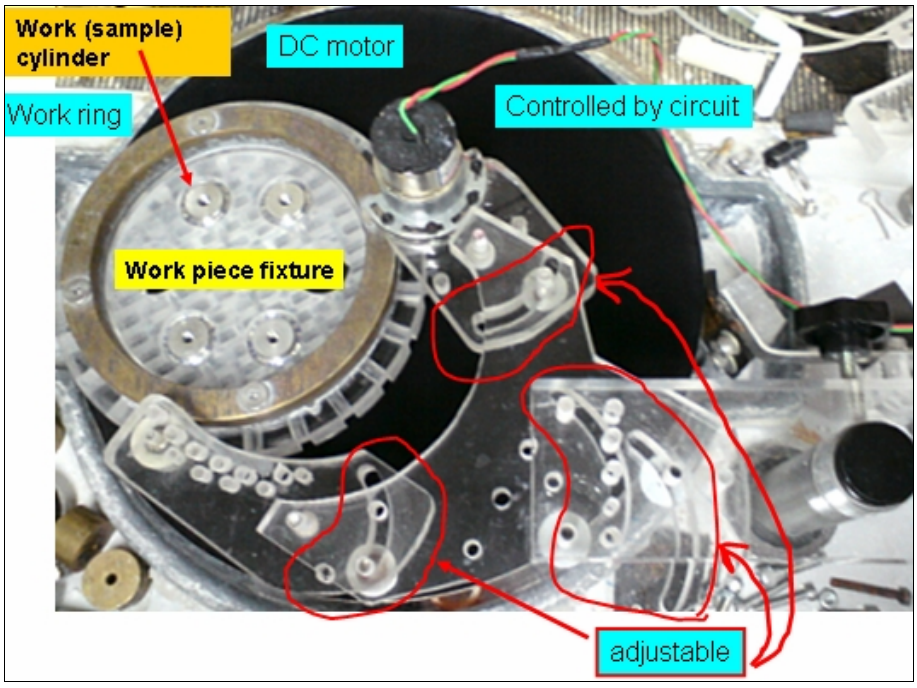

Fig 29: Top view of the whole system we designed and made. The flexible swing jig holder with DC motor fixed on its right arm is shown clearly here.

The smaller one is for abrasive disks of 8 inch diameter (Fig 28a and Fig 28b). The bigger one is for final polishing pad of 12 inch diameter. The smaller one can support 4 work cylinders and the bigger one can support 6 work cylinders (up to 8 work cylinders) which is shown in Fig 28c. Fig 29 is the top view of the whole system we designed and made specifically for the new method of highly polished glass microresonators.

(7) Polish with abrasive disks ranging from large to small grit sizes

In the polishing process the abrasive disks start from grit size 20 or 15 um down to 1 um. For every step or at any time, we measured the height variations by using a height gauge stand with a digimatic indicator. For the final polishing step, we use a polishing suspension that is a 70 nm colloidal silica slurry.

(8) Transfer capillary layer to another disk carrier and flip capillary layer

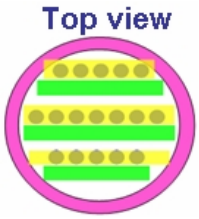

Fig 30: Top view of the layout of capillary arrays fixed on top of work cylinder.

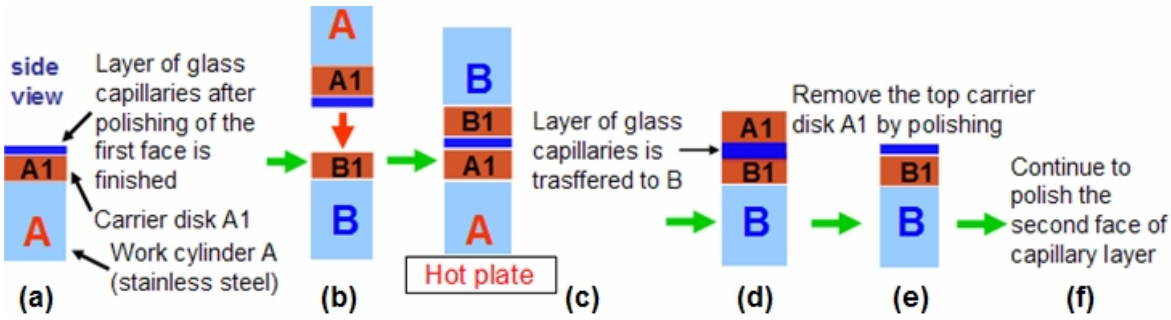

Fig 31: Fabrication steps for transferring the glass capillary layer from work cylinder A to B. (a – f) show different steps of transferring capillary layer.

After the polishing work on the first face of the glass capillaries is finished, we heat up a relatively high-melting-point wax to a temperature of 125 ℃ and pour it on the top to cover the area of glass capillaries (the melted wax covering capillaries is yellow area in Fig 30). This thin layer of wax bar can protect the surface of the first face of glass capillaries (Fig 30). The glass capillaries stand normal to the top surface of the cylinder.

Then we continued to transfer the capillary layer to the second work cylinder for continuing to polish the second face of the capillaries (Fig 31a – Fig 31f). In Fig 31b we used epoxy to fix work cylinders A and B together. When the epoxy between carrier disk B1 and glass capillary layer(deep blue layer) was dry and solid a few hours later, we put the whole body on a hot plate with cylinder A touching the hot plate in order to let the wax melt which was located between work cylinder A and carrier disk A1 (Fig 31c).

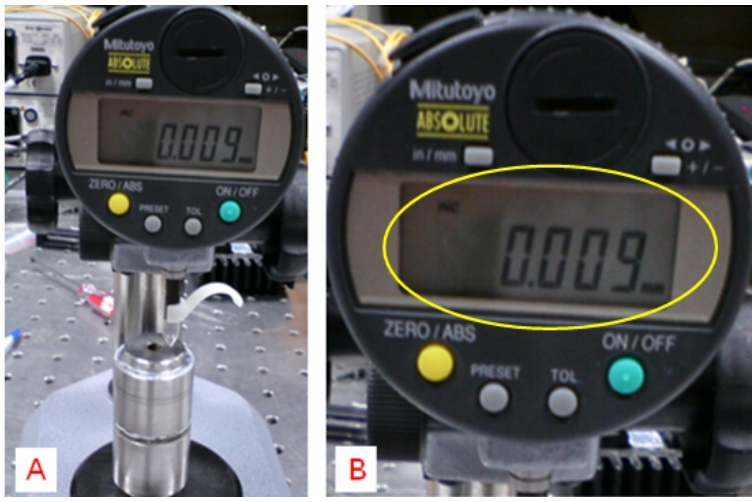

Fig 32: (A) and (B) Photos of height gauge stand with digimatic indicator. The brand is Mitutoyo, a Japanese company that specializes in precision apparatus. The model of digimatic indicator is 543-255B of Mitutoyo. The resolution of this model is 1 µm and the accuracy is 3µm according to its specification. In (B) 0.009 mm is clearly seen.

Once it was melted, we removed the upper portion gently and then the capillary layer was transferred to work cylinder B (Fig 31d). In Fig 31d the carrier disk A1 was removed by polishing (Fig 31e). The remaining thickness of the glass capillary layer can be obtained by using a height gauge stand with digimatic indicator

(9) Take out the glass microresonator using specific facility we made

After the polishing work was finished, we removed the micro-resonators by using the system shown in Fig 33. We fixed the work cylinder firmly on the facility in Fig 33.

We used a metal probe to position the specific device precisely under microscope. Then, we rotated the whole facility upside down for taking out the glass device easily (Fig 34). In the meantime, the microscope next to the facility was also rotated for following the position of glass device and the angle of the take-out facility (Fig 34). We removed individual device we selected by adding a tiny drop of acetone to dissolve the wax (Fig 34).

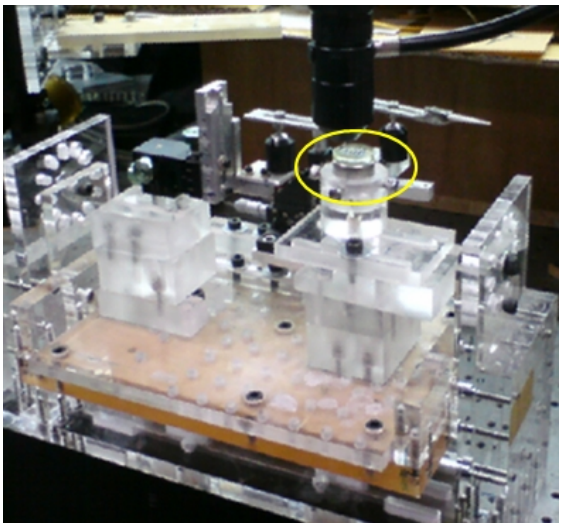

Fig 33: Photo of take-out facility we designed and made. Every glass microresonator will be removed from the top of work cylinder with the help of this take-out facility.

A sharp-end white flat bar was moved close to the metal probe on which the tiny glass microresonator already hang. This move could keep the tiny glass device from being off the hook of a metal probe. Then the whole facility was rotated back to the original position (Fig 33). Now the tiny glass device was already precisely taken out and transferred to the metal probe and constrained by a sharp-end white flat bar (Fig 35).

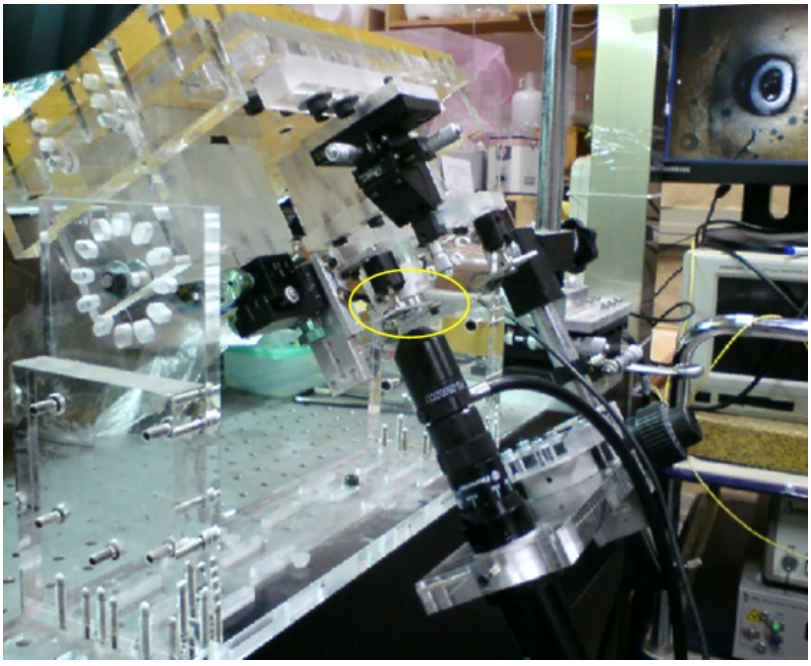

Fig 34: Take-out facility is upside down and ready for the step of removing a device from the top of work cylinder with microscope to monitor the process of taking out device smoothly. After one tiny drop of acetone is added to dissolve the thin-layered wax encapsulating the sidewall and bottom face of glass microresonator,

In Fig 35, the work cylinder will be removed from the facility and the transmission spectrum measurement will be the next step which will be also conducted on this facility because the tiny glass device was on the hook of a metal probe sitting on this facility. It is convenient for us to continue to do the next measurements of transmission spectrum

without moving tiny glass microresonator to other platforms. This whole facility has many functions integrated on it.

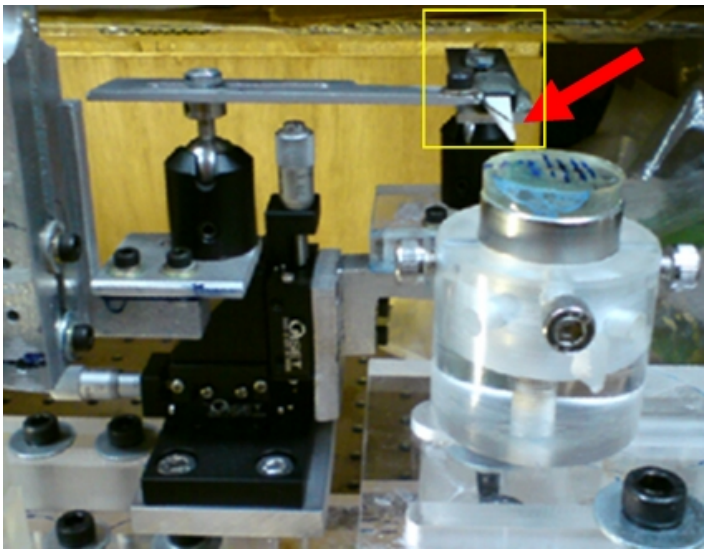

Fig 35: After the tiny glass microresonator is taken out, the whole take-out facility is rotated back to the normal position ready for the next step of

5.4 Some photos of glass microresonators under microscope

In the photos of Fig 36, a thin layer of wax which is generally only few micrometers is around the sidewall surface and some wax also in the hollow area of each glass microresonator. On the bottom face of glass microresonator a thin layer of wax also wraps the bottom face of glass device. Actually this step of wax wrapping the bottom face of each device was done in Fig 30. After the step in Fig 30, we transferred glass capillary layer to another work cylinder by flipping the original whole work cylinder. Then, we continued to polish another face of capillary layer. In the photos of Fig 36, all the glass microresonators are still embedded. Top surfaces of glass microresonators are cleaned by ultra-sonic cleaner and air-blowing.

From the 12 photos of (Fig 36), the glass microresonators look shinning like mirror under microscope of 380x magnification after being polished by suspension slurry of colloidal silica 70 nm.

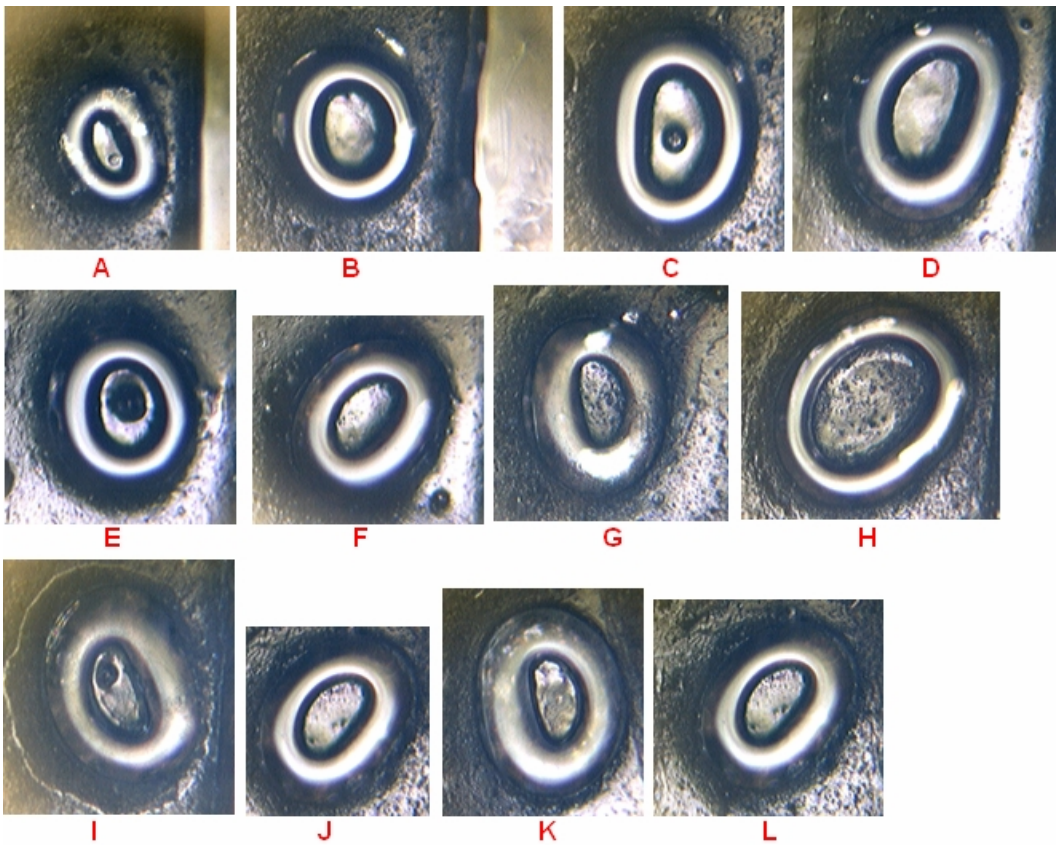

Fig 36: Microscope photos of 12 different glass microresonators to show their shining surface after being polished by suspension slurry of 70 nm colloidal silica. The magnification of microscope is fixed at 380X. The sizes of these glass devices are within 250 µm. These devices are still embedded. They were cleaned first in ultra-sonic cleaner and their top surfaces were also cleaned by air-blowing.

The surface uniformity of both faces of glass devices should be excellent because the size of small spheres of colloidal silica in suspension slurry is only 70 nm and in the meantime the chemical polishing process of suspension slurry also help improving the

surface uniformity of sample surfaces. We do not have apparatus to measure the surface uniformity of our devices, but further measurements that are beyond our current capability are needed for final verification.

This suspension slurry is widely used by semiconductor manufacturing companies to polish their large wafers for surface uniformity. Their wafer sizes are mostly 8 inch to 12 inch. Our glass microresonators have size of 20 ~ 250 μ m and are mounted on top of work cylinders whose diameter is only 25 mm only. Work cylinder of diameter 25 mm is extremely smaller than 8 inch wafer. This means that it is much easier to achieve surface uniformity for tiny glass microresonators mounted on work cylinder than that for 8 inch wafer.

The relevant literature also shows the flatness measurements for suspension slurry of colloidal silica of different diameters and different PH values, and so forth [59].

5.4 Measurement of the transmission spectrum

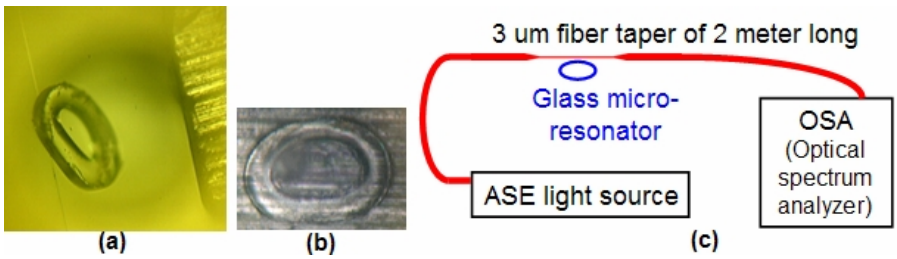

Fig 37: (a) A tiny glass microresonator can be supported by fiber taper with glue between them. (b) Another device we used for the measurement of transmission spectrum. This device is different from that in (a). For (a) and (b), it was seen by microscope of 380X. (c) Experimental setup for the measurement of transmission spectrum. The sizes of device (b) are shown in the following.

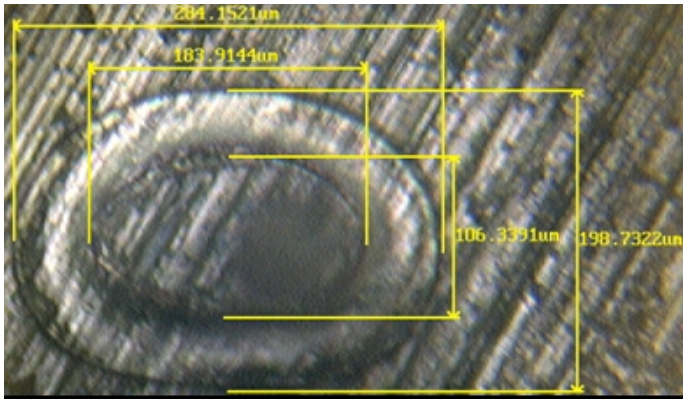

Fig 38: The sizes of glass microresonator we used for transmission spectrum are shown in this figure.

We did not have the equipment available to carry out a detailed study of the resonance characteristics of our fabricated glass microring resonators. However, we were able to directly measure the free spectral range (FSR) of our resonators using the setup shown in Fig 37c.

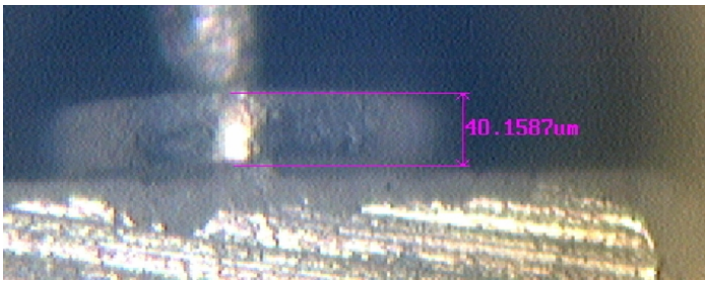

Fig 39: The thickness of glass microresonator is measured by microscope (380X) and about 40 μm.

In Fig 37a we moved a glass micro-resonator close to a fiber taper, also shown in Fig 37c, for the coupling process where a thin layer of glue had already been placed on the left outer facet of each micro-resonator. The uniform section of fiber taper of 3 μm diameter is 10 mm long and the total length of the taper is around 2 meter. It was made

from single mode fiber (SMF-28). In Fig 37a, a tiny glass micro-resonator was shown attached to a 3 μm taper and hung in air. The tiny micro-resonator is extremely light such that this 3 μm taper can support it.

Fig 37b shows another device. This was fabricated in a racetrack shape. Its thickness is 40 μm and perimeter is 780 μm. Fig 37c is the experimental setup for measuring the resonance spectrum. One end of a 3μm-diameter taper of 2-meter long was connected to an amplified spontaneous emission (ASE) light source and another end connected to an optical spectrum analyzer (OSA). While coupling the glass micro-resonator to the fiber taper, index matching liquid of refractive index 1.4520 was applied between them for improved index matching. Fig 40 is the normalized spectrum of the device in Fig 37b. The FSR of this device is 0.22 nm and the half transmission dip width is 0.095 nm. Although this data suggests that the finesse is 2.3 and quality factor Q is 16,117, this grossly underestimates the likely very high finesse of our microrings. The coupling between the fiber taper and the microring is too large when there is index matching fluid in the interface, which drastically reduces the apparent finesse. In order to get a measure of the true finesse the microring resonators must be very lightly coupled to the microring. In the experimental arrangement shown in Fig34c, light from the ring couples very efficiently back into the probing fiber. We attempted to measure the resonance spectrum with an air gap between fiber and microroing, but were unsuccessful. In this case, without the thin layer of index matching fluid there is virtually no coupling between fiber and microring. Its finesse is 2.3 and quality factor Q is 16,117. The loss, 1.8~2.5 dB below zero, in the spectrum of Fig 37b is due to the loss caused by the liquid applied between device and taper.

However, our ability to measure the true finesse is affected by the improper coupling to the microring and our lack of measurement capabilities. We believe that with further improvement of the fabrication technique much better performing devices are possible. The fundamental smoothness of our microrings is very good, but our technique for coupling to the microring needs to be improved.

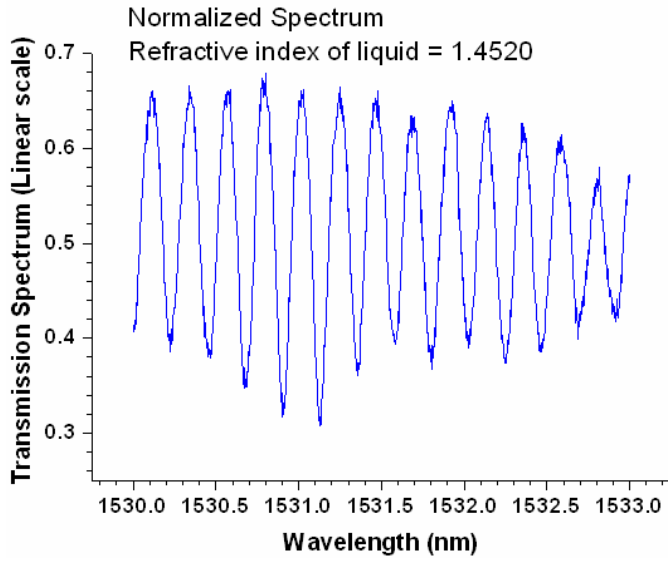

Fig 40: Normalized transmission spectrum in linear scale. The refractive index of the index-matching liquid we used for this measurement is 1.4520.

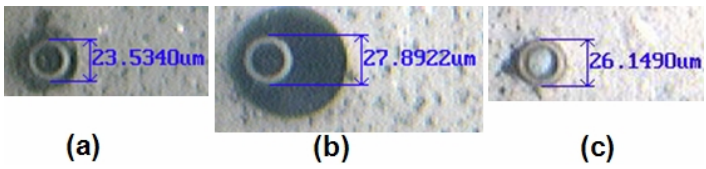

Fig 41: (a) (b) (c) Glass microresonators of smaller diameter we can fabricate.

Fig 41(a, b, c) show the smaller microresonators we made. The smallest one is 23.5 μm in diameter. By polishing further, the device thickness can be reduced to 10 μm which is better for coupling due to the mode matching condition between fiber taper and

glass microresonator. The spectrum of the device with thickness of 10 μm would be better than that in Fig 40. According to our experimental results in the past, the transmission dip can be larger than 10 dB for a device of 10 μm thickness. As discussed in the above, the finesse would be larger for the glass microresonators of 10 μm thickness and smaller perimeter (≦100 μm). As for the applications of our device, the medium surrounding the glass microresonator is air. Therefore, it can work as a chemical, gas, or liquid sensor. Moreover, we saw some disturbance or spikes in the spectrum when we deliberately disturbed the optical table on which the device was placed. This device can also work as a vibration sensor if soft glue of appropriate refractive index can be applied between device and fiber taper.

5.5 Discussion and advantages of this new method

The purpose of inventing this new method was to check the possibility of improving the fabrications of semiconductor and polymer microresonators. We did not seek devices of higher finesse and quality factor due to funding shortages. In the meantime, we have designed and made a complete set of facilities especially for this new method. We will discuss and show the designs and functions of each facility of this new system in the following chapters (6 -- 14). Here we summarize the advantages of our new method as follows.

5.5.1 Low cost, good surface quality, high yield

The fabrication of this highly polished resonator only needs a polishing machine and mechanical systems. In comparison with semiconductor techniques it is low cost. Because our glass capillaries were made by a puller at temperature (≧1000℃), the

surface quality of each one is almost smooth naturally and excellent. But we still need apparatus to measure its surface roughness in the future for verification. The yield rate of this polishing method is above 50%. It could be above 90% if some critical steps are optimized in the future. The critical step was cutting each array of glass capillary before they were glued on the initial acrylic substrate. If they could be cut with a high power laser this would provide an even higher yield. We used a diamond knife to cut the capillaries. This caused damage on the end facets of some glass capillaries, which can be removed and remedied by a polishing process.

5.5.2 Fast fabrication, large quantity

For the total time this method took, it was about 6 weeks and there are few critical steps which took much time. The first critical step is the material of the strips (Fig 25c, Fig 26b, Fig 26c). If it can be replaced by another plastic material that is softer than acrylic strip, the polishing would be quite fast and the total time would be much shorter. The second critical step is the polishing slurry of the final step. We recycled slurry by adding a little new one to the old one for keeping its pH value. The old slurry was collected from the polishing machine. Using new slurry would save much time for polishing. We estimate that the total time could be less than 2 weeks if the above two critical steps can be optimized in the future. In comparison with semiconductor microresonator processing, our new method is quite fast. For each batch our facility can process 800 ~ 1200 glass capillaries at the same time. It can be more than 1200 capillaries if the acrylic strip design in (Fig 25c, Fig 26a, Fig 26b, Fig 30) is replaced with a design of denser pattern.

5.6 Comparison between glass microresonators we made and resonators made by other methods in recent years

Firstly, although our microring resonators are low cost and mass producible, their apparent quality factors are much lower than devices made by other means in recent years, which can be as high as ~ $1.6x10^4$. The finesse ~2.3 of our device is much lower. One of the reasons is that our glass resonators are quite large (~ 780 μm perimeter) which significantly reduces the finesse. The measured finesse may also be lowered because the coupling condition of our glass microresonator is not close to the critical coupling condition. The finesse and quality factor of our devices still need to be improved in the future by using smaller glass resonators and improving coupling conditions. The quality factors of microresonators made by other techniques in recent years are as follows. For example, in 2015 the SOI microring [60] of butterfly-coupled design has quality factor of ~$1.0x10^5$. In 2011 the SOI microring made by Lei Jin [61] has quality factor of ~ $2.0x10^4$. In 2015 SOI micro-rings based on sub-wavelength grating waveguides [62] have quality factor of 1000 ~ 6000. The SOI microrings [63] for biochemical sensing reported in 2014 have quality factor of the order of 10^5. In 2014 the silica microsphere, MgF_2 disk and fiber ring resonators [64] have Q-factor as high as $Q=10^{10}$. In 2015 the low cost SU8 polymer microring [65] has their best result of Q= $1.5x10^4$. But in this paper they did not indicate their yield rate and total number of devices per batch they processed. In 2011 the high-Q polymer micro-ring [66] using nano-imprint technique shows Q = 10^5. In 2013 the high-Q factor silicon-on-sapphire ring [67] is $1.5x10^5$. In 2012 the ultrahigh-Q wedge-resonator made by Hansuek Lee [68] has Q= $8.7x10^8$. In 2014 the lithium niobate

microdisk made by Cheng Wang [69] has Q ~ 10^5. In 2013 the microresonator using femtosecond laser micromachining made by Kazunari Tada [70] has Q ~ $7.2x10^6$.

Secondly, as for the yield rate, total number of processed devices, and total processing time of microresonators per batch, most literature does not mention clearly. But one paper [70] showed some data about this. The devices made by femtosecond laser micromachining also have good surface quality although they did not show surface roughness data. They used non-thermal laser ablation and heat reflow process on 125 μm fused silica fiber. The quality factor of their microdisk is $7.2x10^6$. This is much better than that of our glass microresonators. Their whole process can be finished in twenty minutes. At this speed of processing, the total number of their microdisks could be about 1000 within six weeks, which is the time taken by our highly polished method per batch. But on their paper they did not indicate the yield rate of microdisks in processing. In the meantime, according to our discussion on the previous pages our processing time could be within two weeks if the material of strip fixed on work cylinder is replaced with a softer one. And our yield rate is above 50%. Compared with this method of femtosecond laser micromachining the quality factor of our glass devices is much worse. The quality factor of our glass microresonators need to be improved further. The refractive index and loss of glue should be replaced with an appropriate one for better coupling conditions. The method of femtosecond laser micromachining has much potential in the future, but requires very expensive equipment. They also need to find a way to precisely control the diameter of each microdisk.

Thirdly, as for the surface quality of devices our glass microresonator has a surface naturally formed on melting and drawing at high temperature ≧1000℃. Its surface

quality should be excellent but it still needs verification by using apparatus to measure surface roughness in the future. As for the papers on other method, the waveguide made by multiphoton absorption polymerization (MAP) [71] has very smooth walls. Their SEM photos have a resolution better than 100 nm. It should be quite close to the sidewall surface quality of our glass devices where our capillary forms a naturally smooth surface on melting and drawing at high temperature ≧1000℃. According to other relevant literature on MAP [72, 73], some steps of their MAP method are pretty time consuming, a few days or even a few weeks. And the authors did not indicate the yield rate, so we can not make comparison between different techniques.

Advantages of glass resonators are discussed in the following.

By this new method glass microresonators can be fabricated at low cost and in fast mass production. As discussed earlier, the fabrication time is within six weeks. If some critical steps can be optimized in the future, the fabrication time could be shortened to less than two weeks. The surface uniformity of both faces of glass devices should be excellent because the size of small spheres of colloidal silica in suspension slurry is only 70 nm and in the meantime the chemical polishing process of suspension slurry also help improve the surface uniformity of sample surfaces. According to the literature [59], most samples polished by a suspension slurry of colloidal silica of different diameters show surface roughness which is generally within a few tens nano-meters except in a few cases of high material removal rate with large size colloidal silica, high oxidizer contents and low lubricant content. Literature values show surface roughness with respect to different PH values, weight percentages and diameters of colloidal silica, volume percentages of oxidizer, and so on. As for the sidewall surface quality also should be excellent because

glass capillary forms a naturally smooth surface on melting and drawing at high temperature ≧1000℃. We do not have apparatus to measure the surface uniformity of our devices, but in the future further measurements are required for verification. The yield rate, percentage of devices w/o cracks on edge, of our glass resonators is above 50%. We estimate that this yield rate can be higher than 90% if a high power laser beam can be used to cut the capillaries for better end facet quality of capillaries which are fixed on strips.

5.7 Conclusion

Based on the prior experience of doing experiments on semiconductor microresonators as well as fabricating semiconductor microresonators in a clean room which is described in the first part of this dissertation, we had realized that the current semiconductor fabrications of micro-resonator have many disadvantages, which it has been difficult to overcome over the past decades. Thus, we come up with an innovative method to fabricate glass microresonators. It opens a new path for microresonator fabrications at low cost, in fast mass production, with excellent surface quality (need apparatus to measure it for verification), and with high yield rate. There is no existing system specific for glass microresonator from industry. We designed and made a complete set of facilities specific for this method to work properly. We list them in Appendices.

Nobody else has tried to fabricate microrings by a cutting and polishing technique. Our new method can also apply to other materials such as lithium niobate which has been widely used in many photonic applications due to its excellent electrooptic, acoustooptic, piezoelectric, and nonlinear-optic properties. According to the literature [74], it is

difficult to obtain good surface quality after dry etching. Dry etch is a challenging work for lithium niobate microring and usually results in rough sidewalls of microring. It produces large scattering losses and causes fairly low optical quality Q factors (4,000 in [75], 2007).

According to the book [76], the hardness of $LiNbO_3$ has a value of 5 on the Mohs scale. In general glass has a value of range 4.8 ~ 6.5 on the Mohs scale of hardness (see Mohs hardness scale listed on page 104). So, lithium niobate is softer than generic glass and it would be easier to polish lithium niobate with our method. If a lithium niobate microresonator needs to be integrated with other semiconductor bus waveguides, a micro-manipulator system has to be used for performing the alignment of lithium niobate microresonator with semiconductor bus waveguide.

This glass microresonator can work as gas sensor, chemical sensor, liquid sensor, and vibration sensor. This provides an alternative method for fabrication of glass micro-resonators avoiding more costly semiconductor techniques. The advantages of this new method are low-cost, high-yield, good surface quality of sidewall, large quantity, and fast fabrication.

Chapter 6: Conclusion

6.1 Accomplishment and innovation

Over the past several years our group at the University of Maryland had focused on single photonic logic gate operations using single microring resonator [28, 29, 31] (see publications listed in section 6.3). I was a contributor to some of these experiments. The first part of this dissertation furthers this work by demonstrating cascaded photonic AND logic gates by using two symmetric semiconductor GaAs microring resonators. This achievement is important for other operations of cascade photonic logic gates by using multiple micro-resonators in the near future. The paper of Dr. Brent Little [1], "Towards very large-scale integrated photonics", foresees the future trend of all-photonic integrated circuits that will contain a tremendous number of photonic logic gates comprising multiple micro-resonators to do multiple-stage logic gate operations. Because of this, our experiment is the building block of multiple-stage logic gate operations.

The second part of this dissertation describes the development of an innovative method for fabricating highly polished glass micro-resonators. No existing polishing systems specific for glass micro-resonator fabrication are available from industry. To accomplish this, we designed and made a complete set of facilities specific for this unique polishing method to work properly. This method has several advantages such as low cost, high yield ($\geqq$50%) (percentages of devices w/o cracks on edge), fast fabrication ($\leqq$6 weeks), and large production quantity (800 ~1200 per batch). The surface quality of glass resonators should be excellent because capillaries were made at high temperature $\geqq$1000℃ and devices were polished by suspension slurry of 70 nm

colloidal silica. Further measurements that are beyond our current capability are needed for final verification. It opens up a new path for developing micro-resonators of low cost and high surface quality sidewalls with a fast fabrication method.

6.2 Suggestions for future work

As for the future research on different cascade photonic logic gates using multiple microrings, combinations of different logic gates can be studied. Besides, the material of our semiconductor GaAs microrings can also be replaced with other more optically nonlinear materials, such as quantum wells inserted in the microring core region. This can lower the power consumption of cascade photonic logic gates by microrings and improve their performance.

As for the future research on the highly polished glass microresonator, some suggestions are as follows.

[1] The glass micro-resonators can work as gas sensor, chemical sensor, solution sensor, and vibration sensor. Advanced designs can be studied in the future for better sensing sensitivity with such glass micro-resonator.

[2] Combine glass microresonators with other fiber devices for different applications. It also can be integrated with other semiconductor chips through mode converters on chips to couple light beams in and out.

[3] To design a power laser beam system to cut the glass capillaries that are fixed on the edge facet of each acrylic strip. Such a system must be combined with the gluing facility (Fig 25a, Fig 25b) in order to cut capillaries smoothly. This will reduce the probability of damage to the edge facet of glass capillaries during the cutting process and

increase the yield rate of final glass microresonators. We estimate that the final yield rate could be higher (≧ 90%) if this optimization could be achieved in the future.

[4] Firstly, to replace the acrylic strip (in Fig 25c and Fig 26a) with a softer material. This will speed up the polishing process dramatically and save a lot of processing time. Secondly, to add some chemicals or solutions in the polishing slurry in order to increase the polishing rate. This also can reduce the process time. We estimate that the overall process time could be much shorter (≦ 2 weeks).

[5] Design a micro-manipulation system specific for picking out the smaller glass microresonators and more precisely conducting experiments of different glass microresonator functions.

6.3 Publications

All the publications are listed below on the next two pages.

At the beginning I had worked on InGaAsP microring fabrications with Dr. Rohit Grover for a few years. At the same time I had worked on GaAs microring fabrications with Dr. Tarek Ibrahim for many years prior to doing the experiments on cascaded photonic AND logic gates using two symmetric GaAs microrings. I had contributed to some portions of his fabrications in clean room and also some portions of his experiments of different single logic gates using microrings. After finishing the experiments on cascaded photonic AND logic gates I had worked on the fabrication of InGaAsP microring lasers with Dr. Kuldeep Amarnath in the clean room for two years. I contributed to some portions of his fabrications in the clean room and some portions of his experiments on amplification and lasing in microrings.

1. Li-Chiang Kuo, V. Van, K. Amarnath, T. N. Ding, W. Astar, G. M. Carter, and P.-T. Ho, “Cascaded Integrated Photonic AND Gates Based on GaAs Ring Resonators,” in the *Proceedings* of *Conference on Lasers and Electro-Optics (CLEO),* 2006, Paper CMJ2.

2. T. A. Ibrahim, R. Grover, L.-C. Kuo, S. Kanakaraju, L. C. Calhoun, and P.-T. Ho, "Photonic AND/NAND logic gates using semiconductor microresonators," *IEEE Lasers and Electro-Optics Society (LEOS)* 2003

3. R. Grover, T. A. Ibrahim, T. N. Ding, L.-C. Kuo, S. Kanakaraju, L. C. Calhoun, P.-T. Ho, "Ultracompact single-mode GaInAsP-InP microracetrack resonators," *Integrated Photonics Research, Silicon and Nano Photonics (IPR)* 2003

4. T. A. Ibrahim, R. Grover, L.-C. Kuo, S. Kanakaraju, L. C. Calhoun, and P.-T. Ho, "All-optical switching in GaInAsP-InP microresonators," *Integrated Photonics Research, Silicon and Nano Photonics (IPR)* 2003

5. T. A. Ibrahim, R. Grover, L.-C. Kuo, S. Kanakaraju, L. C. Calhoun, and P.-T. Ho, "All-optical AND/NAND logic gates using semiconductor microresonators," *IEEE Photonics Technology Letters (PTL)*, vol. 15, pp. 1422-1424, 2003

6. R. Grover, T. A. Ibrahim, T. N. Ding, Y. Leng, L.-C. Kuo, S. Kanakaraju, K. Amarnath, L. C. Calhoun, P.-T. Ho, "Laterally coupled InP-based single-mode microracetrack notch filter," *IEEE Photonics Technology Letters (PTL)*, vol. 15, pp. 1082-1084, 2003

7. T. A. Ibrahim, K. Amarnath, L.-C. Kuo, R. Grover, Vien Van, P.-T. Ho, “Photonic logic NOR gate based on two symmetric microring resonators “ *Optics Letters*, vol29, 23, p2779-2781, Dec. 2004

Appendix 1: Buildup of puller, glue-on facility, work cylinder, and sample substrate plates specific for glass microresonator

In the following **Appendix** chapters we will show designs and fabrications of facilities specific for our highly polished glass microresonator that was discussed in chapter 5. We have contacted some manufacturers for existing polishing system specific for our glass micro-resonator. No existing system specific for our glass microresonator has been found. So we have designed and built a whole set of facilities specific for glass micro-resonator. Here at first we discuss the extra-long-range puller of glass capillary we designed and made.

A1.1 Extra-long-range puller of glass capillary

A1.1.1 Commercial short-range puller of glass capillary used initially

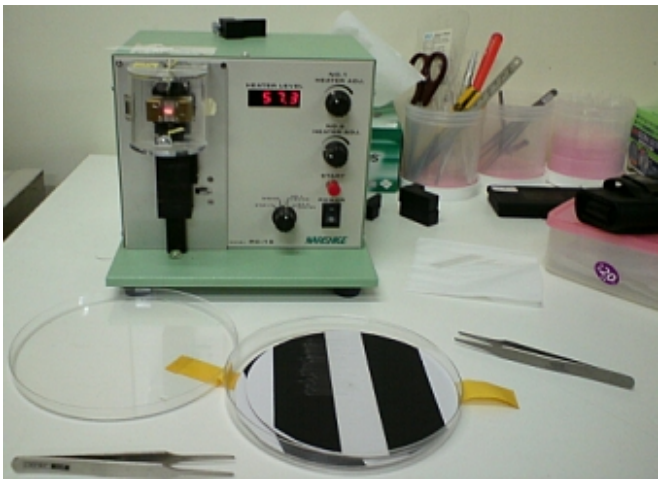

Fig 42: A small glass needle puller we initially used for our glass capillaries. Its drawing range is short and only 2 – 4 centimeter.

Fig 42 shows a commercial short-range puller of glass capillary I had used initially, which was located in another building. It has a controllable heat source.

A1.1.2 Motivation for designing and making the extra-long-range puller

The pulling range is too short to meet the requirement of glass micro-resonator experiments. There is no available existing ultra-long range puller from industry. A new puller specific for glass capillary was designed, fabricated, and built.

A1.1.3 Original designs and photos of the final structures

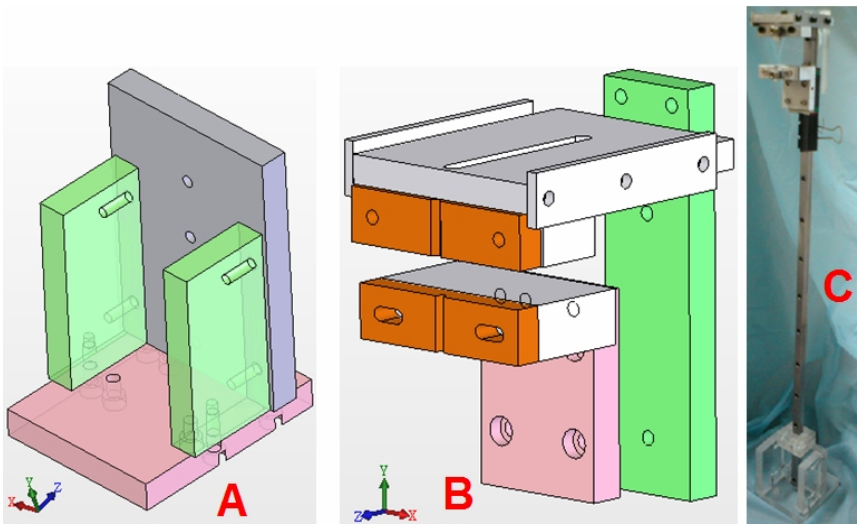

Fig 43: 3D plot of ultra-long puller we designed and made.

Fig 43a and Fig 43b show the lower and upper portions of the original design, respectively. Fig 43c shows the final structure of this long range puller of glass capillary.

Fig 44b, Fig 44c, and Fig 44d are upper portion viewed from different direction. Fig 44e is front view of upper portion. Fig 44f is rear view of upper portion. This upper portion is made of aluminum because high temperature of torch may deform the body of

puller. The vertical free fall rail in Fig 44a is made of stainless steel which is about 75 cm long. Fig 45a is lower portion. Fig 45b is rear view of lower part and Fig 45c is bottom view of it.

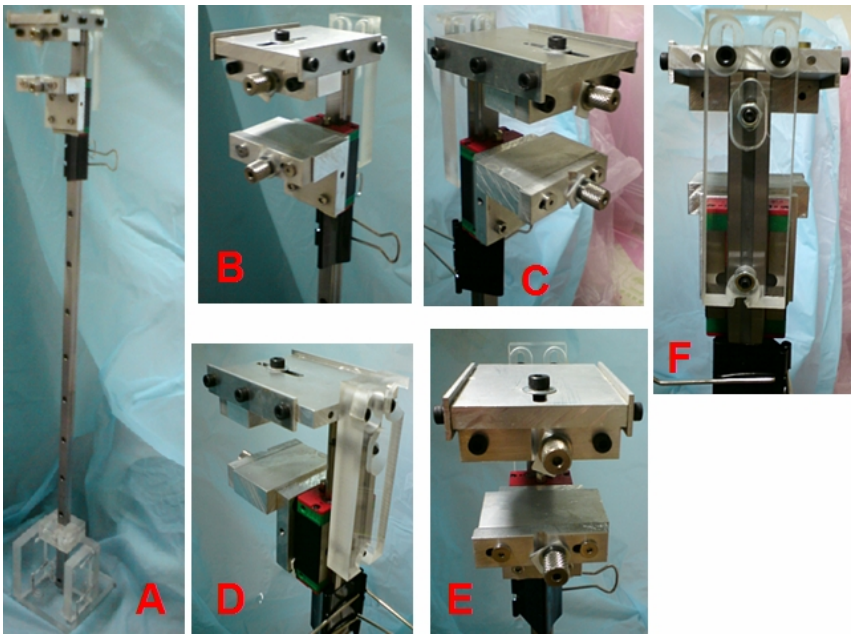

Fig 44: Photos show different view angles of whole ultra-long puller and its upper part.

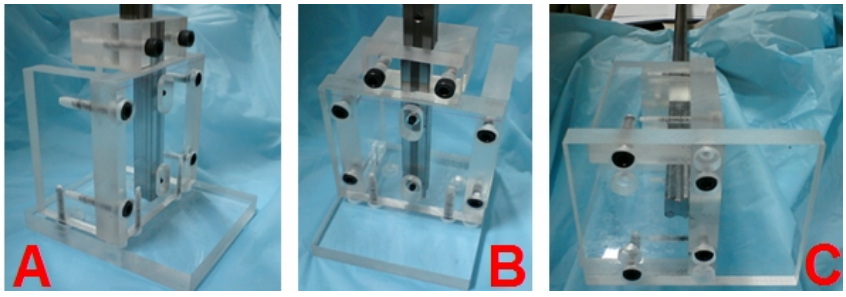

Fig 45: Photos of lower part of ultra-long puller.

A1.1.4 Engineering drawings of selected components

Because there are many components in this design of an extra-long-range puller, only two engineering plots of components are shown. Most components of this puller

were made by me in a machine shop. The engineering drawing in Fig 46a is the transparent acrylic vertical plate attached to the vertical stainless steel rail in Fig 44c and Fig 44f. Fig 46b is the engineering drawing of the top alumina horizontal plate shown in Fig 44b and Fig 44c.

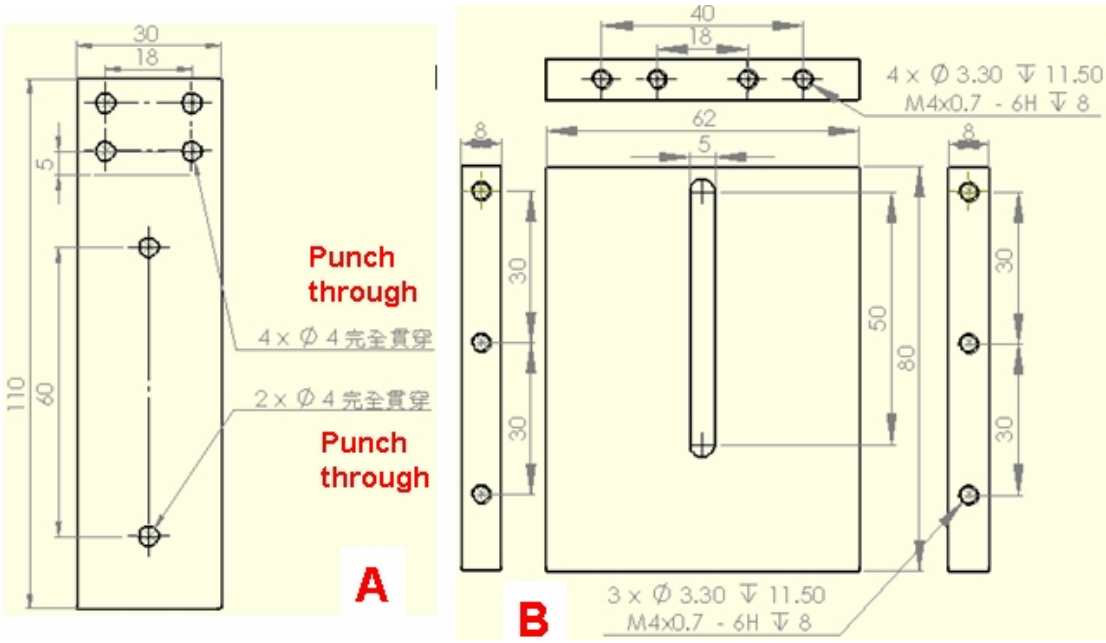

Fig 46: Engineering drawings for the back plate of the lower portion to fix and firmly grab the stainless steel rail.

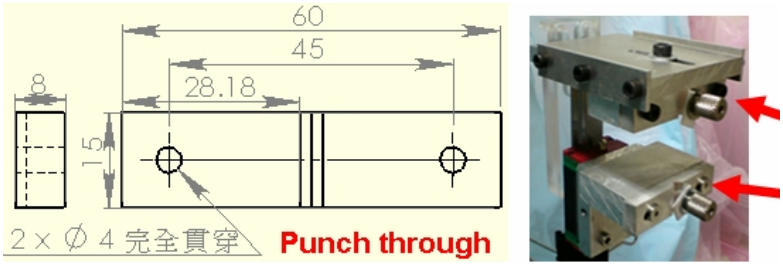

Fig 47: Engineering drawing for the upper part of ultra-long puller and photo of the upper part.

Fig 47 is the engineering drawing of the rectangular plates, which have V-groove in the edge center, attached to the top plate and the rectangular block sitting on the sliding block of the stainless steel rail.

Fig 48 is the engineering drawing of the back plate of the lower portion to fix and firmly grab the stainless steel rail. In the final chapter, the experimental processes will be discussed.

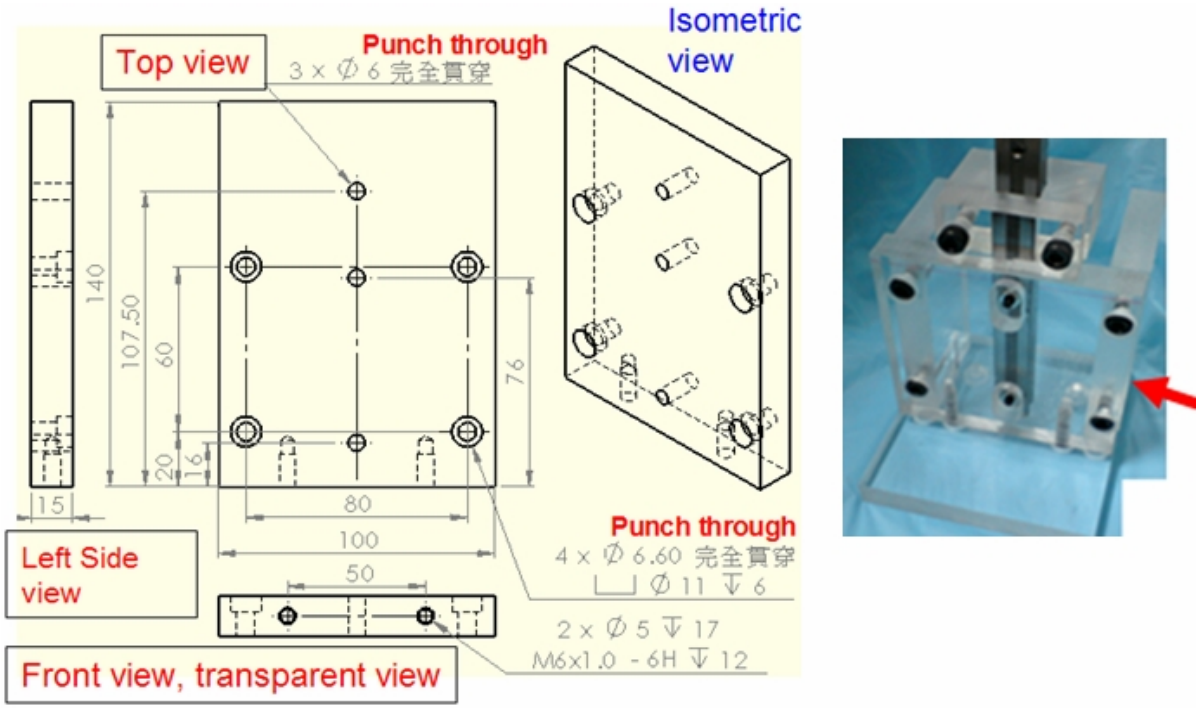

Fig 48: Engineering drawings for the lower part of ultra-long puller and photo of the lower part.

A1.1.5 Discussion about this facility

After this extra-long-range puller was finished, to pull glass capillaries become more convenient and faster. Each time we made one long uniform capillary using this extra-long puller. The uniform section is long enough such that we cut it into many short sections. This is good for the next few steps to go faster (see Fig 49 and Fig 50). The

original commercial small puller could only make very short uniform glass capillaries due to its short travel range for pulling glass tubes. So, this facility we made really solved our problems that were encountered in experiments.

A1.2 Glue-on facility

A1.2.1 Motivation for designing and making glue-on facility

After glass capillary is made by puller, a facility needs to be designed for gluing many arrays of glass capillaries, which are fixed on each glass plate one by one (Fig 49a and Fig 49b), on the edge facets of long strips simultaneously. This design can save a lot of time in the following steps of this new method for fabricating glass micro-resonators. The following sections show the evolution of designs of this glue-on facility. In Fig 49b many glass capillaries are fixed on one rectangular plate.

Many rectangular plates (Fig 50a) with glass capillaries on them are glued on the edge facets of each thin strip vertically clamped by glue-on facility (Fig 50b, which shows the optimized glue-on facility).

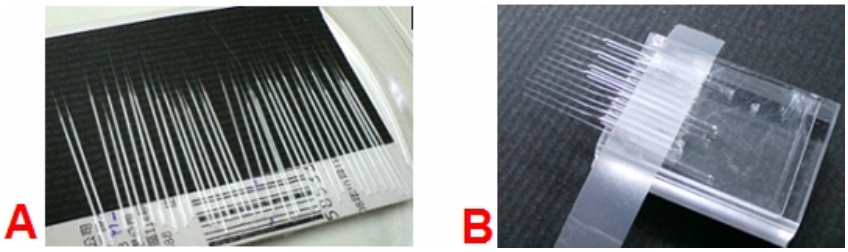

Fig 49: Glass capillaries attached on plate.

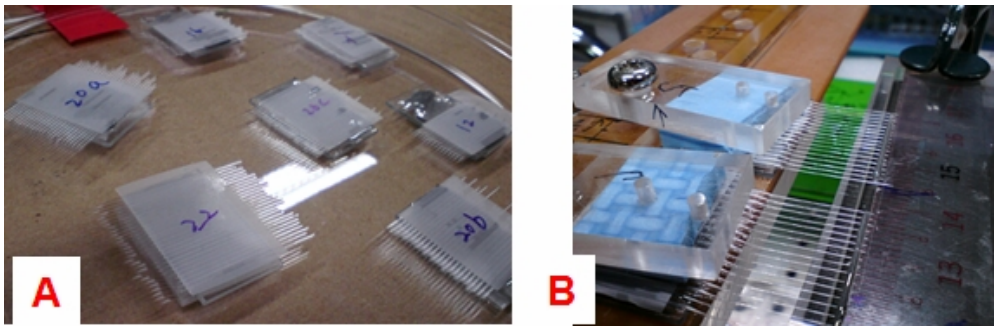

Fig 50: Glass capillary arrays stored in Petri dish. Two arrays of capillaries are fixed on the edge facets of acrylic strips.

A1.2.2 The glue-on facility

(1) **Original design plots**

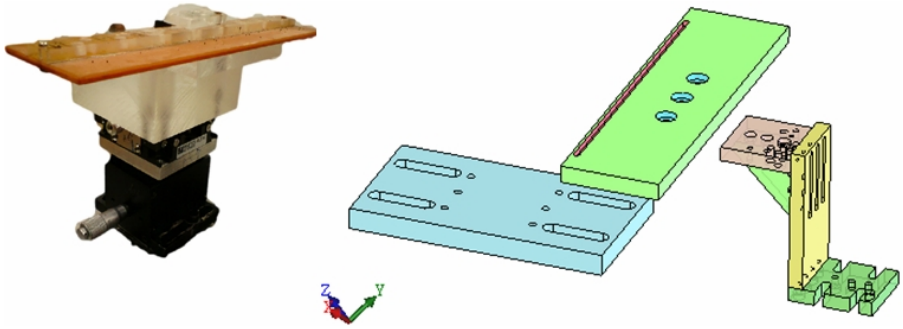

Fig 51: 3D plot for the glue-on facility we designed and made.

Fig 51 is a full view of the whole structure of the optimized glue-on facility. This system has functionality to fix every rectangular plate, which carries many capillaries, on clamping plate. The system can handle at most eight rectangular plates simultaneously and can fix every rectangular plate before glue is placed on the edge facets of strips. Real object of the glue-on facility is shown in Fig 52.

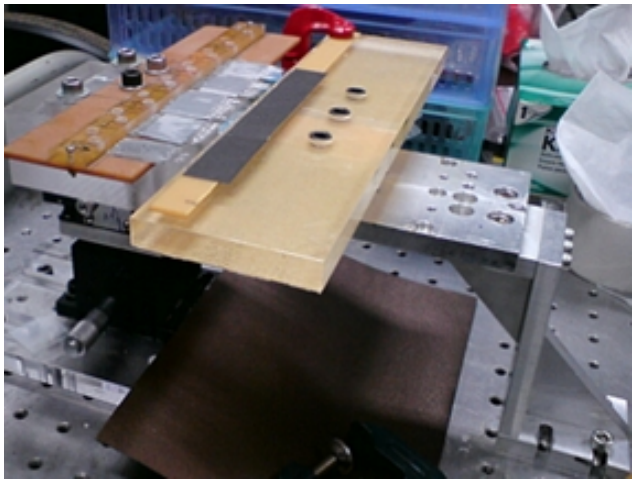

Fig 52: Photo of glue-on facility.

(2) **Engineering drawings of selected components**

Fig 53 is the drawing of the bottom plate in the left part of Fig 51. This bottom plate bears z-axis and x-axis stages on it.

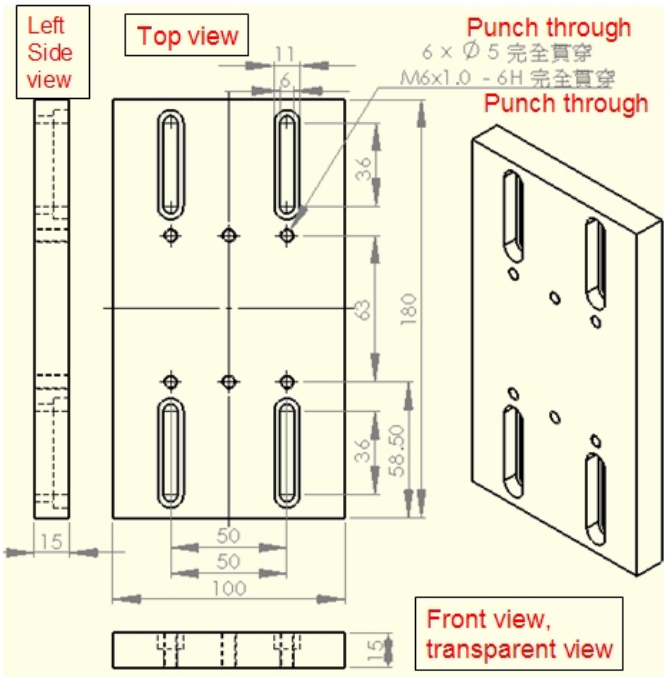

Fig 53: Engineering drawings for the bottom plate in the left part of Fig 51.

A1.3 Work cylinder

This work cylinder (Fig 54a) is designed to carry six or more strips glued on it (Fig 51) and each strip has 10 to 30 glass capillaries in arrays glued on its edge facet (Fig 54c). In total there would be 100 or more glass capillaries glued on one work cylinder. Each work piece fixture can support 4 to 6 work cylinders (Fig 55, Fig 56). So, for each batch 400 ~ 600 glass capillaries can be processed for polishing. The work cylinder will be inserted in the work piece fixture for polishing (Fig 55a, Fig 55b, and Fig 56). Different work piece fixtures will be described in the following chapters.

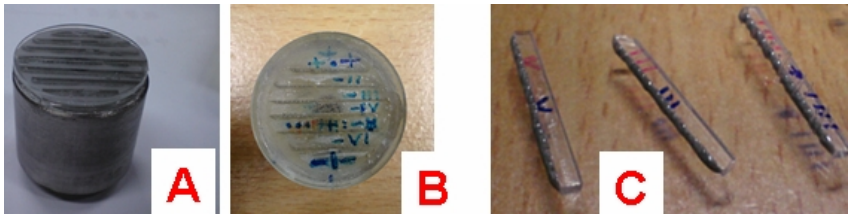

Fig 54: (A), (B) different views of work cylinder. (c) acrylic strips with capillaries fixed on the edge facet of strips.

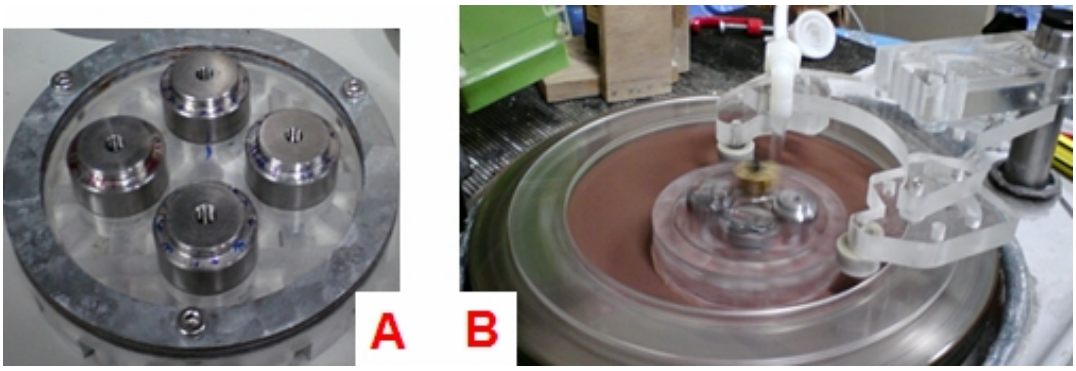

Fig 55: (A) small workpiece fixture (B) small workpiece fixture is operation.

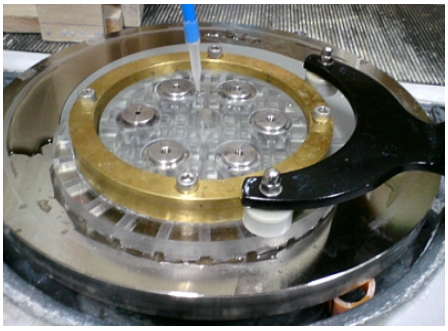

Fig 56: Large workpiece fixture.

A1.4 Sample substrate plate designs

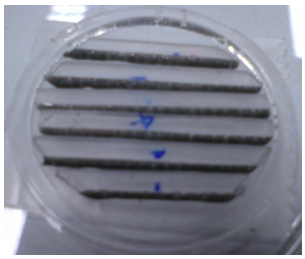

Fig 57: Layout of acrylic strips packed together.

One each top face of work cylinder there are 6 ~ 7 acrylic strips (Fig 57). Fig 58 shows the acrylic strips are fixed on top of work cylinder viewed from different angle.

Fig 58: Isometric view of work cylinder with six acrylic strips fixed on top of it..

Appendix 2: A complete set of facilities specific for the highly polished glass micro-resonators

A2.1 Motivation for designing facilities specific for glass microresonator

We have contacted a few facility manufacturers for available system specific for our glass micro-resonator. There was no existing system specific for our glass microresonator. So, there was a need for designing and making facilities specific for our polishing machine to fabricate highly polished glass micro-resonators.

A2.2 Design of acrylic cover for protecting circular polishing plate

A2.2.1 Original default polyurethane polishing plate

Fig 59: Polishing machine we used.

Originally the polishing machine had only one default polyurethane polishing plate which is expensive and only for polishing jobs. A new acrylic cover was designed in order to protect the surface of the polyurethane plate and to let the new cover serve as the plate for both lapping and polishing processes. For lapping jobs, the grit sizes of abrasive

disks are larger. For polishing jobs, the particle sizes in slurry are much smaller and in general are a few tens of nano-meters in size.

Fig 59 is the original default polyurethane plate sitting on the pedestal plate of stainless steel. A new acrylic cover was developed to protect the original polyurethane plate.

A2.2.2 Acrylic cover designed for default polyurethane plate

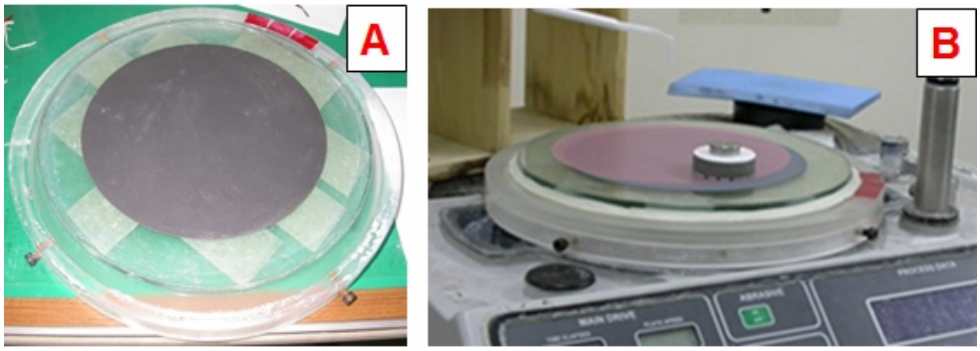

Fig 60: (A) Acrylic cover we designed. (B) Acrylic cover is used to protect the original polishing plate.

Fig 60a shows the acrylic cover designed for the polyurethane plate. There is one circular glass plate attached on the top of the acrylic cover. Fig 60b shows the newly designed acrylic cover sitting on the default polyurethane plate for protecting the surface of the default polyurethane plate.

A2.2.3 Original design of acrylic cover

(1) **3D design plot**

Fig 61a and Fig 61b are 3-D plots for the newly-designed acrylic protection cover for the polyurethane plate. Four screw holes on the outer edge surface will be made and

are used to fix the acrylic protection cover after this cover is put on the top of the machine (see Fig 60b).

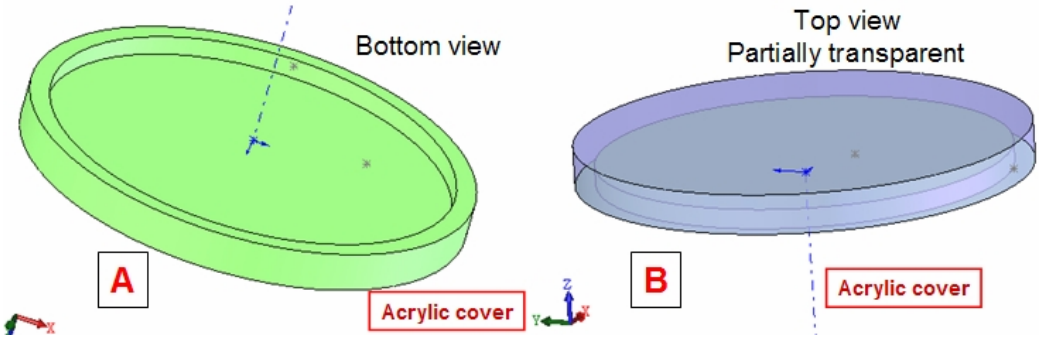

Fig 61: 3D plots of acrylic cover. (A) bottom view (B) top view.

(2) **Engineering drawing**

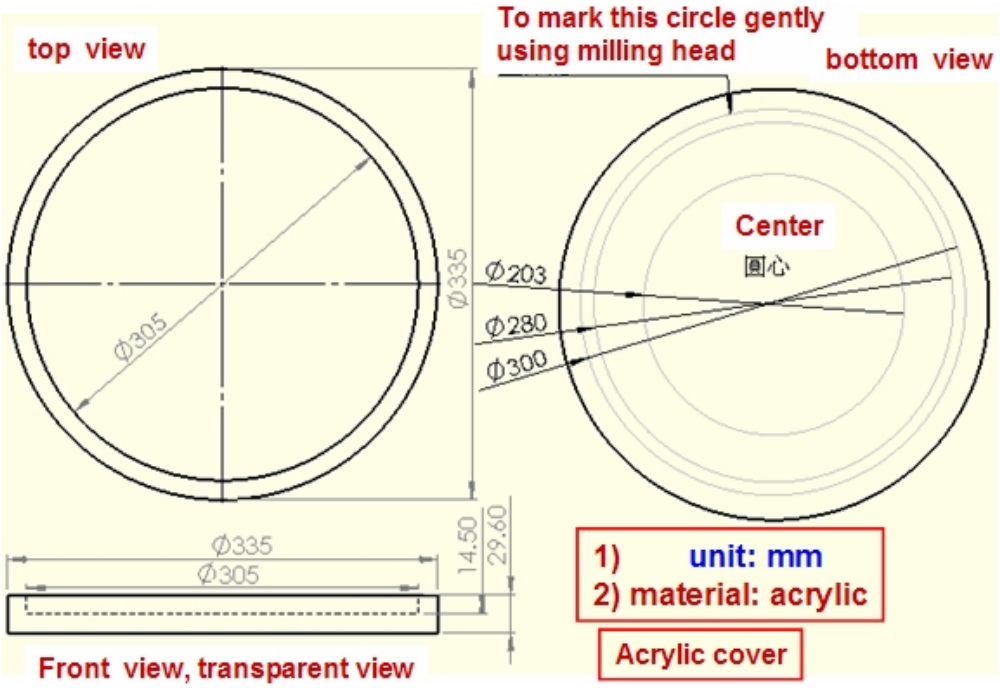

Fig 62: Engineering drawings for acrylic cover.

Fig 62 is the engineering drawing of the acrylic protection cover for the polyurethane plate. Its inner diameter is 305 mm to fit the size of the original polyurethane plate.

A2.3 Design of stainless steel lapping/polishing plates

A2.3.1 Motivation for designing new stainless steel plates for lapping/polishing processes

After the acrylic protection cover had been used for about one and half years, many problems occurred due to this protection cover. Many methods had been tried to solve those problems, but those problems could not be solved completely. Thus, a better way was to discard the previous protection cover and to replace the original default polyurethane plate with a new stainless steel plate designed for this polishing machine. Therefore, there was no need to touch the original default polyurethane plate which is not for polishing glass micro-resonators and is expensive. This stainless steel circular plates was used as a lapping and polishing plate. During lapping processes, coarse abrasive disks will be placed and fixed on the top of the stainless steel circular plate. During polishing processes, fine abrasive disks or polishing pad will be used.

A2.3.2 3D design plot

Fig 63 is the 3-D plot of stainless steel circular plate. Fig 64 is its engineering drawing. The diameter of this stainless steel plate is 303 mm as can be seen in its drawing. Its thickness is 19.20 mm. In Fig 65 there are three stainless steel plates. Because the

machines in our machine shop cannot deal with stainless steel material, this design was sent to an external machine shop for fabrication.

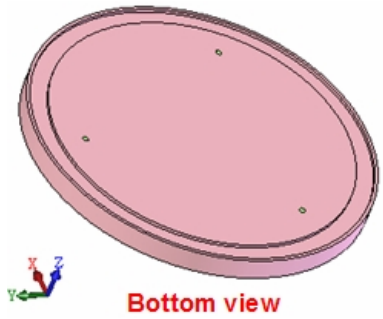

Fig 63: 3D plot of the stainless steel lapping/polishing plates we designed.

A2.3.3 Design of stainless steel circular plates

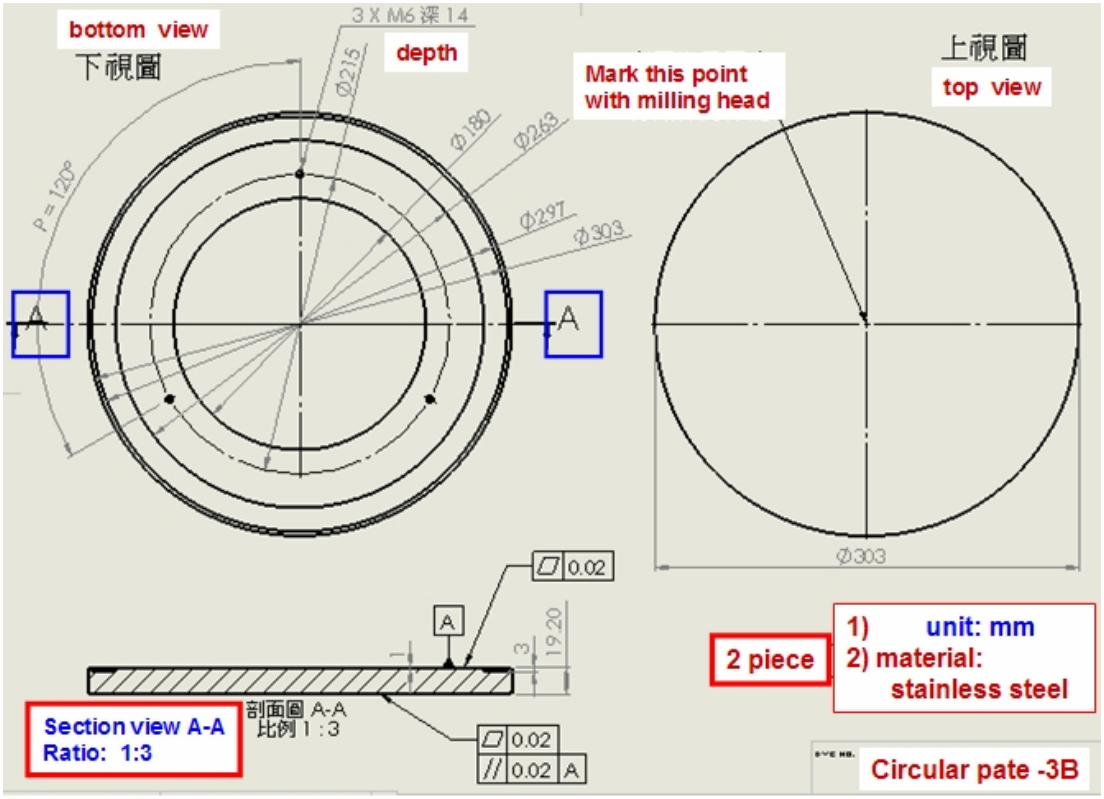

Fig 64: Engineering drawing of the stainless steel lapping/polishing plates we designed.

In Fig 65 the left plate is attached with a grey silicon carbon abrasive disk on it. That is for the lapping process. The middle plate is attached with a black polishing pad. As can be seen from the left and right plates, there are six screw holes on plates. These six screw holes are used to fix abrasive disks if abrasive disk does not have sticky tape on its back for attachment.

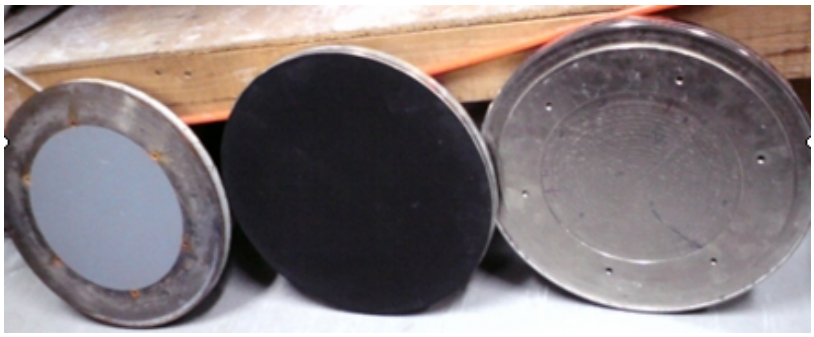

Fig 65: Real object of the stainless steel lapping/polishing plates we designed.

A2.4 Design of single-hole acrylic work cylinder holder for default swing jig arm

In Fig 66 the black aluminum swing jig arm is the original default accessory. The transparent acrylic single-hole work cylinder holder was designed to let work cylinder freely and uniformly rotate in the hole of holder during lapping process.

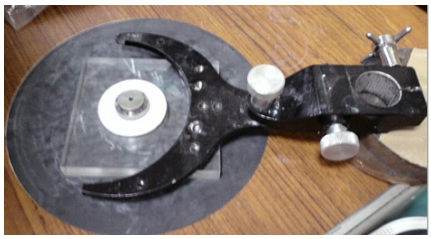

Fig 66: Original default swing jig arm

The dimension of the single-hole work cylinder holder is 100 mm by 110 mm. Its thickness is 13 mm. As can be seen in Fig 66, there are four screw holes on it for fixing it on the black swing jig arm. This is the first step to see if this new polishing method is feasible for fabricating glass micro-resonators. According to the lapping/polishing results, the second version was developed.

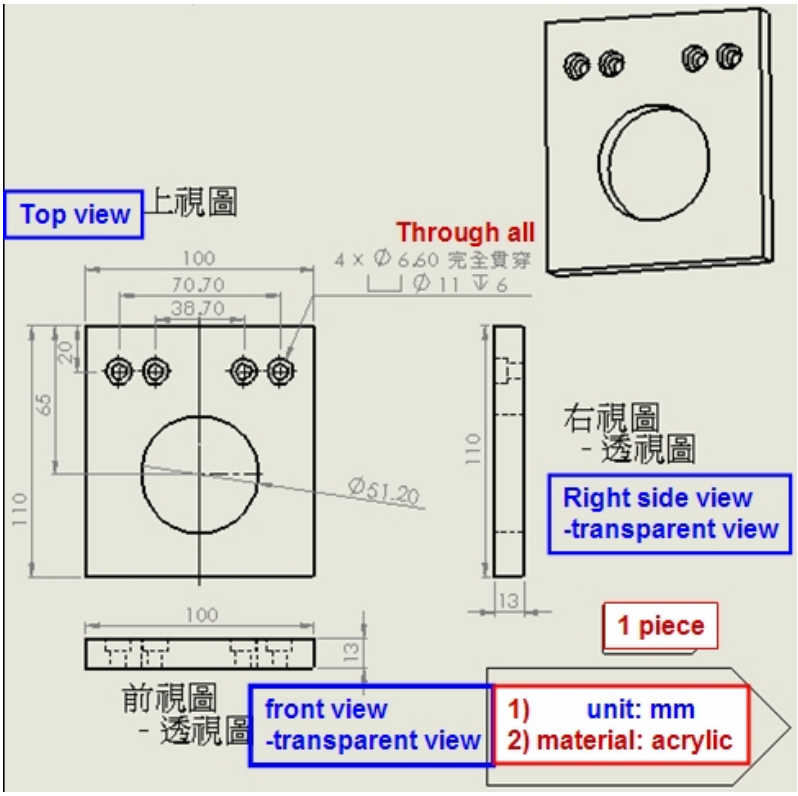

Fig 67: Engineering drawing of the single-hole work cylinder holder.

A2.5 Design of 8-hole acrylic work cylinder holder for default swing jig arm

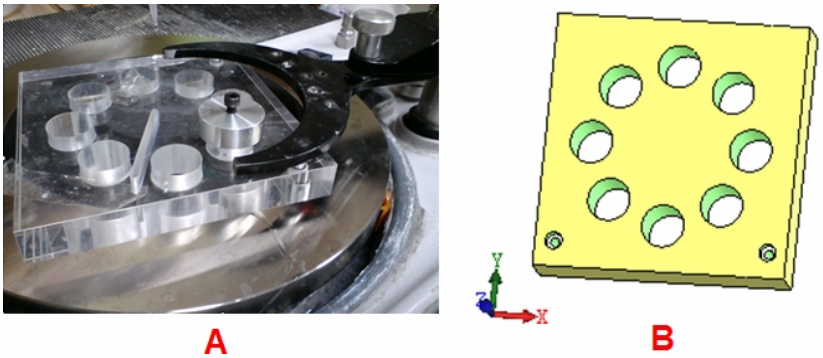

Fig 68: Real object and 3D plot of the 8-hole acrylic work cylinder holder for default swing jig arm

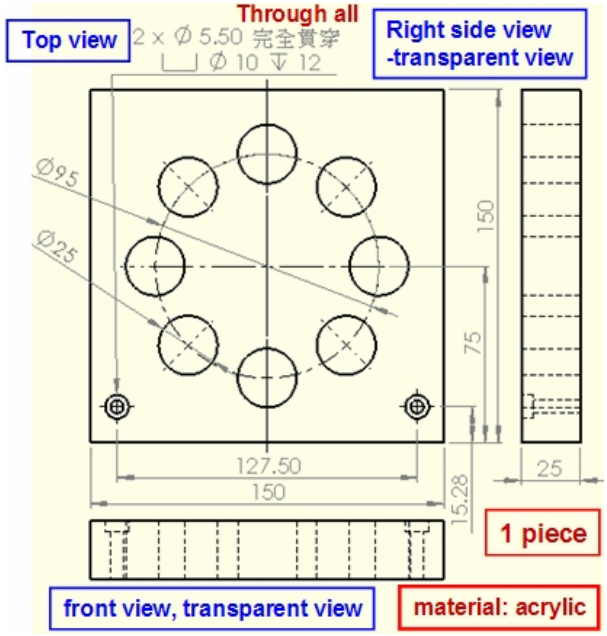

Fig 69: Engineering drawing for the 8-hole acrylic work cylinder holder

This 8-hole work cylinder holder was developed to increase the number of glass capillaries for lapping/polishing processes per batch. There are 8 holes on the acrylic work cylinder holder, so the number of glass micro-resonators per batch will be 8 times

the number for single-hole work cylinder holder. Fig 69 is the engineering drawing and Fig 68b is 3-D plot. As can be seen in Fig 68a, this acrylic work cylinder holder can be fixed with two screws onto the black swing jig arm.

A2.6 Design and fabrication of different work piece fixtures

A2.6.1 Motivation for developing work piece fixtures, work rings, weights, flexible swing jig holder, etc

Although the previous 8-hole work cylinder holder can support eight work cylinders rotating simultaneously during lapping and polishing processes, the lapping/polishing rates are different at different positions (radius). There was a need to design some better facilities that have uniform rates of lapping/polishing for all the work cylinders. This point is very important for this new fabrication method of glass micro-resonators to have large quantity of successful devices coming out per batch. That is, the yield rate of highly polished glass microresonators is much higher than that of generic semiconductor micro-resonators made by photolithographic facilities in a clean room. The following chapters will describe how this apparatus works.

A2.6.2 How this new apparatus works

The principle of this scheme is illustrated in Fig 70. There are small wheels (red) on the arms of the adjustable swing jig holder (light blue). The work ring (pink) rotates in the same direction in which the lapping/polishing circular plate rotates. The work ring (pink) will make work piece fixture (yellow) rotate in the same way. This scheme can let

work piece fixture (yellow) and work cylinders (blue) rotate more freely and uniformly. There are three rotation movements in progress during polishing.

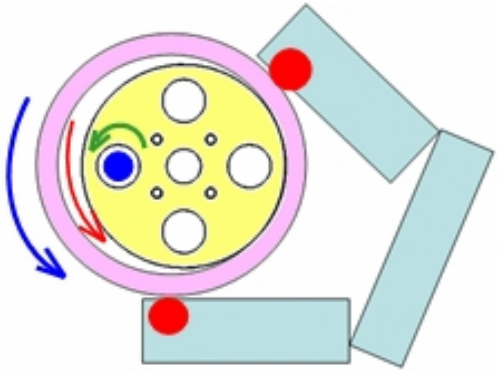

Fig 70: Schematic for the rotation mechanism of work ring, workpiece fixture, and work cylinders.

(1) **Apparatus of small size**

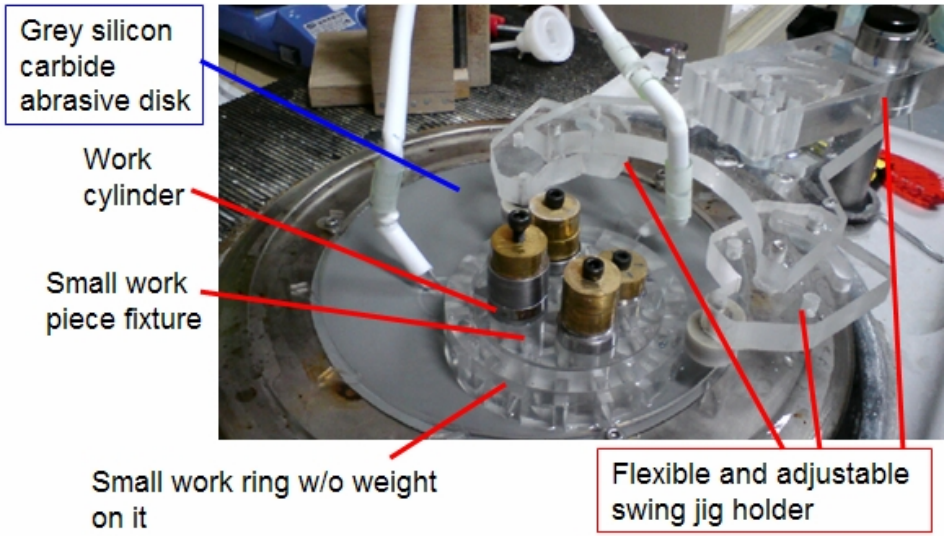

Fig 71: Flexible swing jig works with workpiece fixture of small size.

Fig 71 shows the work piece fixture rotating in the same way as work ring (outer part) rotates. This small work piece fixture can support four work cylinders per batch and it is specially for 8-inch grey abrasive disks. As can be seen in Fig 71, there are small

wheels on the front end of the swing jig holder's arm. This grey silicon carbide abrasive disk is 8-inch without adhesive back. The lapping/polishing plate is 12-inch, so a circular holder on plate is needed to design and fix the grey silicon carbide abrasive disk. This is why a smaller work piece fixture was designed and used in experiments using 8-inch silicon carbide abrasive disks.

(2) **Apparatus of large size**

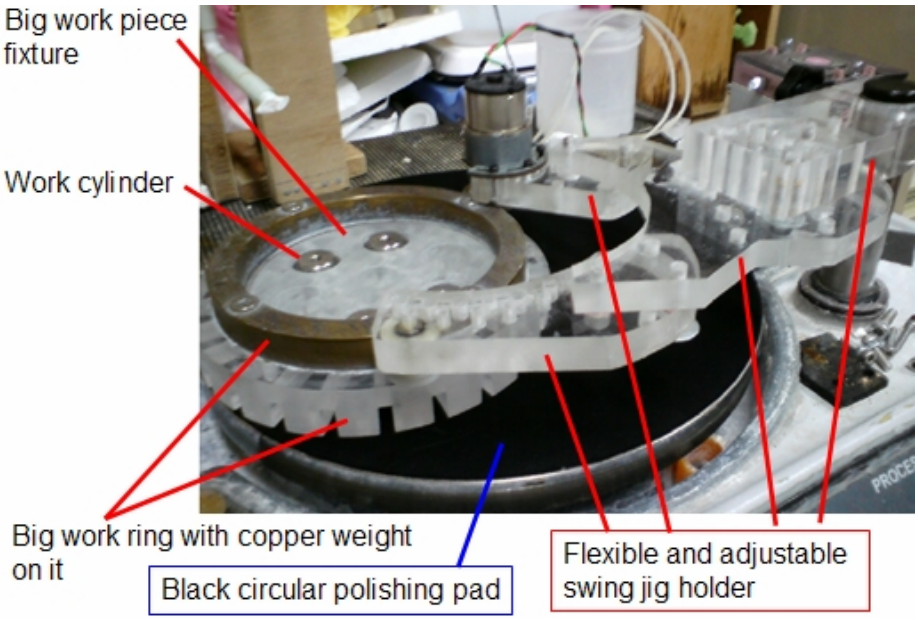

Fig 72: Flexible swing jig works with workpiece fixture of large size for 12-inch soft pad.

Fig 72 shows the bigger work piece fixture. This is specially used for black polishing pads of 12-inch in diameter, so the size of the work piece fixture, work ring, and weight is bigger than that of the smaller version. Due to its larger size, the work piece fixture of this set can support up to eight work cylinders per batch for the final polishing process. In Fig 72 this work piece fixture has six holes and supports six work cylinders at the same time. Polishing slurry is sent to this 12-inch black polishing pad drop by drop

through a silicone tube. The flow rate of polishing slurry can be controlled by a tubing pump.

A2.6.3 Work piece fixture of small diameter

(1) **3D-plot**

As already discussed in the previous sections, this small work piece fixture was designed and used for 8-inch abrasive disks. The diameter of the work piece fixture and work ring is limited by the size of abrasive disks used in experiments. The left portion of Fig 73 shows the partially transparent view of this accessory. The grooves on the bottom side are designed to let water and slurry flow uniformly at any location and not accumulate in any area.

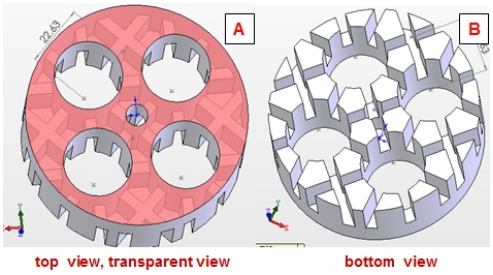

Fig 73: 3D plots of workpiece fixture of small size

(2) **Engineering drawing**

Fig 74 is the engineering drawing of small work piece fixture. The groove depth is 14 mm and groove width is 4 mm. Its diameter is 81 mm. Fig 75 shows the real object.

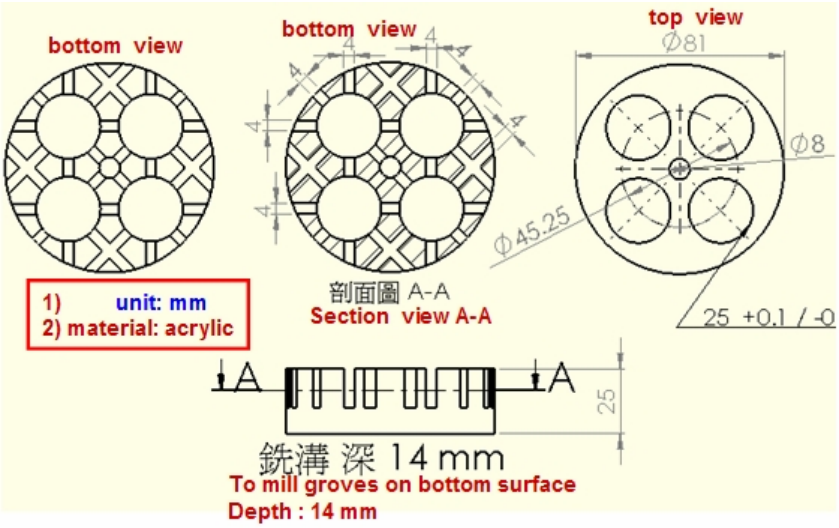

Fig 74: Engineering drawing of workpiece fixture of small size

Fig 75: Photo of workpiece fixture of small size

A2.6.4 Work piece fixture of large diameter

(1) **3D-plot**

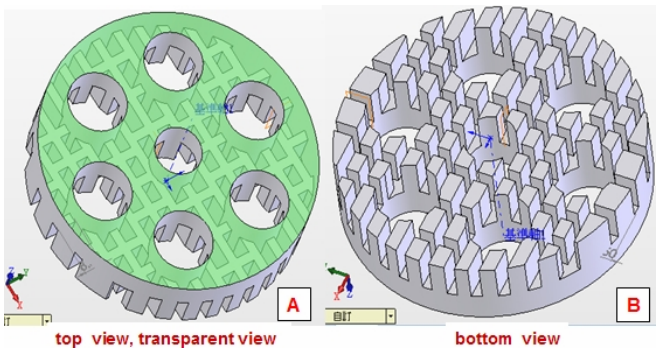

Fig 76: 3D plots of workpiece fixture of large size

As already been discussed in the previous sections, this large work piece fixture was designed and used for 12-inch black polishing pads. In Fig 76 it has six holes and can let six work cylinders rotate and be polished together per batch.

(2) **Engineering drawing**

Fig 77: Photo of workpiece fixture of large size

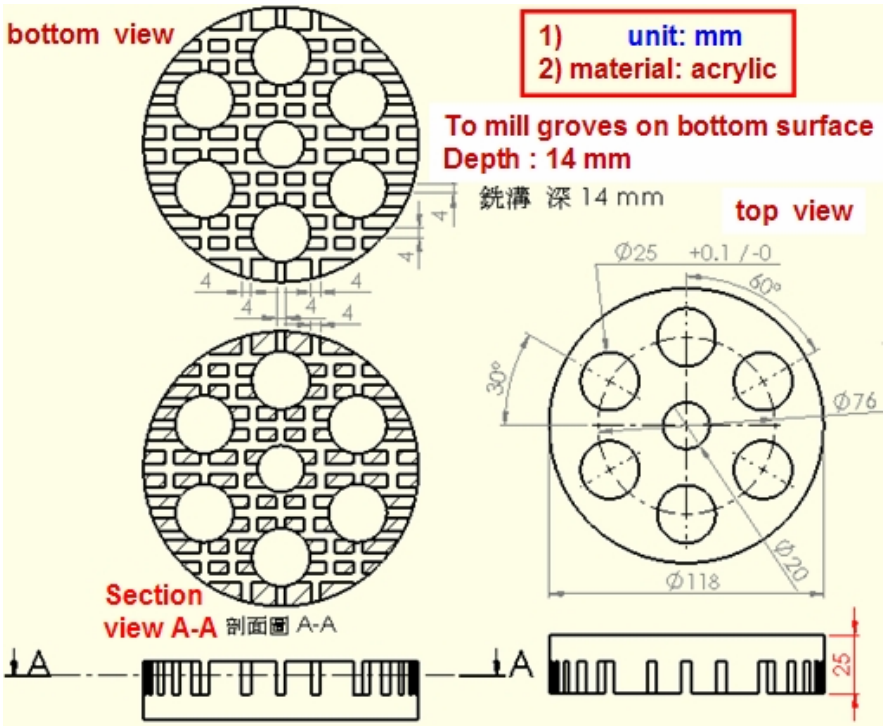

Fig 78: Engineering drawing of workpiece fixture of small size

Fig 78 is the engineering drawing. The diameter of this one is 118 mm and its height is 25 mm. Groove depth is 14 mm and width is 4 mm. The angle between each hole for

work cylinder rotating freely is 60 degrees. Fig 77 shows the real object. As can be seen in figure, grooves on the bottom side can be seen clearly through the acrylic material.

A2.7 Design and fabrication of different work rings

A2.7.1 Work ring of small diameter (Small work ring)

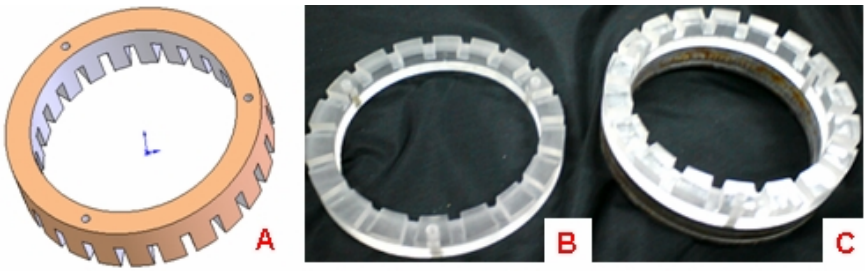

Fig 79: (A) 3D plot and (B) photo of work ring of small diameter

A small work ring was designed and used for 8-inch silicon carbide abrasive disks. Fig 79a shows 3-D plot. Fig 79b is a used ring. Fig 79c is a freshly-made small work ring. Fig 80 is engineering drawing.

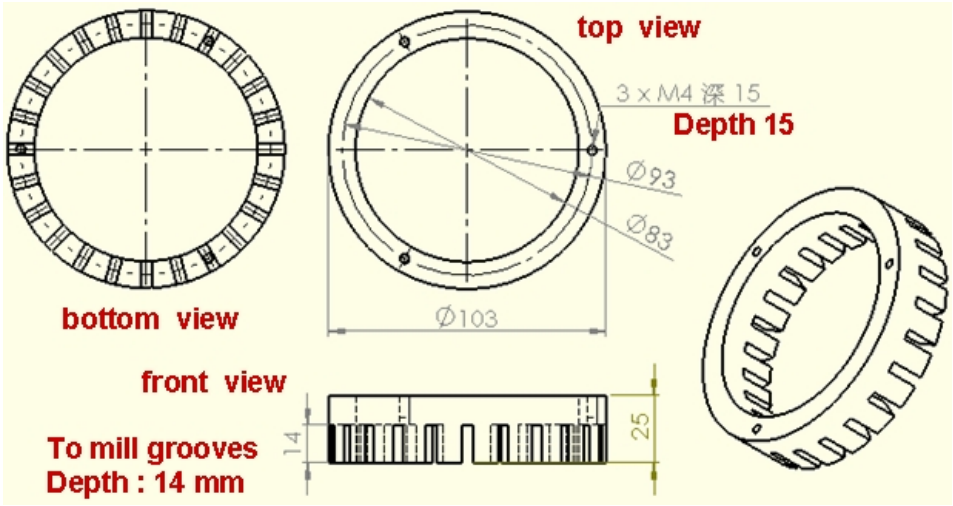

Fig 80: Engineering drawing of work ring of small diameter

A2.7.2 Work ring of big diameter (Big work ring)

A big work ring was designed and used for 12-inch polishing pad. Fig 81a and Fig 81b show 3-D plots. Fig 81c is real object. Fig 82 is engineering.

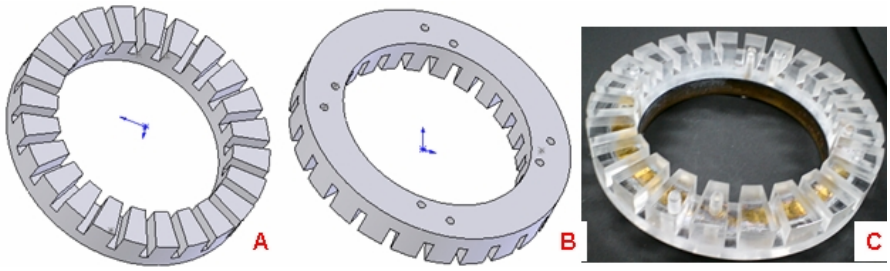

Fig 81: (A) 3D plot and (B) photo of work ring of large diameter

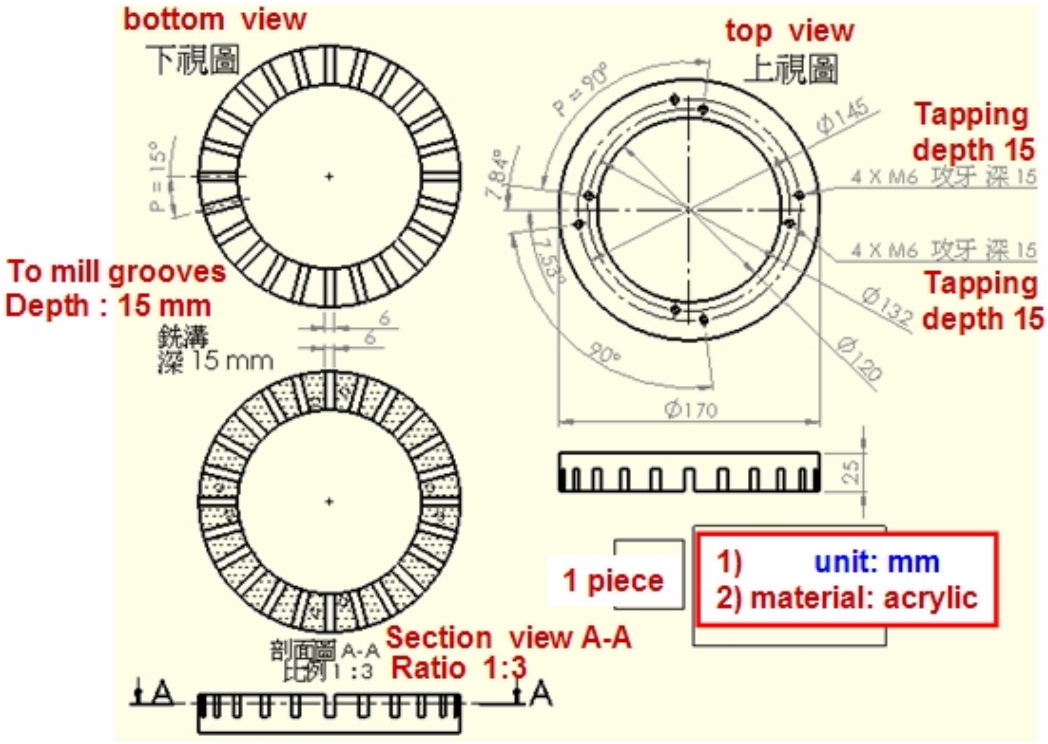

Fig 82: Engineering drawing of work ring of small diameter

A2.8 Design and fabrication of different weights

Different weights were fabricated to hold work piece fixture steady during lapping/polishing (Fig 83a and Fig 83b).

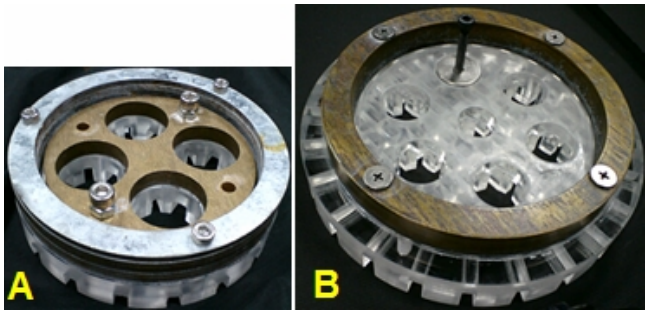

Fig 83: (A) (B) Different weights for small and large workpiece fixture.

A2.9 Design and fabrication of flexible acrylic swing jig holder

A2.9.1 Flexible acrylic swing jig holders

A new flexible acrylic swing jig holder was designed and fabricated.

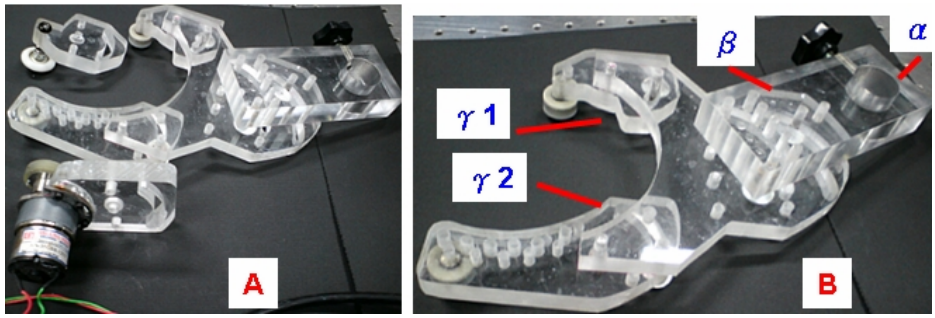

Fig 84: (A) flexible acrylic swing jig holder with DC motor (B) its enlarged view

Fig 85: (A) enlarged view of the short jig arm (B) enlarged view of the motor jig assembly (C) Motor speed controller and its assembly

Fig 84b shows the flexible acrylic swing jig holder. It can be seen that one arm is much longer because the work piece fixture and ring rotated in counterclockwise direction and they may move out of the control of swing jig arm if left arm is not long enough. This design can cover more locations on lapping/polishing plate. There are four positions which can adjust the angle (α, β, γ1, γ2 in Fig 84b). Fig 84a is the whole set of flexible acrylic swing jig holder including all the components of Fig 84b and other components such as short jig arm, motor, motor adaptor, and motor jig. Motor speed controller and its assembly is illustrated in Fig 85c.

Fig 86: (A) flexible acrylic swing jig holder operates for small workpiece fixture. (B) flexible acrylic swing jig holder operates for large workpiece fixture.

Fig 85a shows the enlarged view of the short jig arm and Fig 85b shows the enlarged view of the motor jig assembly. Fig 86a shows how the flexible acrylic swing jig holder works during the lapping process. For this lapping process only two short jig arms were used.

Fig 86b shows how it works during the polishing process. For this polishing process one long jig arm and motor jig arm were used. Its rotation speed can be controlled by the motor controller. These sets of flexible swing jig holders are better than the default swing jig holder and can work well for a wide range of different work piece fixtures and work rings. From Fig 86a and Fig 86b this apparatus can support wide angle operation condition of work piece and reach farther.

A2.10 DC motor controller and motor jig

A2.10.1 DC motor controller

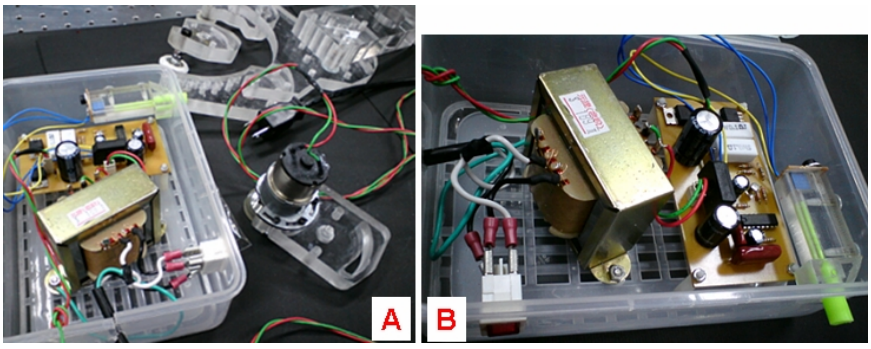

Fig 87: (A) (B) DC motor and controller circuit

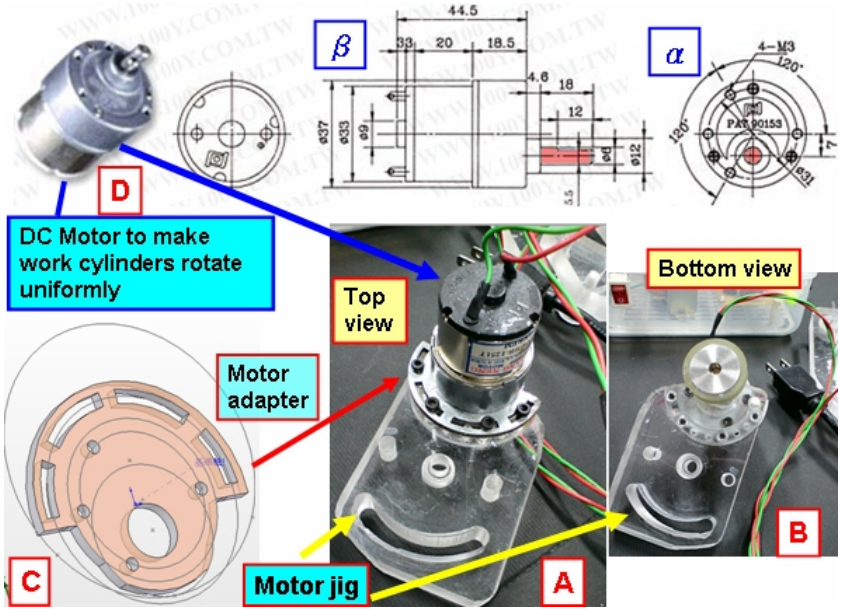

Fig 88: (A) top view of whole assembly of motor and its relevant components. (B) its bottom view (C) 3D plot of motor adapter (D) DC motor (α, β) top and side views of motor, respectively.

In Fig 87a the bottom left portion is controller circuit board and on the bottom right portion is the assembly of DC motor, motor adapter, and motor jig. Top right portion in Fig 87a is assembly of flexible acrylic swing jig holder. Fig 87b is an enlarged view of the circuit board of the DC motor controller installed in its plastic container.

A2.10.2 Motor jig

As can be seen in the figures above, motor and motor adapter need a jig to combine with the whole system of accessories and offer flexibility to adjust the position of motor according to experimental need during polishing work.

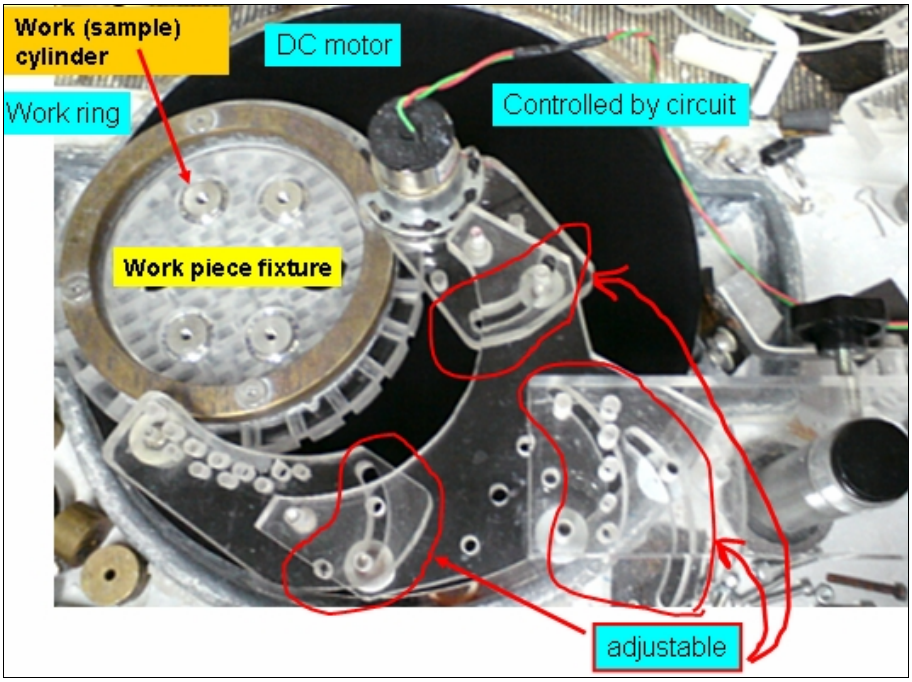

Fig 89: Top view of the whole system which contains flexible swing jig holder, DC motor, large workpiece fixture..

A2.11 A complete set of facilities specific for device take-out/coupling

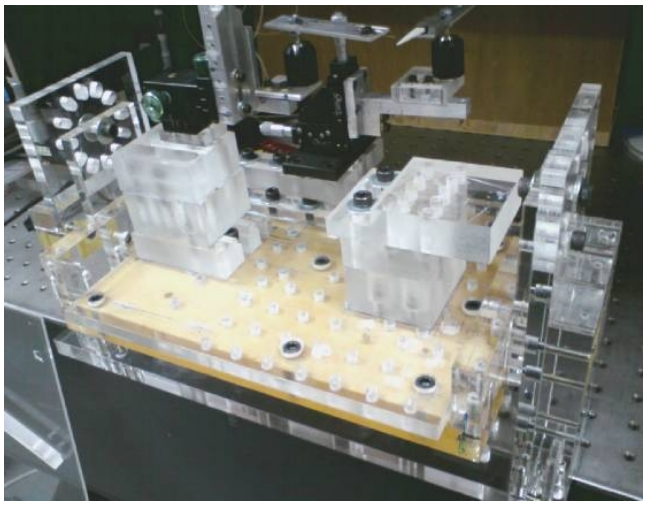

Fig 90: Take-out facility we designed and made.

The size of glass microresonators is below 250 μm and it is difficult to take it out from the top face of work cylinder. We designed and made this whole set of facilities **specific** for glass microresonators. These facilities can help us to take out glass microresonator easily and transfer it to a small flat sharp-end bar which is used for the final coupling process. This facility can rotate to any angle, make the whole work cylinder upside down, and give a convenient way to take out the tiny glass microresonator from the top face of work cylinder. At the same time, the microscope also needs to be rotated upside down for the following steps to monitor the process of taking-out the tiny glass microresonator from work cylinder (see Fig 91).

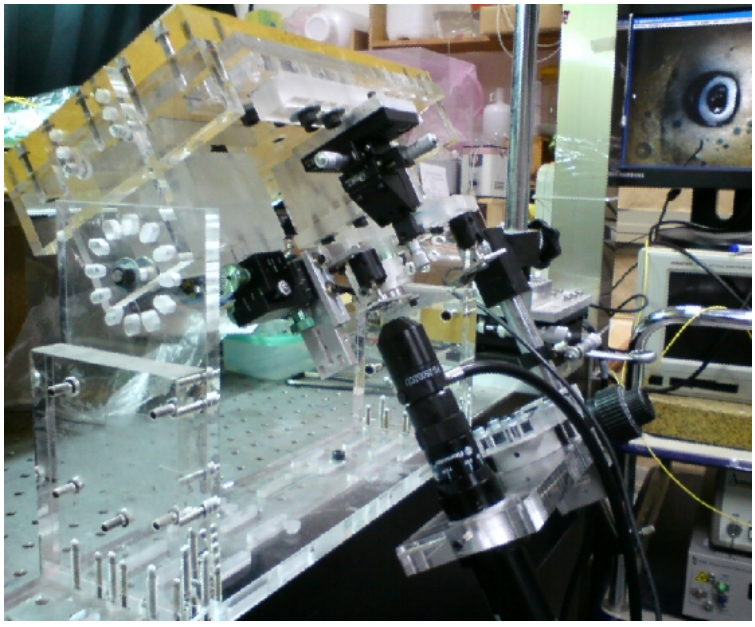

Fig 91: Take-out facility upside down for removing tiny device smoothly and easily from the top of work cylinder with the help of microscope to monitor the whole process owing to the tiny size of glass device.

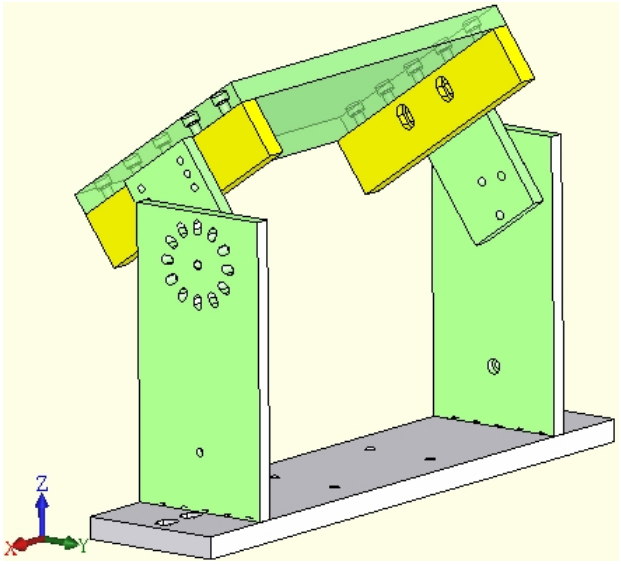

Fig 92: 3D plot of take-out facility.

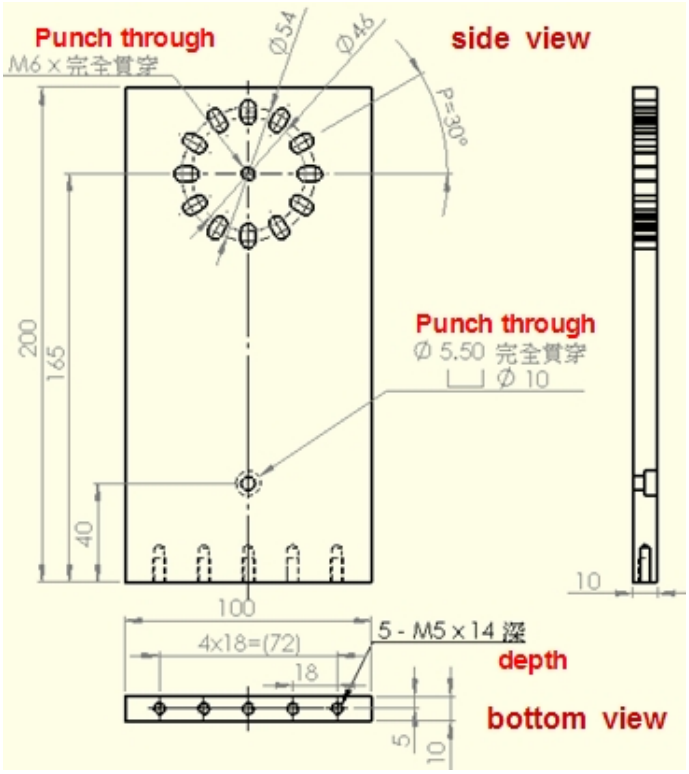

Fig 93: Engineering drawing of two long side plates standing on the bottom plate in Fig 92.

Fig 92 is the 3D plot of this whole set of facilities we designed and made specifically for removing individual tiny glass device from work cylinder. This whole facility can be rotated in many angles with 30 degree increment.

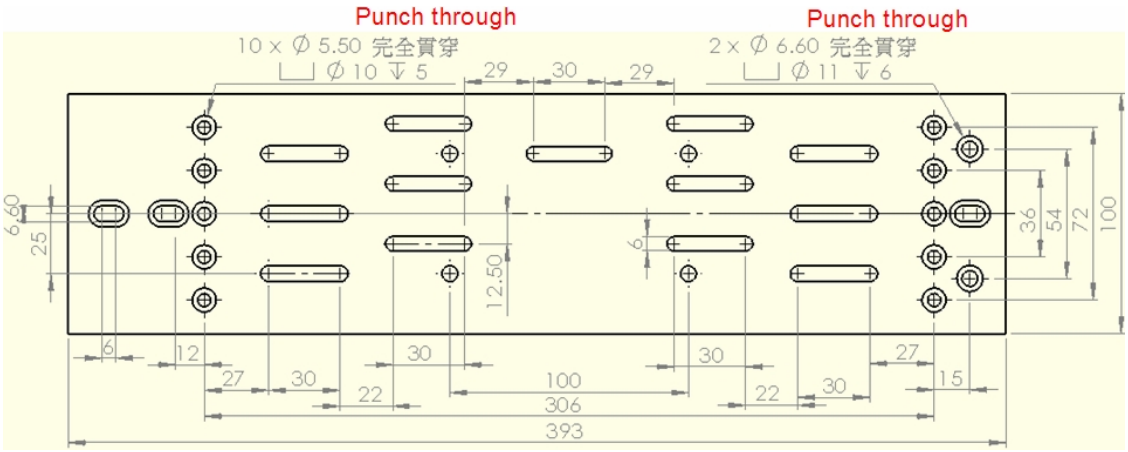

Fig 94: Engineering drawing of the bottom plate in Fig 92.

Fig 93 is the engineering drawing of two long side plates standing on the bottom plate in Fig 92. Fig 94 is the drawing of bottom plate. This whole system have been modified many times due to improving the performances based on the experiment results we obtained each time.

A2.12 Fiber taper puller

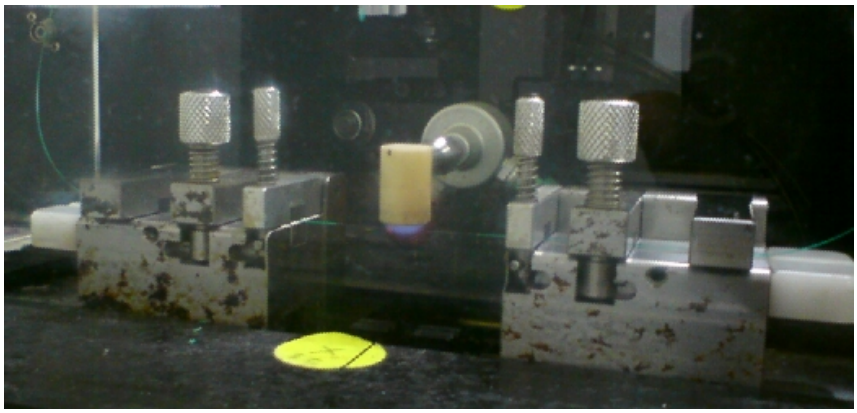

Fig 95: A fiber taper was in pulling motion under torch of high temperature.

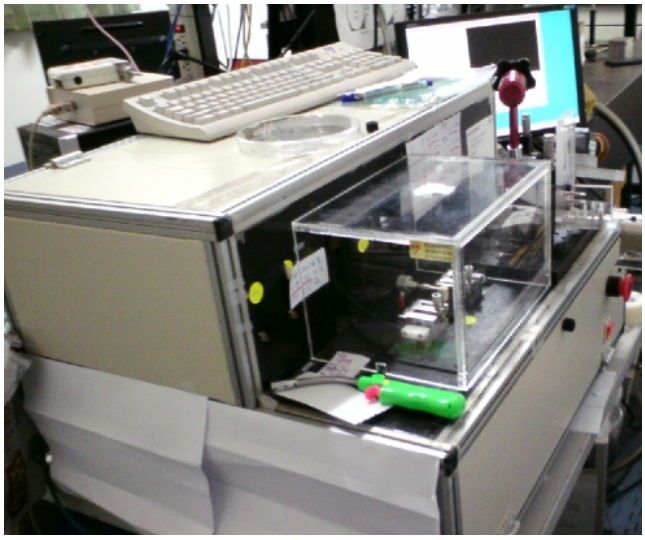

Fig 96: Our fiber tapers were made by this fiber puller machine.

Fig 95 and Fig 96 show the fiber taper puller we used to make tapers which were used to couple glass microresonator in measurement.

MOHS HARDNESS SCALE

		Wax 0.2, Graphite 0.5-0.9
1	**TALC**	Soapstone 1, Lead 1.5, Tin 1.5-1.8, Alabaster 1.7
2	**GYPSUM**	Halite (Rock Salt 2, Magnesium 2.0, Aluminum 2-2.4, Amber 2-2.5, Galena 2.5, Copper 2.5-3, Gold 2.5-3, Mica 2.8
3	**CALCITE**	Limestone 3, Boric Acid 3, Barite 3.3, Brass 3-4, Marble 3-4, Serpentine 3-4, Dolomite 3.5-4
4	**FLUORITE**	Bell Metal 4, Iron 4-5, Platinum 4.3, Soda (soft) Glass 4.5, **Glass 4.8-6.6**, Opal 4-6
5	**APATITE**	Asbestos 5, Manganese 5.0, Steel 5-5.5, Hornblende 5.5, **Stainless Steel 5.5-6.3**
6	**ORTHOCLASE**	Feldspar 6, Hematite 6, Magnetite 6, Pumice 6, Pyrite 6.3, Agate 6.5-7, Garnet 6.5-7.5
7	**QUARTZ**	Flint 7, Silicon 7.0, Tourmaline 7.3, Emery 7-9, Beryl 7.8
8	**TOPAZ**	Case Hardened File Steel 7.8-8.5
9	**CORUNDUM**	Alundum 9+, Chromium 9.0, Carborundum 9.3, Boron 9.5
10	**DIAMOND**	

Table 2: Mohs hardness scale for some common materials

Bibliography

[1] Brent E. Little and Sai T. Chu, “Towards very large-scale integrated photonics”, Optics and Photonics News, vol. 11, Issue 11, pp. 24- (2000)

[2] B. E. Little, S. T. Chu, W. Pan, D. Ripin, T. Kaneko, Y. Kokubun, and E. Ippen, ” Vertically coupled glass microring resonator channel dropping filters”, IEEE Photonics Technology Letters, vol. 11, pp. 215-217, 1999

[3] S. T. Chu, B. E. Little, W. Pan, T. Kaneko, and Y. Kokubun, "Second order filter response from parallel coupled glass microring resonators", IEEE Photonics Technology Letters, vol. 11, pp. 1426-1428, 1999.

[4] B. E. Little and S. T. Chu, “Application of micro-resonators in large-scale optical signal processing circuits", Laser Resonators III, 2000.

[5] S. T. Chu, B. E. Little, W. Pan, T. Kaneko, S. Sato, and Y. Kokubun, "An eight-channel add-drop filter using vertically coupled microring resonators over a cross grid", IEEE Photonics Technology Letters, vol. 11, pp. 691-693, 1999.

[6] T. A. Ibrahim, W. Cao, Y. Kim, J. Li, J. Goldhar, P.-T. Ho and Chi H. Lee, “All-optical switching in a laterally coupled microring resonator by carrier injection,” IEEE Photonics Technology Letters, vol. 15, pp. 36-38, January 2003.

[7] T. A. Ibrahim, R. Grover, L.-C. Kuo, S. Kanakaraju, L.C. Calhoun, and P.-T. Ho, “All-optical AND/NAND logic gates using semiconductor microresonators”, IEEE Photonics Technology Letters, vol. 15, pp. 1422-1424, October 2003

[8] T. A. Ibrahim, L. C. Kuo, K. Amarnath, R. Grover, V. Van and, P.-T. Ho, "Photonic logic NOR gate using two symmetric microring resonators." Conference on Lasers and Electro-Optics. Optical Society of America, 2004

[9] T. A. Ibrahim, V. Van and P.-T. Ho, "All-optical time-division demultiplexing and spatial pulse routing with a GaAs/AlGaAs microring resonator", Optics Letters, vol. 27, pp. 803-805, May 2002

[10] Martin T. Hill, Harmen J. S. Dorren, Tjibbe de Vries, Xaveer J. M. Leijtens, Jan Hendrik den Besten, Barry Smalbrugge, Yok-Siang Oei, Hans Binsma, Giok-Djan Khoe & Meint K. Smit, "A fast low-power optical memory based on coupled micro-ring lasers", Nature 432.7014, 206-209, 2004

[11] Wang, Z., Yuan, G., Verschaffelt, G., Danckaert, J., & Yu, S., "Storing 2 bits of information in a novel single semiconductor microring laser memory cell", IEEE Photonics Technology Letters, 20(14), 1228-1230, 2008

[12] Kuwata-Gonokami, M., Ozawa, S., Jordan, R. H., Dodabalapur, A., Katz, H. E., Schilling, M. L., & Slusher, R. E., "Polymer microdisk and microring lasers", Optics Letters, 20(20), 2093-2095, 1995.

[13] Chlouverakis, K. E., Mikroulis, S., Stamataki, I., & Syvridis, D.,"Chaotic dynamics of semiconductor microring lasers", Optics Letters, 32(20), 2912-2914, 2007

[14] Liang, D., Fiorentino, M., Okumura, T., Chang, H. H., Spencer, D. T., Kuo, Y. H., & Bowers, J. E., "Electrically-pumped compact hybrid silicon microring lasers for optical interconnects", Optics Express, 17(22), 20355-20364, 2009

[15] Ayça Yalçın, Ketul C. Popat, John C. Aldridge, Tejal A. Desai, John Hryniewicz, Nabil Chbouki, Brent E. Little, Oliver King, Vien Van, Sai Chu, David Gill, Matthew Anthes-Washburn, M. Selim Unlu, and Bennett B. Goldberg, "Optical sensing of biomolecules using microring resonators." Selected Topics in IEEE Journal of Quantum Electronics, 12.1: 148-155, 2006

[16] Chao, C. Y., Fung, W., & Guo, L. J.," Polymer microring resonators for biochemical sensing applications", IEEE Journal of selected topics in Quantum Electronics, 12(1), 134-142, 2006

[17] J. E. Heebner and R. W. Boyd, "Enhanced all-optical switching by use of a nonlinear fiber ring resonator," Optics Letters, vol. 24, pp. 847–849, June 1999

[18] P. P. Absil, J. V. Hryniewicz, B. E. Little, R. A. Wilson, L. G. Joneckis, and P.-T. Ho, "Compact microring notch filters," IEEE Photonics Technology Letters, vol. 12, pp. 398-400, 2000

[19] E. A. J. Marcatili, "Bends in optical dielectric guides", Bell System Technical Journal, vol. 48, pp. 2103-32, 1969

[20] J. Haavisto and G. A. Pajer, "Resonance effects in low-loss ring waveguides," Optics Letters, vol. 5, pp. 510-512, 1980

[20] H. A. Haus, "Waves and Fields in Optoelectronics", Prentice-Hall, 1983

[21] V. Van, T. A. Ibrahim, K. Ritter, P. P. Absil, F. G. Johnson, R. Grover, J. Goldhar and P.-T. Ho, "All-optical nonlinear switching in GaAs-AlGaAs microring resonators," IEEE Photonics Technology Letters, vol. 14, pp. 74-76, January 2002

[22] John Heebner, Rohit Grover, Tarek Ibrahim, "Optical Microresonators: Theory, Fabrication, and Applications", Springer Series in Optical Sciences, vol. 138, 2008, 268 p

[23] B. E. Little, S. T. Chu, H. A. Haus, J. Foresi, and J. P. Laine, "Microring resonator channel dropping filters", Journal of Lightwave Technology, vol. 15, pp. 998–1005, June 1997

[24] V. Van, T. A. Ibrahim, K. Ritter, P. P. Absil, F. G. Johnson, R. Grover, J. Goldhar and P.-T. Ho, "All-optical nonlinear switching in GaAs-AlGaAs microring resonators," IEEE Photonics Technology Letters, vol. 14, pp. 74-76, January 2002

[25] T. A. Ibrahim, V. Van and P.-T. Ho, "All-optical time-division demultiplexing and spatial pulse routing with a GaAs/AlGaAs microring resonator," Optics Letters, vol. 27, pp. 803-805, May 2002

[26] V. Van, T. A. Ibrahim, P. P. Absil, J. V. Hryniewicz, F. G. Johnson, R. Grover and P.-T. Ho, "Optical signal processing using nonlinear semiconductor microring resonators," IEEE Journal of Selected Topics in Quantum Electronics, special issue on nonlinear optics, vol.8, pp. 705-713, May 2002

[27] T. A. Ibrahim, W. Cao, Y. Kim, J. Li, J. Goldhar, P.-T. Ho and Chi H. Lee, "All-optical switching in a laterally coupled microring resonator by carrier injection," IEEE Photonics Technology Letters, vol. 15, pp. 36-38, January 2003

[28] R. Grover, T. A. Ibrahim, T. N. Ding, Y. Leng, L.-C. Kuo, S. Kanakaraju, K. Amarnath, L. C. Calhoun, and P.-T. Ho, "Laterally coupled InP-based single mode microracetrack notch filter," IEEE Photonics Technology Letters, vol. 15, pp. 1082-1084, August 2003

[29] T. A. Ibrahim, R. Grover, L.-C. Kuo, S. Kanakaraju, L.C. Calhoun, and P.-T. Ho, "All-optical AND/NAND logic gates using semiconductor microresonators," IEEE Photonics Technology Letters, vol. 15, pp. 1422-1424, October 2003

[30] T. A. Ibrahim, W. Cao, Y. Kim, J. Li, J. Goldhar, P.-T. Ho, and Chi H. Lee, "Photonic switching in semiconductor microring devices by free carrier injection," Journal of Lightwave Technology vol. 21, Issue 12, pp. 2997, 2003

[31] Ibrahim, T. A., Amarnath, K., Kuo, L. C., Grover, R., Van, V., and Ho, P. T., “Photonic logic NOR gate based on two symmetric microring resonators”, Optics letters, 29, 2779-2781, 2004

[32] Goeppert-Mayer M., "Über Elementarakte mit zwei Quantensprüngen", Annals of Physics 9 (3): 273–95, 1931

[33] W. Kaiser and C.G.B. Garrett, "Two-photon excitation in CaF2:Eu2+," Physical Review Letters 7, 229–232 (1961)

[34] I.D. Abella, "Optical double-quantum absorption in cesium vapor," Physical Review Letters, 9, 453 (1962)

[35] Y. R. Shen, “The Principles of Nonlinear Optics”, Wiley, 1984

[36] R. W. Boyd, “Nonlinear optics”, Academic Press, 2003

[37] Nicolaas Bloembergen, “Nonlinear Optics”, 1996

[38] P. N. Butcher and D. Cotter, "The Element of Nonlinear Optics", Cambridge University Press, 1990

[39] Yamashita, Y. Saito, J H Choi, “Carbon Nanotubes and Graphene for Photonic Applications”, 2013

[40] Elsa Garmire, Alan Kost, “Nonlinear Optics in Semiconductor Physics **I**”, Academic Press, 1998

[41] Van, V., Ibrahim, T. A., Absil, P. P., Johnson, F. G., Grover, R., & Ho, P. T., “Optical signal processing using nonlinear semiconductor microring resonators”, IEEE Journal of Selected Topics in Quantum Electronics, 8(3), 705-713, 2002

[42] J. H. Marburger and F. S. Felber, “Theory of a lossless nonlinear Fabry–Pérot interferometer,” Phys. Rev. A, vol. 17, no. 1, pp. 335–342, Jan. 1978

[43] D. Sarid, “Analysis of bistability in a ring-channel waveguide,” Opt. Lett., vol. 6, pp. 552–553, Nov. 1981

[44] F. J. Fraile-Pelaez, M. Prol, D. J. Santos, and J. M. Soto-Crespo, “Transient analysis of a nonlinear fiber ring resonator,” Appl. Phys. Lett., vol.63, pp. 1477–1479, Sept. 1993.

[45] D. Osugu, H. Shigekuni, and Y. Yokota, “Dynamic transmission properties of a nonlinear fiber ring resonator,” Opt. Lett., vol. 20, pp. 2288–2290, Nov. 1995.

[46] K. Osugu, “Dynamic behavior of reflection optical bistability in a nonlinear fiber ring resonator,” IEEE J. Quantum Electron., vol. 32, pp.1537–1543, Sept. 1996.

[47] Dr. T. A. Ibrahim, dissertation, 2004

[48] Li-Chiang Kuo, Vien Van, Kuldeep Amarnath, T. N. Ding, P. T. Ho, W. Astar, G. M. Carter,” Cascaded integrated photonic AND gates based on GaAs ring resonators”, In Conference on Lasers and Electro-Optics (CLEO), May 2006

[49] T. Sherwood, A. C. Young, J. Takayesu, A. K. Jen, L. R. Dalton, , and A. Chen, “Microring resonators on side-polished optical fiber.”, Photonics Technology Letters, IEEE, 17(10), 2107-2109, 2005.

[50] Pauline Girault, Nathalie Lorrain, Luiz Poffo, Mohammed Guendouz, Jonathan Lemaitre, Christiane Carré, Michel Gadonna, Dominique Bosc and Guillaume Vignaud, “Integrated polymer micro-ring resonators for optical sensing applications”, J. Appl. Phys. 117, 104504 , 2015

[51] Jingya Xie, Linjie Zhou, , Xinwan Li, Jianping Chen, “Microdisk resonator assisted all-optical switching with improved speed using a reverse-biased p-n diode”, Optics Communications , 343, pp. 51–55, 15 May 2015

[52] Timurdogan, E., Sorace-Agaskar, C. M., Hosseini, E. S., & Watts, M. R., "An interior-ridge silicon microring modulator", Journal of Lightwave Technology, 31(24), 3907-3914, 2013

[53] Lin Yang, Jianfeng Ding, Qiaoshan Chen, Ping Zhou, Fanfan Zhang, and Lei Zhang, "Optical Digital to Analog Converter Based on Microring Switches", Optics Letters, Vol. 39, No. 19, pp. 5736, 2014

[54] Xiaoliang Zhu, Kishore Padmaraju, Lian-Wee Luo, Shu Yang, Madeleine Glick, Raj Dutt, Michal Lipson and Keren Bergman, "Fast Wavelength Locking of a Microring Resonator", IEEE Photonics Technology Letters, vol.26, no. 23, 2014

[55] Zhe Xuan, Yangjin Ma, Yang Liu, Ran Ding, Yunchu Li, Noam Ophir, Andy Eu-Jin Lim, Guo-Qiang Lo, Peter Magill, Keren Bergman, Tom Baehr-Jones, and Michael Hochberg, "Silicon microring modulator for 40 Gb/s NRZ-OOK metro networks in O-band", Optics Express vol. 22, 23, pp. 28284, 2014

[56] Zheng A, Dong J, Zhou L, Xiao X, Yang Q, Zhang X, Chen J., "Fractional-order photonic differentiator using an on-chip microring resonator", Optics Letters, vol. 39, 21, pp.6355, 2014

[57] Cai, D. P., Lu, J. H., Chen, C. C., Lee, C. C., Lin, C. E., & Yen, T. J., "Compact pulley-type microring resonator with high quality factor", Applied Physics Express, 7.11, 112202, 2014

[58] Todd H. Stievater, Marcel W. Pruessner, Doewon Park, William S. Rabinovich, R. Andrew McGill, Dmitry A. Kozak, Robert Furstenberg, Scott A. Holmstrom, and Jacob B. Khurgin, "Trace gas absorption spectroscopy using functionalized microring resonators", Optics Letters, 39(4), 969-972, 2014

[59] Sivanandini, M., Dhami Sukhdeep, S., & Pabla, B. S., “Chemical Mechanical Polishing By Colloidal Silica Slurry”, International Journal of Engineering Research and Applications (IJERA) ISSN, 6, 2248-9622, 2013

[60] Shubin Yan, Minghui Li, Liang Luo, Kezhen Ma, Chenyang Xue and Wendong Zhang, “Optimisation Design of Coupling Region Based on SOI Micro-Ring Resonator”, Micromachines, 6(1), 151-159, 2014

[61] Lei Jin, Mingyu Li, Jian-Jun He, “Highly-sensitive silicon-on-insulator sensor based on two cascaded micro-ring resonators with vernier effect”, Optics Communications, 284(1), 156-159, 2011

[62] Valentina Donzella, Ahmed Sherwali, Jonas Flueckiger, Samantha M. Grist, Sahba Talebi Fard, and Lukas Chrostowski, “ Design and fabrication of SOI micro-ring resonators based on sub-wavelength grating waveguides”, Optics Express, 23(4), 4791-4803, 2015

[63] C. Ciminellin, F. Dell'Olio, D. Conteduca, C.M. Campanella, M.N. Armenise, “High performance SOI microring resonator for biochemical sensing”, Optics and Laser Technology, 59, 60-67, 2014

[64] Rémi Henriet, Patrice Salzenstein, Davor Ristic, Aurélien Coillet, Michel Mortier, Alphonse Rasoloniaina, Khaldoun Saleh, Gilles Cibiel, Yannick Dumeige, Maurizio Ferrari, Yanne K Chembo, Olivier Llopis and Patrice Féron, “High quality factor optical resonators”, Physica Scripta, 162, 014032, 2014

[65] Pauline Girault, Nathalie Lorrain, Luiz Poffo, Mohammed Guendouz, Jonathan Lemaitre, Christiane Carre, Michel Gadonna, Dominique Bosc, and Guillaume Vignaud,

"Integrated polymer micro-ring resonators for optical sensing applications", Journal of Applied Physics, 117(10), 104504, 2015

[66] Tao Ling, Sung-Liang Chen, and L. Jay Guo, "Fabrication and characterization of high-Q polymer micro-ring resonator and its application as a sensitive ultrasonic detector", Optics Express, 19(2), 861-869, 2011.

[67] Raji Shankar, Irfan Bulu, and Marko Lončar, "Integrated high-quality factor silicon-on-sapphire ring resonators for the mid-infrared", Applied Physics Letters, 102(5), 051108, 2013

[68] Hansuek Lee, Tong Chen, Jiang Li, Ki Youl Yang, Seokmin Jeon, Oskar Painter and Kerry J. Vahala, "Chemically etched ultrahigh-Q wedge-resonator on a silicon chip", Nature Photonics, 6(6), 369-373, 2012

[69] Cheng Wang, Michael J. Burek, Zin Lin, Haig A. Atikian, Vivek Venkataraman, I-Chun Huang, Peter Stark, and Marko Lončar, "Integrated high quality factor lithium niobate microdisk resonators", Optics Express Vol. 22, Issue 25, pp. 30924-30933, 2014

[70] Kazunari Tada, Gregory A. Cohoon, Khanh Kieu, Masud Mansuripur, and Robert A. Norwood, "Fabrication of High-Q Microresonators Using Femtosecond Laser Micromachining", IEEE of Photonics Technology Letters, 25(5), 430-433, 2012

[71] W. N. Herman, Y. Leng, V. Yun, W.-Y. Chen, V. Van, T. Ding, L. Lucas, L. Li, E. Gershgoren, J. T. Fourkas, P.-T. Ho, J. Goldhar, "Polymer Waveguides and Advances in Fabrication Techniques", In Integrated Photonics and Nanophotonics Research and Applications (p. ITuA1). Optical Society of America, July of 2007

[72] Linjie Li and John T. Fourkas, "Multiphoton polymerization", Materials Today, 10(6), 30-37, 2007

[73] Christopher N. LaFratta, John T. Fourkas,* Tommaso Baldacchini, and Richard A. Farrer, “Multiphoton fabrication”, Angewandte Chemie International Edition, 46(33), 6238-6258, 2007

[74] Cheng Wang, Michael J. Burek, Zin Lin, Haig A. Atikian, Vivek Venkataraman, I-Chun Huang, Peter Stark, and Marko Lončar, “Integrated high quality factor lithium niobate microdisk resonators”, Optics Express, 22(25), 30924-30933, 2014

[75] A. Guarino, G. Poberaj, D. Rezzonico, R. Degl’Innocenti, and P. Günter, “Electro-optically tunable microring resonators in lithium niobate,” Nature Photonics 1(7), 407–410, 2007

[76] B.H.T. Chai: Optical Crystals. In: CRC Handbook of Laser Science and Technology, Supplement2: Optical Materials, ed. by M.J. Weber (Boca Raton: CRC Press), 1995